Nano Research

ISSN 1998-0124 CN 11-5974/O4
https://doi.org/10.1007/s12274-021-3439-3

Research Article

Recent advances in anode materials for potassium-ion batteries: A review

Lianbo Ma[1,2,3], Yaohui Lv[1], Junxiong Wu[4] (✉), Chuan Xia[5], Qi Kang[6] (✉), Yizhou Zhang[7], Hanfeng Liang[8], and Zhong Jin[2,3] (✉)

[1] *School of Materials Science and Engineering, Anhui University of Technology, Maanshan 243002, China*
[2] *Key Laboratory of Mesoscopic Chemistry of Ministry of Education (MOE), Jiangsu Key Laboratory of Advanced Organic Materials, State Key Laboratory of Coordination Chemistry, School of Chemistry and Chemical Engineering, Nanjing University, Nanjing 210023, China*
[3] *Shenzhen Research Institute of Nanjing University, Shenzhen 518063, China*
[4] *Department of Mechanical Engineering, The Hong Kong Polytechnic University, Kowloon, Hong Kong, China*
[5] *School of Materials and Energy, University of Electronic Science and Technology of China, Chengdu 610054, China*
[6] *Department of Polymer Science and Engineering, Shanghai Key Laboratory of Electrical Insulation and Thermal Ageing, Shanghai Jiao Tong University, Shanghai 200240, China*
[7] *Institute of Advanced Materials and Flexible Electronics (IAMFE), School of Chemistry and Materials Sciences, Nanjing University of Information Science & Technology, Nanjing 210044, China*
[8] *College of Chemistry and Chemical Engineering, Xiamen University, Xiamen 361005, China*

Received: 6 February 2021 / **Revised:** 3 March 2021 / **Accepted:** 4 March 2021

ABSTRACT

Potassium-ion batteries (PIBs) are appealing alternatives to conventional lithium-ion batteries (LIBs) because of their wide potential window, fast ionic conductivity in the electrolyte, and reduced cost. However, PIBs suffer from sluggish K^+ reaction kinetics in electrode materials, large volume expansion of electroactive materials, and the unstable solid electrolyte interphase. Various strategies, especially in terms of electrode design, have been proposed to address these issues. In this review, the recent progress on advanced anode materials of PIBs is systematically discussed, ranging from the design principles, and nanoscale fabrication and engineering to the structure-performance relationship. Finally, the remaining limitations, potential solutions, and possible research directions for the development of PIBs towards practical applications are presented. This review will provide new insights into the lab development and real-world applications of PIBs.

KEYWORDS

potassium-ion batteries, anode materials, nanoscale engineering, electrode design

1 Introduction

The ever-increasing energy demand of our society calls for clean and sustainable energy sources. Most renewable energy sources, such as wind and solar, are intermittent; therefore, energy storage devices are needed to store and release the energy power on demand [1–3]. Lithium-ion batteries (LIBs) are one kind of the most popular devices, and currently, they have dominated the market of electronic devices. Unfortunately, the scarcity and uneven distribution of Li resources limit the wide spreading application of LIBs. In addition, the rapid development of the electronic market requires a significant improvement in energy density [4, 5]. Owing to the intrinsic properties of alkaline lithium metal and the as-formed LIBs, the achieved energy density from LIBs almost approached its theoretical limits [6, 7], and thus new alternatives are always pursed. So far, various energy storage and conversion systems have been explored, including sodium-ion batteries (SIBs), sulfur-based batteries, metal-based batteries, supercapacitors, and so on [8–11]. Widespread research interest in SIBs has recently been soaring due to the natural abundance of sodium, but the relatively low energy density caused by the high redox potential (−2.71 V vs. standard hydrogen electrode (SHE)) hinders its practical development. For comparison, potassium has a relatively low potential, i.e., −2.936 V vs. SHE, a value close to −3.04 V of Li/Li^+ redox couple, ensuing a comparable energy density. Besides, the low cost and abundance of K resources make potassium-ion batteries (PIBs) an attractive alternative to LIBs, especially in large-scale energy storage [12–14]. Another notable advantage of PIBs over LIBs and SIBs is that the much weaker Lewis acidity of K^+ ion results in smaller solvated ions as compared to Li and Na ions, leading to fast K^+ ion transportation in the electrolyte. All these features mentioned above contribute to the development of PIBs as a promising battery system for large-scale energy storage.

Similar to LIBs, PIBs consist of four main components: cathode, anode, separator, and electrolyte. Each component is essential and significantly affects the electrochemical performance of PIBs. Regarding the slow kinetics of K^+ ions in cathode materials, the rational design of anode materials featured with high capacity, fast K-ion diffusivity, and good cyclic stability is crucial to building high-performance PIBs [15]. In this regard,

Address correspondence to Junxiong Wu, jwuba@connect.ust.hk; Qi Kang, kangqi@sjtu.edu.cn; Zhong Jin, zhongjin@nju.edu.cn

numerous anode materials have been explored and various structures have been designed and constructed, in order to improve the electrochemical performance. Graphite, a commercially available carbon material, is recognized as a potential anode material in PIBs [16] through an intercalation/deintercalation mechanism. To facilitate K^+ storage behaviors in pores and voids, carbons with various architectures, such as hollow and porous structures, have been deliberately designed. However, carbon-based anodes usually show limited capacities and energy densities, fail to satisfy the increasing demands of devices [17]. Since then, a lot of inorganic materials have emerged in PIBs, including metal alloys, oxides, and sulfides, but the limitations lie in the poor electrical conductivity, fragile structural integrity, and poor K^+ storage capability. Through studying these materials, it is clear that the rational design and engineering of micro/nanostructures of anode materials can effectively address the issues of inorganic anode materials (Fig. 1), as has already been confirmed in many electrochemical related fields [18, 19]. Thus, numerous efforts have been focused on the selection of inorganic materials, design and construction of anodic structures, and investigation of their electrochemical performances in PIBs.

Over the past several years, we have witnessed exponential growth in high-quality works regarding PIBs, turning this into a highly competitive field of research. Given the fact that the anode materials for PIBs are rapidly developing and have achieved great progress thus far, we believe that a timely review is necessary, not only to summarize the latest progress but also to provide a better understanding and general guidance on the design and engineering of anode materials. In this review, we firstly summarize the representative work of PIBs and categorize them into several groups based on different anodic compositions. Then, in each part, we introduce the representative work from the viewpoints of anodic design concepts, nanoscale fabrication/engineering methods, and electrochemical performances. The comparisons of different electrochemical performances and storage mechanisms of various anode materials are presented. Finally, based on the progress achieved so far, the shortcomings of existing methods for making anodic structures, as well as the possible solutions and strategies are discussed. Lastly, future perspectives on the development and real-world applications of PIBs are given.

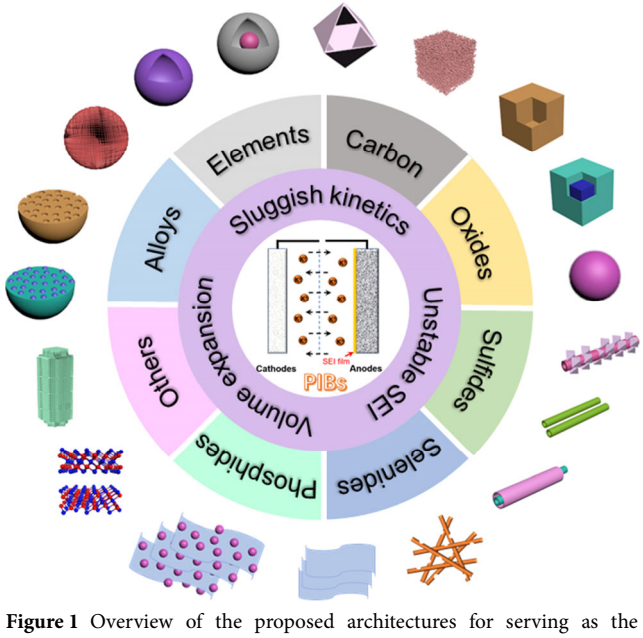

Figure 1 Overview of the proposed architectures for serving as the anodes of PIBs.

2 Challenges of PIBs

Similar to LIBs, K^+ ions move back and forth between the cathode and anode with electrolyte serving as the transport medium in PIBs, known as the "rocking chair" mechanism. The main challenges to achieving high energy density and good cyclability of PIBs include the sluggish K^+ reaction kinetics in solid electrodes and the large volume expansion of electroactive materials, which not only causes the crack of active materials but also results in unstable solid electrolyte interphase (SEI). To overcome these challenges, efforts from both the rational design of electrode materials and the exploration of new electrolytes are required.

Sluggish K^+ reaction kinetics. Due to a much larger ionic size (1.38 Å) of K^+ ion than these of Li^+ (0.76 Å) and Na^+ (1.02 Å), it is more difficult for K^+ ions to intercalate into electroactive materials than Li^+ and Na^+ ions [20–22]. One well-established approach is to reduce the dimension and size of active materials. Considering the large size of K^+, nanostructured materials display improved K^+ reaction kinetics due to the shortened ion diffusion length, leading to the enhanced rate capability and reversible capacity. For layered-structured materials, expanding the interlayer distance can significantly improve K^+ mobility due to the smaller diffusion barrier relative to the pristine material. For example, heteroatom doping can enlarge the interlayer spacing of carbonaceous materials, resulting in fast K^+ ion transport and improved structural integrity [23].

Large volume expansion. During potassiation process, the anode materials undergo large volume expansion due to the insertion of K^+ ions. Specifically, graphite exhibits ~ 61% volume expansion after potassiation, six times larger than that upon lithiation [24]. For alloy-based materials, the situation is even worse. The volume variation of Sn_4P_3 upon deep potassiation is ~ 600% [25], which not only leads to the pulverization of electroactive material but also isolates part of the electrode from electrical contact, resulting in fast capacity decay. It is known that a thin and stable SEI layer can greatly improve the electrochemical performance of batteries because it prevents the continuous reduction of organic electrolytes, thus enabling the battery to operate below the reduction voltage of electrolytes. However, as discussed before, the volume change of anode materials triggers the breakage and regeneration of SEI layers. As a consequence, SEI layers grow continuously upon reiterative charge/discharge processes, giving rise to low Coulombic efficiencies and fast capacity decay [26–28]. Besides, since most electrochemical tests are carried out in half-cell configuration, the intrinsic active properties of K metal would trigger numerous side reactions with the electrolyte, forming interphase layers with complicated compositions [29, 30]. In addition, the serious volume expansion during the plating/stripping process would destroy the as-formed SEI layers, and expose fresh K metal to the electrolyte, generating new SEI. Therefore, it is crucial to promote the formation of a stable SEI layer to ensure the cyclability of PIBs in both full-cell and half-cell configurations.

Considerable efforts have been devoted to optimizing the composition, morphology, and local atomic structure of anode materials through nanoscale engineering to meet the above challenges. These approaches have been demonstrated on various anode materials, including carbon materials, alloys, oxides, sulfides, to result in improved electrochemical performance. In the following sections, we will introduce the synthesis and nanoscale engineering concepts of anode materials, and then comprehensively discuss the different types of anode materials, along with the listing of representative works.

3 Engineering concepts of PIB anode materials

As demonstrated in this review, various strategies have been proposed to design and synthesize intriguing structures of anode materials to resolve the issues encountered by PIBs. In general, an optimal structure of anode materials should possess the following characteristics: (i) high electrical conductivity to facilitate electron transport; (ii) short ion diffusion length with good electrolyte penetration; (iii) ample space to accommodate volume change; and (iv) special structure to enable stable SEI layers during cycles. For the engineering concepts of PIB anode materials, the discussions are listed below.

With regard to the geometry of materials, they are typically divided into zero-dimensional (0D), one-dimensional (1D), two-dimensional (2D), and three-dimensional (3D) structures. The 0D anode materials (e.g., particles, quantum dots) have been widely studied as the anode materials for PIBs, especially for transition metal compounds. However, the isolated 0D particles tend to aggregate during electrochemical reactions, degrading their K^+ storage performance. 1D nanostructures, including nanofibers, nanotubes, nanowires, and nanorods, are characterized by large aspect ratios, short ion diffusion paths, and efficient electron transport. Moreover, the 1D nanostructure can maintain excellent mechanical stability over several cycles of K^+ insertion and extraction, which is extremely suitable for materials undergo conversion and alloying reactions. To date, several methods, such as hydrothermal, electrodeposition, electrospinning, and chemical vapor deposition techniques, have been employed to fabricate the 1D nanostructures. The 2D nanostructures with large specific surface areas have attracted increasing attention in PIBs. The large surface area provides abundant sites for K^+ adsorption and insertion, enabling fast reaction kinetics. However, the serious stacking and aggregation issues for 2D nanostructures significantly reduce the surface areas and hinder ion transport, which has to be resolved to enhance their electrochemical performances. The 3D architectures are usually assembled by 2D nanosheets, 1D nanowires, or 0D particles, thus enjoying the advantages arising from the subunits. Typically, 3D nanostructures contain numerous pores, voids, and channels, ensuing the easy penetration of electrolytes and maintaining excellent structural integrity. In addition, 3D architectures have better processability because of the inhibited aggregation. As a result, the electrochemical performance can be enhanced compared to the bulk counterparts.

The design and construction of nanoscale structures is also a popular approach to improve K^+ storage performances of different dimensional anode materials. Main nano-structures for anode materials include porous, hollow, and core (yolk)–shell. To obtain these structures, approaches like template, hydrothermal/solvothermal, electrospinning, and MOFs-derived methods, are routinely utilized. Taking carbonaceous materials with porous structures as an example, high-temperature carbonization and template methods are commonly employed, since voids and space can be created by the gas produced during the carbonization process, and using templates. It should be emphasized that the template method tends to generate hierarchical porous architectures, which usually have a high specific surface area for ion storage. For metal oxides, sulfides, selenides, nitrides, phosphides, and other materials, diverse approaches are used to create nano-structures. With delicate nano-structures, the challenge of anode materials is often how to maintain structural integrity during electrochemical processes. As discussed throughout this work, although the design and construction of nano-structures for anode materials is one of the most efficient approaches to increase the PIB performance, it creates serious challenges in understanding the charge storage mechanism of PIBs, which requires efforts from both theory and experiments.

4 Carbon materials

Carbon materials with high electrical conductivity and tunable structures are promising anode materials for PIBs [31, 32]. The above merits facilitate the transport pathways of electrons and K^+ ions, contributing to outstanding cyclic performance. To better study the in-depth relationships between structure and electrochemical performance, keeping the different storage mechanisms of K^+ ions within various types of carbon materials in mind, we deliberately categorized the carbon anodes into graphene, carbon tubes, carbon fibers, hollow carbon, and porous carbon, as shown in Table 1.

4.1 Graphene

Graphene, a type of carbon material with atomic-layer thickness, has attracted tremendous interests because of its high theoretical specific surface area (2,630 $m^2 \cdot g^{-1}$), exciting mechanical characteristics, and excellent electron mobility [33–35]. Various methods have been reported to prepare graphene nanosheets. In the battery field, reduced graphene oxide (rGO) is the most widely adopted form. rGO has shown remarkable K^+ storage performance, owing to its abundant active sites as well as an enlarged interlayer distance. Simon and co-workers synthesized 3D rGO aerogel through a freeze-drying method for K^+ storage [36], as shown in Fig. 2(a). By optimizing the electrolytes and drying methods, the 3D rGO aerogel delivered a high reversible capacity of 267 $mAh \cdot g^{-1}$ at C/3 rate, along with 78% capacity retention after 100 cycles. Even increasing the rate to 1.6 C, a high reversible capacity of 125 $mAh \cdot g^{-1}$ was obtained after running 500 cycles. Chen et al. also investigated the correlation between microstructure and electrochemical performance of rGO in PIBs [37]. They revealed that the K^+ storage performance strongly depends on the thermal annealing temperature on account of the difference in microstructure (Fig. 2(b)). The rGO graphitized at 2,500 °C exhibited ultralong cyclic stability over 2,500 cycles, resulting from the expanded interlayer distance and the graphite-like structure [37].

Heteroatom (i.e. nitrogen, sulfur, boron, or phosphorous)-doping has been demonstrated to be an effective strategy to enhance the electrical conductivity and effectively promote the ion storage properties of graphene [38–40]. For instance, Ju et al. prepared few-layer N-doped graphene nanosheets as anode materials for PIBs, using dicyandiamide and coal tar pitch as raw materials [41]. As displayed in Fig. 2(c), by virtue of the large K^+ storage capacity arising from high specific surface area and abundant nitrogen doping sites (14.68 at.%), the few-layer N-doped graphene displayed a competitive reversible capacity of 320 $mAh \cdot g^{-1}$ after 60 cycles at 50 $mA \cdot g^{-1}$, superior rate capability, and excellent cyclability under a high current density (150 $mAh \cdot g^{-1}$ after 500 cycles at 500 $mA \cdot g^{-1}$). Qiu et al. reported the use of N and P co-doped vertical graphene sheets grown on carbon cloth as a binder-free anode for PIBs [42]. Considering the advantageous structures with enriched active sites, large interlayer spacing and accessible surface, highly conductive network, and robust structural integrity, the achieved PIBs exhibited a high capacity reaching 344.3 $mAh \cdot g^{-1}$, remarkable rate capability (~ 46.5% capacity retention at 2.0 $A \cdot g^{-1}$), and prominent long-term cycle stability (~ 82% capacity retention even after 1,000 cycles).

Table 1 Comparison of different carbon-based anode materials of PIBs

Anodes	Morphology	Synthesis method	Specific capacity	Cyclic performance	Ref.
rGO aerogel	3D porous structure	Chemical reduction	92 mAh·g^{-1} at 6.7 C	267 mAh·g^{-1} after 100 cycles at 1/3 C	[36]
rGO	Curved flakes	Heat treatment	~ 80 mAh·g^{-1} at 10 C	88.4 mAh·g^{-1} after 2,500 cycles at 100 mA·g^{-1}	[37]
N-doped graphene	Few-layered structure	Bottom-up synthesis	~ 320 mAh·g^{-1} at 50 mA·g^{-1}	150 mAh·g^{-1} after 500 cycles at 500 mA·g^{-1}	[41]
N, P co-doped graphene/carbon cloth	Hierarchical porous layered structure	Microwave plasma-enhanced chemical vapor deposition	46.5% capacity retention at 2,000 mA·g^{-1}	82% capacity retention after 1,000 cycles	[42]
F-doped graphene foam	Hollow porous structure	Solid-state method	—	165.9 mAh·g^{-1} after 200 cycles at 500 mA·g^{-1}	[43]
Carbon microtube array	Porous structure	Hydrothermal method followed with annealing	273.6 mAh·g^{-1} at 1,000 mA·g^{-1}	177.6 mAh·g^{-1} after 2,000 cycles at 2,000 mA·g^{-1}	[47]
N-doped carbon nanotube	Nanotubular structure	Precursor-derived method	44 mAh·g^{-1} at 9.56 C	91.8% capacity retention after 5,000 cycles	[48]
N-doped cup-stacked carbon nanotube	Interconnected network with interspace inside	Chemical vapor deposition	75 mAh·g^{-1} at 1,000 mA·g^{-1}	236 mAh·g^{-1} after 100 cycles at 20 mA·g^{-1}	[51]
SMCF@CNTs	Flexible and porous structure	Electrospinning combined with annealing	108 mAh·g^{-1} at 5.0 C	193 mAh·g^{-1} after 300 cycles at 1.0 C	[52]
N-doped carbon nanofiber	Porous tubular structure	Precursor-derived method	101 mAh·g^{-1} at 20,000 mA·g^{-1}	146 mAh·g^{-1} after 4,000 cycles at 2,000 mA·g^{-1}	[56]
N-doped carbon nanofiber	Hierarchical porous structure	Electrospinning combined with annealing	197 mAh·g^{-1} at 50 mA·g^{-1}	65 mAh·g^{-1} after 346 cycles at 100 mA·g^{-1}	[57]
Multichannel carbon fibers	Free-standing porous structure	Electrospinning combined with annealing	420.1 mAh·g^{-1} at 50 mA·g^{-1}	110.9 mAh·g^{-1} after 2,000 cycles at 2,000 mA·g^{-1}	[58]
N-doped carbon nanofiber	Porous structure	Precursor-derived method	84.7 mAh·g^{-1} at 5 C	103.4 mAh·g^{-1} after 500 cycles at 2 C	[61]
N-doped porous carbon	Porous and hollow structure	Template method (polystyrene spheres)	94 mAh·g^{-1} at 10,000 mA·g^{-1}	157 mAh·g^{-1} after 12000 cycles at 2,000 mA·g^{-1}	[65]
Carbon nanosphere	Hollow structure	Template method (SiO_2)	370.2 mAh·g^{-1} at 2,000 mA·g^{-1}	Stable for 5,000 cycles at 2,000 mA·g^{-1}	[66]
N-doped carbon nanosphere	Hollow structure	Template method (SiO_2)	141 mAh·g^{-1} at 2,000 mA·g^{-1}	154 mAh·g^{-1} after 2,500 cycles at 1,000 mA·g^{-1}	[67]
N-doped carbon	Necklace-like porous structure	Template method (ZnO)	293.5 mAh·g^{-1} at 100 mA·g^{-1}	161.3 mAh·g^{-1} after 1600 cycles at 1000 mA·g^{-1}	[68]
Hard carbon	Honeycomb porous structure	Template method (carbon quantum dots)	42 mAh·g^{-1} at 3,200 mA·g^{-1}	195.3 mAh·g^{-1} after 150 cycles at 100 mA·g^{-1}	[69]
N-doped carbon	Hollow structure	Template method (carbon quantum dots)	145 mAh·g^{-1} at 4,000 mA·g^{-1}	160 mAh·g^{-1} after 800 cycles at 1,000 mA·g^{-1}	[70]
Bi-doped carbon nanosheets	Porous structure	Template method (NaCl)	107 mAh·g^{-1} at 20,000 mA·g^{-1}	271 mAh·g^{-1} after 1,000 cycles at 1,000 mA·g^{-1}	[71]
N-doped carbon sphere	Interconnected porous nanosheets	Template method (NaCl)	54 mAh·g^{-1} at 30,000 mA·g^{-1}	117.2 mAh·g^{-1} after 3,000 cycles at 1,000 mA·g^{-1}	[72]
N-doped graphitic nanocarbons	Porous, defect-rich structure	Precursor-derived method	280 mAh·g^{-1} at 50 mA·g^{-1}	189 mAh·g^{-1} after 200 cycles at 200 mA·g^{-1}	[73]
N-rich carbon onion	Hollow nanosheets	Precursor-derived method	105 mAh·g^{-1} at 10,000 mA·g^{-1}	132 mAh·g^{-1} after 5,000 cycles at 2,000 mA·g^{-1}	[74]
Graphitic carbon nanocages	Interconnected hollow structure	Precursor-derived method	175 mAh·g^{-1} at 35 C	—	[75]
Carbon material	Porous structure	Precursor-derived method (coal)	260 mAh·g^{-1} at 50 mA·g^{-1}	118 mAh·g^{-1} after 1200 cycles at 1,000 mA·g^{-1}	[76]
P-doped hard carbon	Porous structure	Precursor-derived method (epoxy resin)	381.9 mAh·g^{-1} at 100 mA·g^{-1}	260 mAh·g^{-1} after 1,000 cycles at 200 mA·g^{-1}	[77]
Hard carbon	Macroporous structure	Precursor-derived method (epoxy resin)	336 mAh·g^{-1} at 10 mA·g^{-1}	—	[78]
Graphitic carbon nanospring	Hierarchical porous structure	Precursor-derived method (epoxy resin)	121.7 mAh·g^{-1} at 5,000 mA·g^{-1}	99.9 mAh·g^{-1} after 10,000 cycles at 2,000 mA·g^{-1}	[79]
Carbon shells	Hierarchical porous structure	Precursor-derived method (MOFs)	320 mAh·g^{-1} at 50 mA·g−1	65 mAh·g^{-1} after 900 cycles at 2,000 mA·g^{-1}	[80]
N-doped carbon	Porous structure	Precursor-derived method (MOFs)	186.2 mAh·g^{-1} at 2,000 mA·g^{-1}	231.6 mAh·g^{-1} after 2,000 cycles at 500 mA·g^{-1}	[81]
Hard-soft composite carbon	Porous carbon nanosphere	Precursor-derived method (3,4,9,10-perylenetetracarboxylic dianhydride)	81 mAh·g^{-1} at 10 C	118 mAh·g^{-1} after 200 cycles at 1 C	[82]

(Continued)

Anodes	Morphology	Synthesis method	Specific capacity	Cyclic performance	Ref.
N-doped carbon nanosphere	Porous structure	Precursor-derived method (polyaniline-co-polypyrrole)	423 mAh·g^{-1} at 50 mA·g^{-1}	305 mAh·g^{-1} after 660 cycles at 200 mA·g^{-1}	[83]
S, N co-doped carbon	Porous structure	Precursor-derived method (polyacrylonitrile)	293.8 mAh·g^{-1} at 100 mA·g^{-1}	143.6 mAh·g^{-1} after 1,200 cycles at 3,000 mA·g^{-1}	[84]
N-doped carbon	Porous structure	Precursor-derived method (polyacrylonitrile)	280 mAh·g^{-1} at 25 mA·g^{-1}	—	[85]
Ordered carbon	Mesoporous structure	Precursor-derived method (sucrose)	144.2 mAh·g^{-1} at 1,000 mA·g^{-1}	146.5 mAh·g^{-1} after 1,000 cycles at 1,000 mA·g^{-1}	[86]
Hard carbon	Porous structure	Precursor-derived method (sucrose)	—	290 mAh·g^{-1} after 50 cycles at 25 mA·g^{-1}	[87]
Carbon bowls	Porous hollow structure	Precursor-derived method (biomass)	304 mAh·g^{-1} at 100 mA·g^{-1}	133 mAh·g^{-1} after 1,000 cycles at 1,000 mA·g^{-1}	[88]
N-doped carbon	Hierarchical porous carbon	Precursor-derived method (biomass)	263.6 mAh·g^{-1} at 100 mA·g^{-1}	119.9 mAh·g^{-1} after 1,000 cycles at 1,000 mA·g^{-1}	[89]
Hard carbon	Porous structure	Precursor-derived method (biomass)	32 mAh·g^{-1} at 1/5 C	—	[90]
N-rich hard carbon	Hierarchical porous carbon	Precursor-derived method (biomass)	154 mAh·g^{-1} at 72 C	Stable for 4,000 cycles	[91]
Carbon wires	Porous structure	Precursor-derived method (biomass)	164 mAh·g^{-1} at 1,000 mA·g^{-1}	122 mAh·g^{-1} after 1,000 cycles at 5,000 mA·g^{-1}	[92]
Graphite-structured hard carbon	Porous structure	Precursor-derived method (biomass)	67 mAh·g^{-1} at 1.3 C	90% capacity retention after 300 cycles	[93]
N-doped carbon	Hierarchical porous structure	Precursor-derived method (ammonium chloride/sodium polyacrylate)	193.1 mAh·g^{-1} at 500 mA·g^{-1}	296.8 mAh·g^{-1} after 200 cycles at 50 mA·g^{-1}	[94]
N, S co-doped carbon	Hierarchical porous structure	Precursor-derived method (sodium polyacrylate/thiourea)	158.7 mAh·g^{-1} at 500 mA·g^{-1}	156.8 mAh·g^{-1} after 1,000 cycles at 500 mA·g^{-1}	[95]
Carbon framework	Hierarchical porous structure	Precursor-derived method (polyacrylate/sodium chloride/Zn nanoparticles)	76.7 mAh·g^{-1} at 10,000 mA·g^{-1}	211.5 mAh·g^{-1} after 50 cycles at 50 mA·g^{-1}	[96]
Carbon network	Hierarchical porous structure	Precursor-derived method (melamine foam)	160 mAh·g^{-1} at 1,000 mA·g^{-1}	118 mAh·g^{-1} after 900 cycles at 1000 mA·g^{-1}	[97]
N-doped carbon	Porous structure	Precursor-derived method (pitch/urea)	162.5 mAh·g^{-1} at 2,000 mA·g^{-1}	167 mAh·g^{-1} after 1,000 cycles at 1,000 mA·g^{-1}	[98]
N, S co-doped carbon microbox	Hollow porous structure	Precursor-derived method (ZIFs)	155.6 mAh·g^{-1} at 2,000 mA·g^{-1}	180.5 mAh·g^{-1} after 1,000 cycles at 500 mA·g^{-1}	[99]
N-doped carbon nanotubes@carbon	Porous structure	Precursor-derived method (ZIFs)	339 mAh·g^{-1} at 50 mA·g^{-1}	141 mAh·g^{-1} after 1,000 cycles at 1,000 mA·g^{-1}	[100]
Carbon nanoplate	Porous structure	Precursor-derived method (ZIFs)	120 mAh·g^{-1} at 5,000 mA·g^{-1}	192 mAh·g^{-1} after 5,200 cycles at 1,000 mA·g^{-1}	[101]

Besides building rGO architectures, various graphene architectures prepared via directly thermal annealing processes can also be utilized as anodes for PIBs. The as-prepared graphene structures feature a high graphitic degree and an enlarged interlayer distance. For example, few-layered F-doped graphene foam was synthesized via a high-temperature solid-state synthetic route [43]. Benefitting from the synergistic effects endowed by the F-doped species, high specific surface area, and mesoporous membrane structures, both ions and electrons have fast transportation rates in F-doped graphene. Combined with the abundant active sites for K^+ storage, the corresponding PIBs exhibited excellent electrochemical performances, especially in terms of rate capability and cyclic performance under high rates (165.9 mAh·g^{-1} after 200 cycles at 500 mA·g^{-1}).

4.2 Carbon tubes

Carbon tubes feature high electrical conductivity, fast transport of ions and electrons, which result in enhanced rate performance and prolonged cyclic lifetime [44–46]. Recently, carbon tubes have aroused great interests as anode materials for PIBs. For instance, with sycamore leaves as the raw material, a porous carbon microtube array derived from the carbon quantum dots was fabricated (Fig. 3(a)) [47]. Owing to the merits including multi-hole cross profile, high specific surface area, and larger interlayer spacing distance, porous carbon microtube arrays delivered a record-high cyclic performance with a specific capacity reaching 177.6 mAh·g^{-1} even after 2,000 cycles under 2.0 A·g^{-1}. Meanwhile, polyaniline-derived N-doped carbon nanotubes were also confirmed to have remarkable K^+ storage performance when used as the anode of PIBs [48].

Due to a large length-to-width ratio, carbon tubes can easily form free-standing electrodes with intriguing network architectures, which avoid the use of nonactive components, such as binders, conductive additives, and current collectors [49, 50]. As a typical example, Xu and co-workers employed free-standing N-doped cup-stacked carbon nanotube mats as a PIB anode (Fig. 3(b)) [51]. Benefitting from the nanosized characteristics and interconnected flexible structure, the as-prepared anode exhibited remarkable electrochemical performances with a reversible capacity of 323 mAh·g^{-1} and a good cyclic performance with a capacity of 75 mAh·g^{-1} after 100 cycles at 0.02 A·g^{-1}. Additionally, Shen et al. employed self-supporting carbon nanotubes encapsulated into sub-micron carbon fiber (SMCF@CNTs) for K^+ storage [52], as shown in Fig. 3(c). Electrochemical testing revealed a combined capacitive and diffusion-controlled K^+ storage mechanism, and the

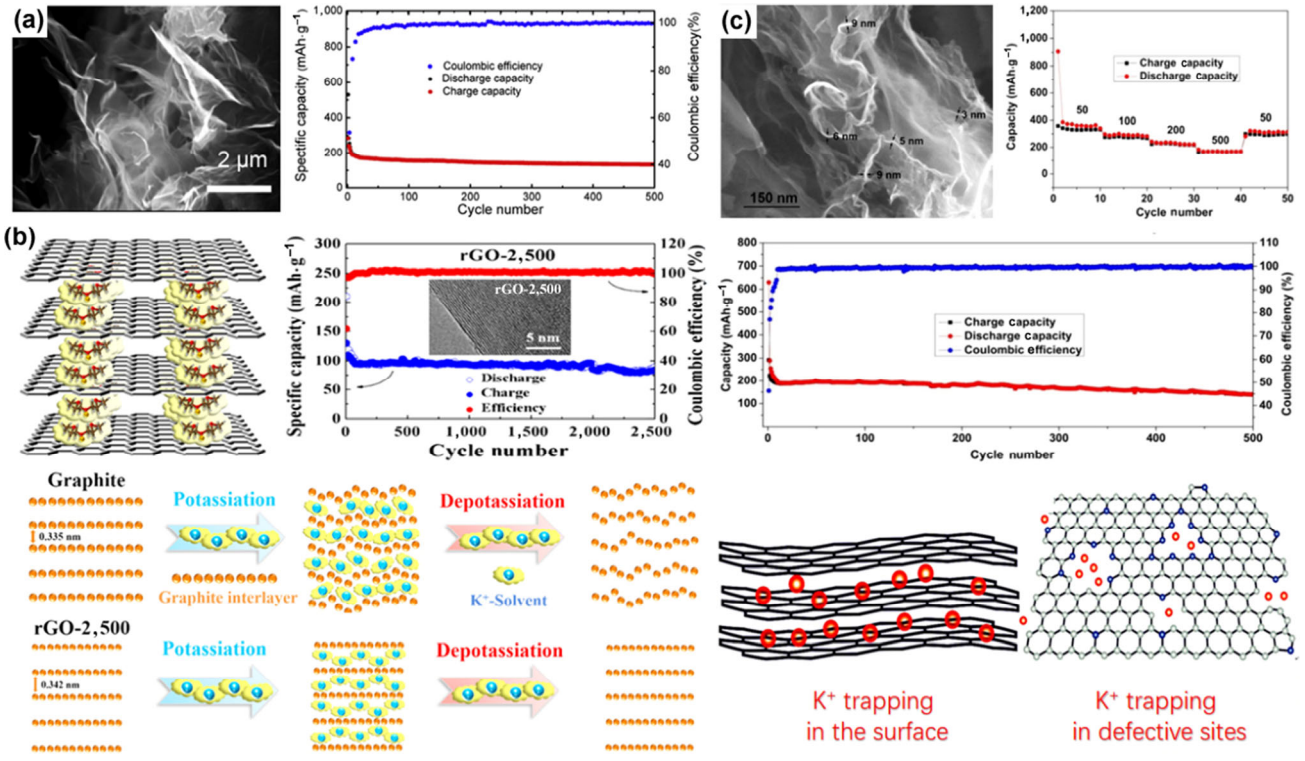

Figure 2 (a) Scanning electron microscopy (SEM) image of rGO sheets and the K^+ storage performance at 1.6 C. Reprinted with permission from Ref. [36], © Elsevier B.V. 2019. (b) Schematic illustration of K^+ storage in rGO sheets, the long-term cycle tests at 0.1 mA·cm^{-2}, and the comparison of K^+ storage mechanisms in graphite and rGO graphitized at 2,500 °C. Reproduced with permission from Ref. [37], © American Chemical Society 2019. (c) SEM image of few-layer N-doped graphene, the electrochemical performance of PIBs, and the schematic of mixed mechanisms for K^+ storage. Reprinted with permission from Ref. [41], © Elsevier B.V. 2017.

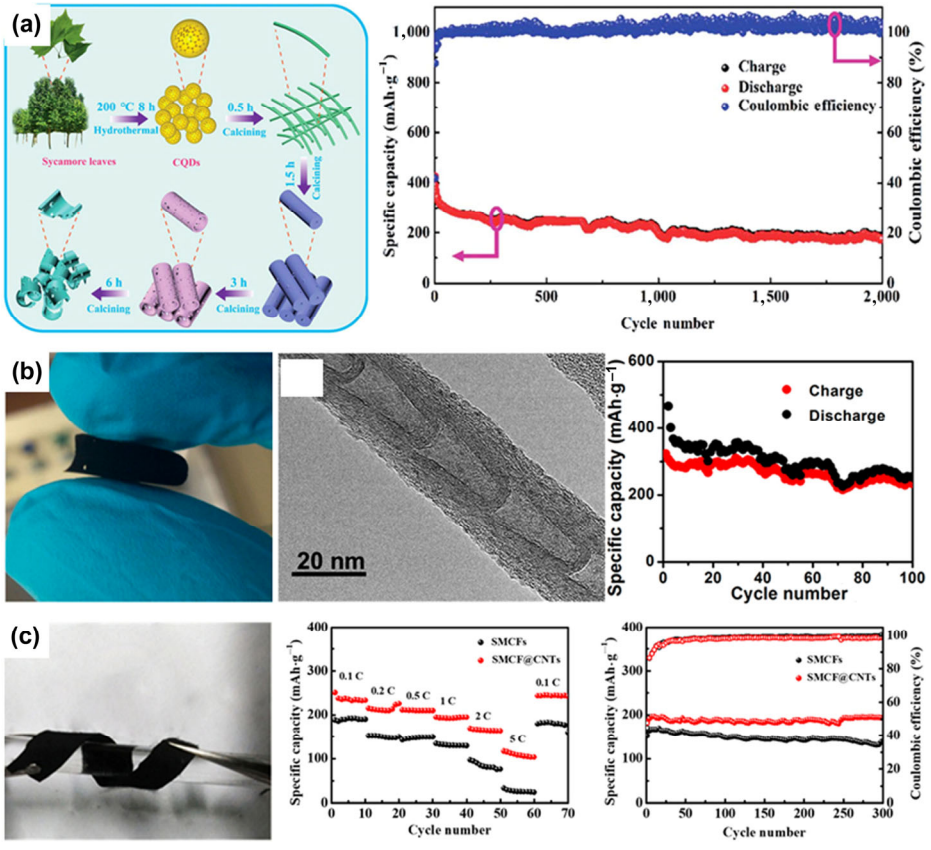

Figure 3 (a) Schematic illustration of the product morphology variation with different sintering times and the K^+ storage performance at 2.0 A·g^{-1}. Reprinted with permission from Ref. [47], © The Royal Society of Chemistry 2019. (b) Free-standing N-doped cup-stacked carbon nanotube and the cycle performance at 20 mA·g^{-1}. Reprinted with permission from Ref. [51], © American Chemical Society 2018. (c) Self-supporting carbon nanotubes encapsulated in sub-micron carbon fiber and the electrochemical performance of PIBs. Reprinted with permission from Ref. [52], © American Chemical Society 2019.

SMCF@CNTs anode displayed high reversible capacities of 236 and 108 mAh·g^{-1} at 0.1 and 5.0 C, respectively, which maintained over 193 mAh·g^{-1} after 300 cycles at 1.0 C. The above results signify the great potential of carbon tubes as the anodes for flexible PIBs.

4.3 Carbon fibers

Besides graphene and carbon tubes, carbon fibers have also been studied because of their high electrical conductivity and short ion diffusion length [53–55]. Toward this end, using N-doped carbon nanofibers as a high-performance anode for PIBs was reported by Lei et al. [56]. Theoretical simulations have predicted that N-doping can enhance the K-adsorption ability and K^+ diffusivity, especially pyrrolic and pyridinic N. The theoretical results indicated that the N-doping was responsible for the excellent electrochemical performance (a high reversible capacity of 248 mAh·g^{-1} at 25 mA·g^{-1}, an excellent rate performance of 101 mAh·g^{-1} at 20 A·g^{-1}, as well as great long-term cyclic stability for 4,000 cycles). Moreover, carbon fiber architecture with a high N content and a hierarchical porous structure was also reported [57]. The unique structure not only provided intrinsic electron pathways and ion transport channels but also accommodated the volume change by providing sufficient free space during cycles. Finally, the anode displayed a high capacity of 197 mAh·g^{-1} at 50 mA·g^{-1} and good cyclic performance over 346 cycles at 100 mA·g^{-1}. To further investigate the effects of microstructures on the electrochemical performances of carbon fibers, Zheng et al. fabricated multi-channel carbon fibers as freestanding anodes of PIBs [58]. The unique multi-channel in amorphous carbon fibers can alleviate the volume expansion and allow the penetration of electrolyte. At the same time the doping of heteroatoms can generate defective sites and ameliorate the electrical conductivity [59, 60]. As a consequence, the multi-channel carbon fibers displayed significantly enhanced K^+ storage performances (420 mAh·g^{-1} at 50 mA·g^{-1}, and 111 mAh·g^{-1} over 2,000 cycles at 2.0 A·g^{-1}). Similarly, chitin-derived porous N-doped carbon nanofibers also showed excellent electrochemical performance in PIBs [61].

4.4 Porous carbon

Porous carbons usually have good electrical conductivity, abundant pores, high specific surface areas, easily accessible channels, and a large number of active sites [62–64], showing great possibility in PIBs. Especially, porous nanocarbons would show better electrochemical performance: (i) Nanocarbon structures can provide abundant active sites for K^+, contributing to the pseudo-capacitive type behavior and thus specific capacity; and (ii) the elastic feature can effectively accommodate the volume expansions during potassiation/depotassiation. Porous nanocarbons with hierarchical structures can be easily fabricated using a template method. So far, different templates including polystyrene spheres [65], SiO_2 [66, 67], ZnO [68], carbon quantum dots [69, 70], and NaCl crystals [71, 72], have been used. For instance, with polystyrene spheres as the template, Yu and co-workers have fabricated a 3D interconnected N-doped hierarchical porous carbon and measured its electrochemical performance in PIBs (Fig. 4(a)) [65]. In virtue of reduced ion/electron diffusion distances and N-doping in porous carbon (as revealed by the theoretical calculations), it exhibited excellent electrochemical performances (292 mAh·g^{-1} at 0.1 A·g^{-1}, 94 mAh·g^{-1} at 10 A·g^{-1}, and 157 mAh·g^{-1} after 12,000 cycles at 2.0 A·g^{-1}). Guo et al. synthesized a highly pyrrolic/pyridinic-N-doped necklace-like hollow carbon material using ZnO as a scarify template (Fig. 4(b)), and employed it as a novel freestanding anode for PIBs [68]. Theoretical simulations verified that the pyrrolic- and pyridinic-N species have a great K-adsorption capability (Fig. 4(b)). Thanks to the multiple structural features: hierarchical pore structures, 1D hollow structure, N atom doping, and high specific surface area, the necklace-like carbon nanofibers exhibited fast intercalation/deintercalation of K^+ ions, good structural stability, and outstanding electrochemical performance (161 mAh·g^{-1} after 1,600 cycles at 1.0 A·g^{-1}).

The precursor-derived method can also produce porous carbon architectures with high efficiencies. Using ethylenediaminetetraacetic acid nickel coordination compound as the precursor, Alshareef et al. fabricated N-doped, defect-rich graphitic nanocarbons as a high-performance PIB anode [73]. The results revealed that the K^+ storage mechanism of carbon architecture was similar to that of graphite, and the structural features provided additional active sites for the potassiation process. Finally, the as-prepared carbon anodes exhibited a high specific capacity reaching 280 mAh·g^{-1} at 50 mA·g^{-1}, good rate performance, and long cyclic lifetime. Moreover, a Co-hexamine coordination framework was also utilized as the precursor to prepare porous and hollow carbon architecture, and electrochemical tests revealed an excellent K^+ storage performance [74]. Besides the organic-based precursor, Ketjen carbon black was also selected as the precursor for synthesizing carbon nanocages with an interconnected hollow structure [75]. This approach can be easily scaled up because Ketjen carbon black was commercially available. The nanocage showed extremely high specific capacity and excellent cyclic stability, when used as the anode materials for PIBs.

Porous carbonaceous materials are the extensively studied for PIBs, to make them, the precursor-derived strategy is preferred because it is simpler and more efficient than the template method without the need to remove the template. The precursor-derived strategy commonly starts with the selection/preparation of precursors containing organic molecules, and then the precursors are treated by thermal annealing under high temperature, and followed by post-treatments. To date, coal [76], epoxy resin [77–79], metal-organic frameworks (MOFs) [80, 81], 3,4,9,10-perylenetetracarboxylic dianhydride [82], polyaniline-co-polypyrrole [83], polyacrylonitrile [84, 85], sucrose [86, 87], biomass [88–93], ammonium chloride/sodium polyacrylate [94], sodium polyacrylate/thiourea [95], polyacrylate/sodium chloride/Zn nanoparticles [96], melamine foam [97], pitch/urea [98], and zeolite imidazole ester frameworks (ZIFs) [99–101] have been used as precursors to synthesize various porous carbon materials for PIBs. Taking phosphoric acid linked epoxy resin as a representative example, porous carbon obtained by massive carbonizing a phosphoric acid solidified epoxy resin contains P–C and P–O bonds, which can serve as active sites for K^+ storage (Fig. 5(a)) [77]. Electrochemical tests revealed that the as-prepared P-doped hard carbon possessed a high reversible capacity reaching 179 mAh·g^{-1} at 5.0 A·g^{-1}, and high capacity retention of 260 mAh·g^{-1} after 1,000 cycles at 0.2 A·g^{-1}. *In situ* characterizations (Fig. 5(a)) confirmed that excellent electrochemical performance could be attributed to the formed P-containing bonds, which can enhance the adsorption to alkali metal ions and participate in electrochemical redox reactions by forming Li_xPC_y. Moreover, Lin and co-workers reported a highly oriented mesoporous graphitic carbon nanospring made from epoxy resin [79]. Benefitting from the high orientation, a large amount of active edge-plane sites, and mesoporous structure, the spring-like structure could efficiently alleviate the volume strain during electrochemical processes. Consequently, an excellent

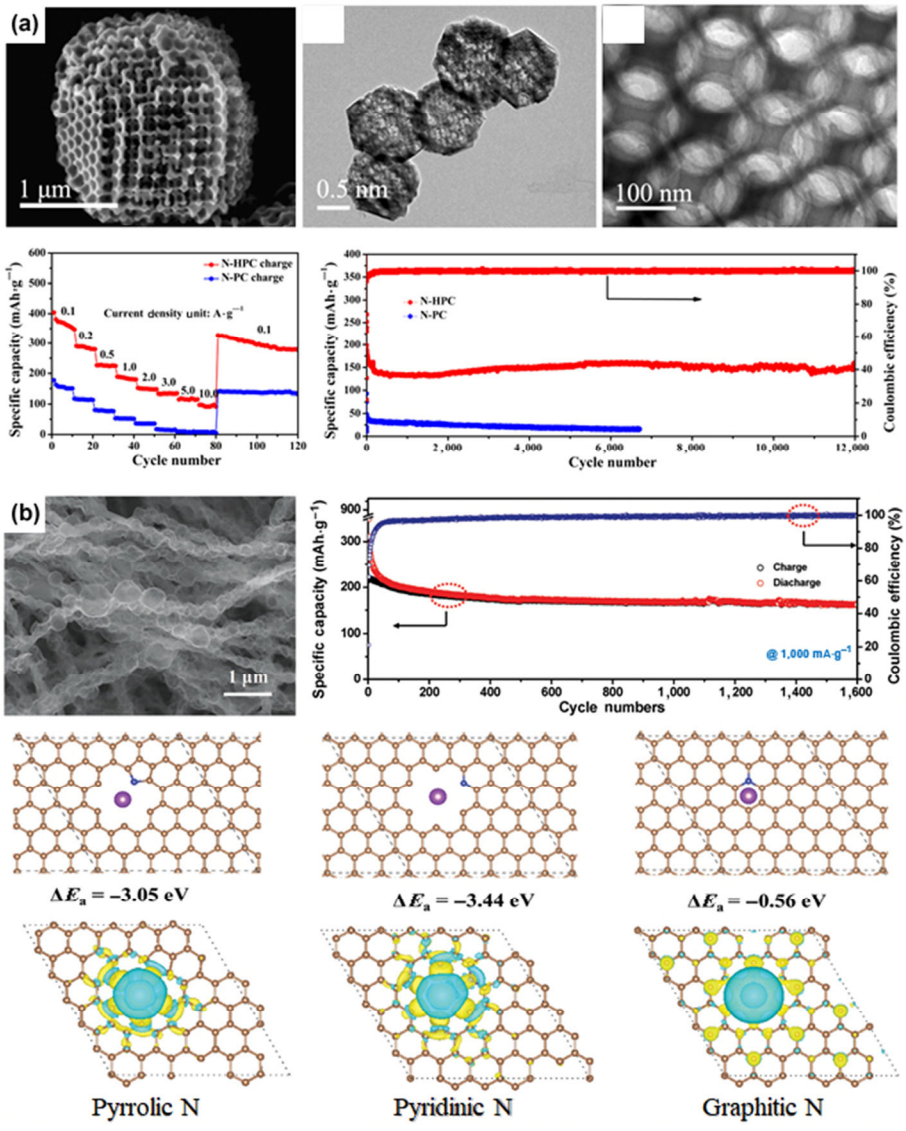

Figure 4 (a) SEM image of N-doped hierarchical porous carbon and the K^+ storage performance at 2.0 $A·g^{-1}$. Reprinted with permission from Ref. [65], © American Chemical Society 2019. (b) SEM image of necklace-like N-doped hollow carbon, long-term cycle tests at 1.0 $A·g^{-1}$, and theoretical simulations on the K-adsorption abilities of different nitrogen species. Reprinted with permission from Ref. [68], © The Royal Society of Chemistry 2019.

electrochemical performance including high reversible capacity (541 $mAh·g^{-1}$ at 50 $mA·g^{-1}$), high rate capability, and stable cyclic performance (100 $mAh·g^{-1}$ after 10,000 cycles at 1,000 $mA·g^{-1}$) were achieved. Besides, polyaniline-co-polypyrrole was selected as the precursor for preparing edge-N-doped carbon architecture (Fig. 5(b)) [83]. Owing to the different thermal stabilities, the ordinal release of radicals was generated from pyrrole and aniline. Through optimizing the pyrolysis conditions, carbon-based anodes displayed remarkable K^+ storage performances (74 $mAh·g^{-1}$ at 5.0 $A·g^{-1}$, and 305 $mAh·g^{-1}$ after 660 cycles at 0.2 $A·g^{-1}$). All these results proved that the precursor-derived strategy was promising for efficiently generating the porous carbon architectures.

Although carbonaceous materials exhibited impressive electrochemical performances when working as the anodes of PIBs, several shortcomings still exist, restricting their commercialization. The first one lies in the sluggish K^+ diffusion kinetics induced by the large ionic radius and the narrow carbon interlayer spacings. This can be well reflected by the poor rate capability under high current densities. The design and construction process of carbon architectures is another major challenge. The micro/nano-structured carbonaceous materials commonly require complex synthesis procedures and harsh experimental conditions; therefore, the obtained carbonaceous materials are difficult to be scaled up. For achieving high-performance K^+ storage, nanoscale engineering of carbonaceous materials is important to reduce the ion diffusion length. For example, carbon materials with unique nanostructures and pores allow the fast storage of K^+ within the pores and voids, contributing to much higher capacities and superior rate capabilities. Expanding the interlayer spacing in carbon materials can mitigate the diffusion barrier energy for K^+-ion intercalation, resulting in improved rate performance. Besides, heteroatom-doping is another typical strategy to improve the K^+ storage for carbon-based materials thanks to the abundant adsorption active sites and improved reaction kinetics. The combination of the above-mentioned strategies can further promote K^+ storage performance owing to the synergistic effects.

5 Alloys

Alloy-type anode materials are considered promising alternatives for carbon materials, and this kind of anode materials normally exhibit high theoretical capacities, energy density, and safety. However, the practical applications of these alloy-type anode

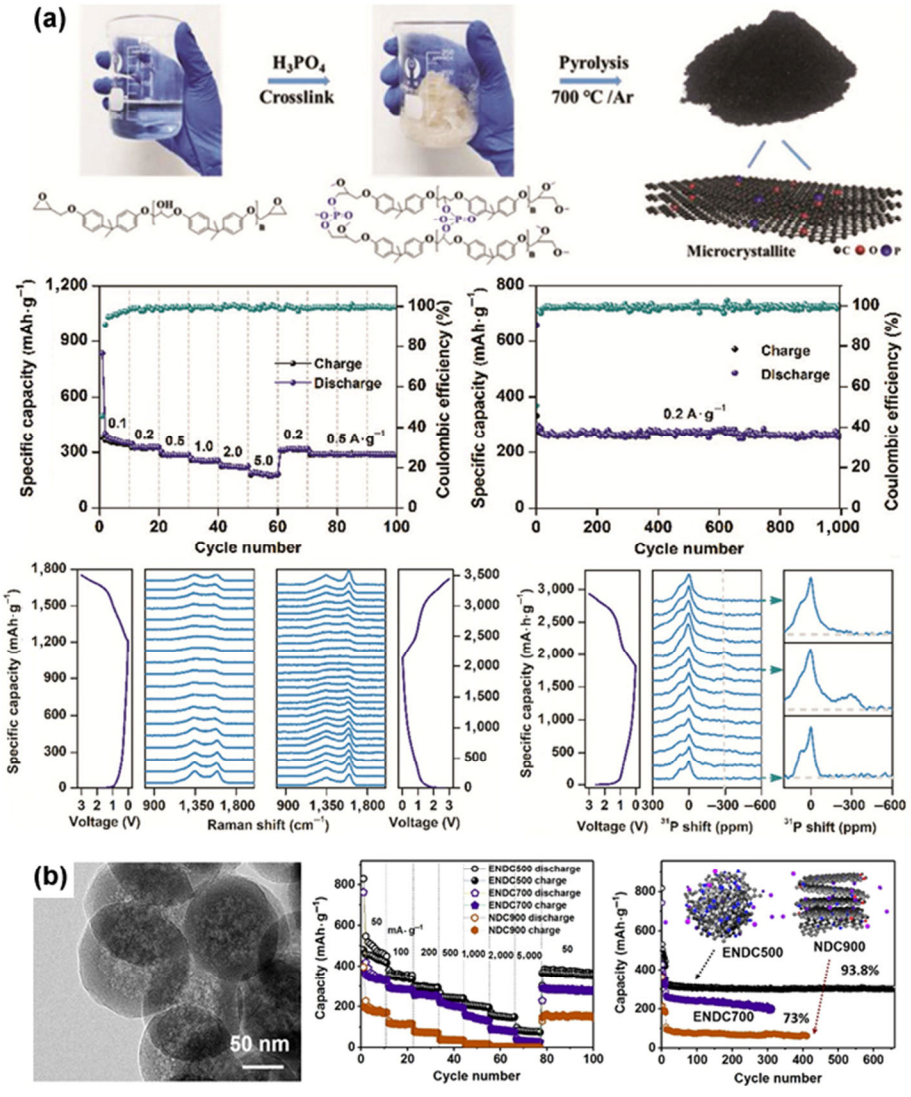

Figure 5 (a) Synthesis, K^+ storage performance, and *in situ* characterizations of phosphorus-doped hard carbon anode. Reprinted with permission from Ref. [77], © WILEY-VCH Verlag GmbH & Co. KGaA, Weinheim 2019. (b) SEM image of defect-rich, edge-N-doped carbons, and the electrochemical performance of PIBs. Reprinted with permission from Ref. [83], © WILEY-VCH Verlag GmbH & Co. KGaA, Weinheim 2020.

materials are seriously restricted by the poor cyclic stability and the large irreversible capacity loss originating from the huge volume change during continuous cycles. The main solutions to overcome these limitations are to improve the electrical contact in electrodes and retain the stability of SEI layers, which rely on the rational design and engineering of alloy-type anodic structures (Table 2), as will be introduced and discussed below.

5.1 Antimony (Sb)

Antimony (Sb) is the most extensively investigated element among metals for PIBs because of its high theoretical capacity (660 mAh·g^{-1}, K_3Sb) and low redox potentials (0.8 ~ 0.9 V vs. SHE) [102]. Unfortunately, Sb suffers from significant volume expansion (~ 390%) during electrochemical processes, leading to serious aggregation and pulverization of electrode materials, which deteriorates the electrochemical performances [103, 104]. To resolve the above challenges, the construction of nano-structured Sb/carbon or Sb/MXene composites has been widely recognized as an effective and straightforward strategy [105–110]. The nanostructured Sb can release the stress stemming from volume variations, while the carbon matrix/MXene sheets not only buffer the volume changes but also ensure the continuous electrical networks. So far, MOFs-derived [111], high-energy ball milling [112], thermal reduction [113–117], and dealloying methods [118] have been applied to produce Sb/carbon architectures. For instance, Lu and co-workers prepared Sb nanoparticles embedded in porous carbon (Sb-NPs@PC) composites through direct calcination of Sb-based MOFs (Fig. 6(a)) [111]. Due to the porous structures, large specific surface area, and uniform distributions of Sb nanoparticle, Sb-NPs@PC electrodes exhibited high reversible capacity reaching 551 mAh·g^{-1} at 50 mA·g^{-1}, great rate capability (270 mAh·g^{-1} at 1,000 mA·g^{-1}), and high capacity retention after 100 cycles. Wang et al. incorporated Sb nano-particles into the carbon sphere network (Sb@CSN) through the electrospray-assisted strategy followed by a thermal annealing process (Fig. 6(b)) [113]. Thanks to the conductive carbon network as well as the formation of a robust KF-rich SEI layer (with concentrated electrolyte solution) on the electrode, Sb@CSN anodes delivered impressive K storage performance (high capacity retention of 504 mAh·g^{-1} after 220 cycles at 200 mA·g^{-1}). To further optimize the anodic structure of PIBs, Feng et al. fabricated nanoporous Sb via an environmentally friendly vacuum-distillation method by using zinc as the alloy metal (Fig. 6(c)) [118]. The study showed that the morphology and porosity of nanoporous Sb could be finely tuned through adjusting the Zn-Sb compositions and

Table 2 Comparison of alloy-type materials for the anodes of PIBs

Anode	Morphology	Synthesis method	Specific capacity	Cyclic performance	Ref.
Sb particle@carbon composite	Porous structure	High-energy ball milling	400 mAh·g^{-1} at 50 mA·g^{-1}	—	[105]
Sb nanoparticle@porous carbon	Hierarchical porous structure	Precursor-derived method (MOFs)	160 mAh·g^{-1} at 2,000 mA·g^{-1}	497 mAh·g^{-1} after 100 cycles at 100 mA·g^{-1}	[111]
Sb@carbon composite	Macroporous structure	High-energy ball milling	286 mAh·g^{-1} at 1,000 mA·g^{-1}	97% capacity retention after 260 cycles	[112]
Sb@carbon composite	Nanoparticles in carbon spheres	Thermal reduction	—	504 mAh·g^{-1} after 220 cycles at 200 mA·g^{-1}	[113]
Sb@N, P-co-doped carbon composite	Uniform distributed porous structure	Thermal reduction	161 mAh·g^{-1} at 1,000 mA·g^{-1}	130 mAh·g^{-1} after 1500 cycles at 1,000 mA·g^{-1}	[114]
Sb nanoparticles@carbon composite	3D porous structure	Thermal reduction	387.2 mAh·g^{-1} at 2,000 mA·g^{-1}	280 mAh·g^{-1} after 500 cycles at 1,000 mA·g^{-1}	[115]
Sb nanorod@carbon tube	Hollow structure	Thermal reduction	211.5 mAh·g^{-1} at 5,000 mA·g^{-1}	300.1 mAh·g^{-1} after 120 cycles at 2,000 mA·g^{-1}	[116]
Sb nanoparticle@rGO	Hierarchical porous structure	Thermal reduction	381 mAh·g^{-1} at 100 mA·g^{-1}	210 mAh·g^{-1} after 200 cycles at 500 mA·g^{-1}	[117]
Sb/carbon	Porous structure	Dealloying method	30 mAh·g^{-1} at 500 mA·g^{-1}	318 mAh·g^{-1} after 50 cycles at 100 mA·g^{-1}	[118]
Sn nanoparticle/N-doped carbon	Hierarchical porous carbon	Sol–gel method followed by annealing	94 mAh·g^{-1} at 1,000 mA·g^{-1}	198 mAh·g^{-1} after 200 cycles at 50 mA·g^{-1}	[124]
Sn/carbon composite	Porous structure	Ball milling	150 mAh·g^{-1} at 25 mA·g^{-1}	—	[125]
Sn particle/rGO	3D porous structure	Solution method combined with annealing	67.1 mAh·g^{-1} at 2,000 mA·g^{-1}	200 mAh·g^{-1} after 50 cycles at 100 mA·g^{-1}	[126]
Bi@N-doped carbon sphere	Multicore–shell porous structure	The solvothermal method combined with annealing	152 mAh·g^{-1} at 100,000 mA·g^{-1}	203 mAh·g^{-1} after 1,000 cycles at 10,000 mA·g^{-1}	[128]
Bi nanoparticles/rGO	Hierarchical porous structure	Solution synthesis	235 mAh·g^{-1} at 500 mA·g^{-1}	290 mAh·g^{-1} after 150 cycles at 50 mA·g^{-1}	[129]
Bi nanospheres/graphene frameworks	3D porous frameworks	Self-assemble and annealing	180 mAh·g^{-1} at 50,000 mA·g^{-1}	185.2 mAh·g^{-1} after 2,000 cycles at 10,000 mA·g^{-1}	[130]
Bi network	3D porous structure	As received	—	86.5% of capacity retention after 350 cycles	[131]
Red P/carbon nanotube	Porous network	Ball milling	300 mAh·g^{-1} at 1,000 mA·g^{-1}	Stable for 680 cycles at 1,000 mA·g^{-1}	[134]
Black P/carbon	Bulk structure	Ball milling	617 mAh·g^{-1} at 50 mA·g^{-1}	61% capacity retention after 50 cycles	[135]
Red P/MoS_2	Porous layered structure	Ball milling	182 mAh·g^{-1} at 1,000 mA·g^{-1}	120.5 mAh·g^{-1} after 500 cycles at 1,000 mA·g^{-1}	[136]
P/carbon composite	Particle structure	Ball milling	223 mAh·g^{-1} at 200 mA·g^{-1}	323.5 mAh·g^{-1} after 50 cycles at 50 mA·g^{-1}	[137]
Red P/N-doped carbon nanofiber	Hollow tubular structure	vaporization-condensation-conversion approach	342 mAh·g^{-1} at 5,000 mA·g^{-1}	465 mAh·g^{-1} after 800 cycles at 2,000 mA·g^{-1}	[138]
Red P/carbon network	Porous hollow structure	vaporization-condensation-conversion approach	430 mAh·g^{-1} at 8,000 mA·g^{-1}	580 mAh·g^{-1} after 800 cycles at 2,500 mA·g^{-1}	[139]
Red P@carbon nanosheet	Interconnected porous structure	vaporization-condensation-conversion approach	323.7 mAh·g^{-1} at 2,000 mA·g^{-1}	—	[140]
P/activated carbon	Porous structure	vaporization-condensation-conversion approach	61 mAh·g^{-1} at 1,000 mA·g^{-1}	—	[141]
P particles/rGO	Hierarchical porous structure	vaporization-condensation-conversion approach	134.4 mAh·g^{-1} at 2,000 mA·g^{-1}	253 mAh·g^{-1} after 500 cycles at 500 mA·g^{-1}	[142]
Ge architecture	Porous structure	Chemical dealloying	—	120 mAh·g^{-1} after 400 cycles at 20 mA·g^{-1}	[143]
Pb architecture	Porous structure	Friction drawing	230 mAh·g^{-1} at 200 mA·g^{-1}	75% capacity retention after 350 cycles at 400 mA·g^{-1}	[144]
Zn nanoparticles /carbon network	Porous structure	Precursor-derived method (MOFs)	46 mAh·g^{-1} at 2,000 mA·g^{-1}	145 mAh·g^{-1} after 300 cycles at 500 mA·g^{-1}	[146]
BiSb alloy	Particle structure	*In situ* reduction method	300 mAh·g^{-1} at 1,000 mA·g^{-1}	353 mAh·g^{-1} after 1,000 cycles at 500 mA·g^{-1}	[149]
CoSn@carbon	Homogeneously distributed	Solution-based method	76.7 mAh·g^{-1} at 5,000 mA·g^{-1}	200 mAh·g^{-1} after 400 cycles at 200 mA·g^{-1}	[150]
Sb_xBi_{1-x} alloys/carbon framework	Porous structure	Sol–gel method	382 mAh·g^{-1} at 50 mA·g^{-1}	83% capacity retention after 400 cycles at 500 mA·g^{-1}	[151]

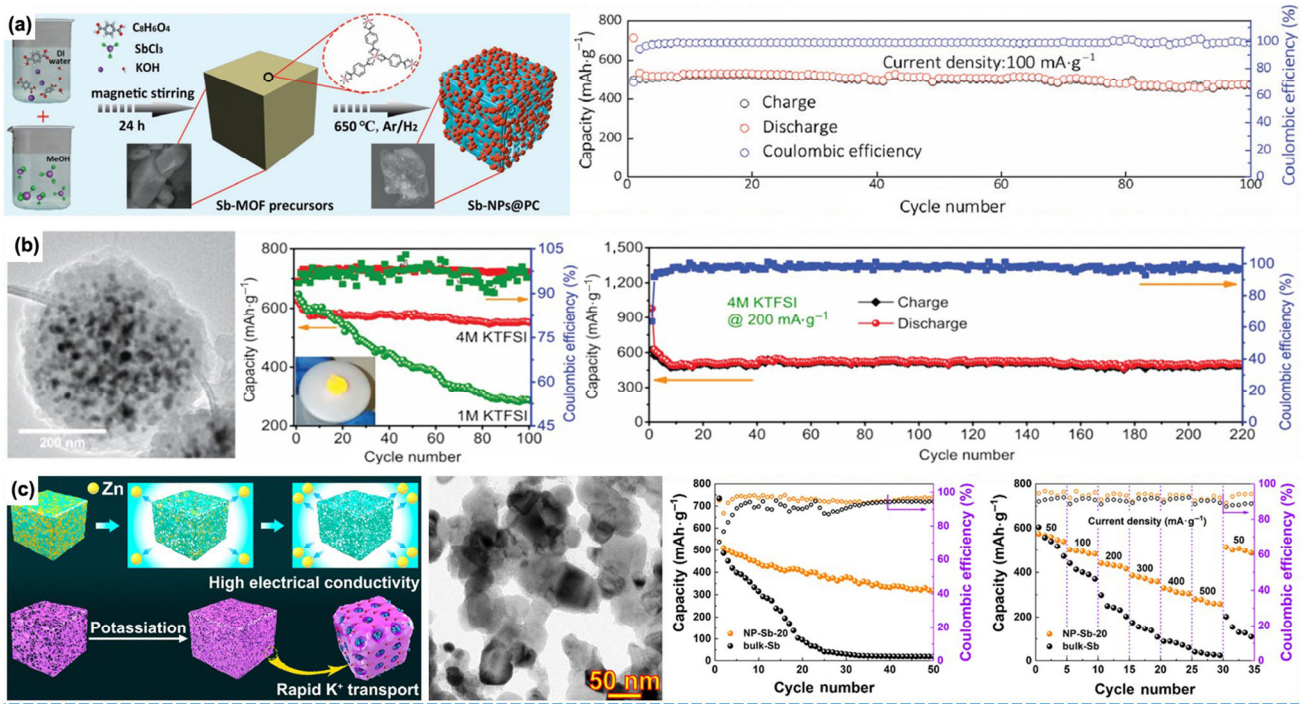

Figure 6 (a) Schematic illustration of the fabrication of Sb-NPs@PC material and cycle performance at 100 mA·g^{-1}. Reprinted with permission from Ref. [111], © The Royal Society of Chemistry 2019. (b) Morphology of Sb@CSN and K$^+$ storage performance of Sb@CSN electrode. Reprinted with permission from Ref. [113], © The Royal Society of Chemistry 2019. (c) Schematic illustration and transmission electron microscopy (TEM) image of nanoporous Sb, and the electrochemical performance of PIBs. Reprinted with permission from Ref. [118], © American Chemical Society 2018.

distillation temperature. Finally, the obtained nanoporous Sb architectures displayed enhanced electrochemical performances in terms of high specific capacity, good rate capability (265 mAh·g^{-1} at 500 mA·g^{-1}), and remarkable cyclic stability (318 mAh·g^{-1} after 50 cycles at 100 mA·g^{-1}). The above results suggest that Sb-based materials are highly promising for high-energy PIBs.

5.2 Tin (Sn)

Similar to Sb, Sn undergoes an alloying and dealloying reaction mechanism in ion batteries [119–121]. Although Sn possesses a high theoretical capacity, it commonly suffers from several apparent limits of low electrical conductivity and serious volume change. It has been demonstrated that the reaction of Sn with K undergoes two steps: forming a KSn intermediate phase after full potassiation and reversible nanopore generation during the cycle of Sn nanoparticles [122]. Unfortunately, Sn-based anodes commonly show a sharp drop in capacity after just a few cycles induced by the severe pulverization of Sn nanoparticles [123]. To surmount the above issue, great efforts have been devoted to the rational design and construction of Sn/carbon architectures [124–126]. Wang and co-workers reported an architecture composed of Sn nanoparticles anchored on a N-doped carbon matrix through a simple sol–gel method combined with a thermal treatment process (Fig. 7(a)) [124]. The N-doped carbon matrix possessed high electrical conductivity and remarkable structural integrity, endowing the total anode with good K storage performances (198 mAh·g^{-1} after 200 cycles at 50 mA·g^{-1}, and 94 mAh·g^{-1} at 1,000 mA·g^{-1}). As another representative work, Zhuang et al. fabricated Sn-based submicron-particles encapsulated in a porous rGO network through an *in situ* reduction method [126]. The Sn@rGO composites possessed the features of homogeneously distributed Sn-based particles in rGO networks, abundant structural defects, numerous oxygen-containing groups, and high specific surface area. All these features contributed to a significantly enhanced electrochemical K$^+$ storage performance.

5.3 Bismuth (Bi)

Recently, Bi has been widely used in ion batteries [127], because of its high theoretical capacity, large lattice fringes (3.95 Å), and environmental friendliness. The pioneering work from Yu and co-workers demonstrated the K storage performance of multicore–shell Bi@N-doped carbon nanospheres [128]. As shown in Fig. 7(b), the as-obtained structure possesses several advantages: (i) The completely encapsulated Bi nanospheres can alleviate the volume change and allow the SEI formation on the outer surface instead of the Bi surface; (ii) the voids and sizes of Bi nanoparticles significantly reduce the ion/electron diffusion length; (iii) the nitrogen doping can enhance the electrical conductivity of composite and provide more active sites for K$^+$ storage. Consequently, the as-prepared anodes exhibited outstanding rate capability of 152 mAh·g^{-1} at 100 A·g^{-1}, and long cycle life even for 2,000 cycles at 10 A·g^{-1} (235 mAh·g^{-1}). To further develop a feasible electrode that can well accommodate the large-sized K$^+$, Guo et al. reported Bi nanoparticles/rGO architecture via a simple room-temperature solution synthesis method [129]. Benefitting from the uniformly distributed Bi nanoparticles on the rGO surface and the high electrical conductivity for promoting fast electron transfer, Bi nanoparticles/rGO anodes displayed excellent electrochemical performance. Through further optimizing the compositions of electrolyte, the uniformity and stability of SEI layers can be improved, benefitting the electrochemical performance, especially the long-term cyclic stability. Bi nanospheres embedded into graphene frameworks [130] and 3D porous Bi network [131] were also reported and employed as the anodes of PIBs, and all of them exhibited good electrochemical performances.

5.4 Phosphorous (P)

The P as the anode material possesses the highest theoretical capacity (865 mAh·g^{-1}) among all the elements, and it is

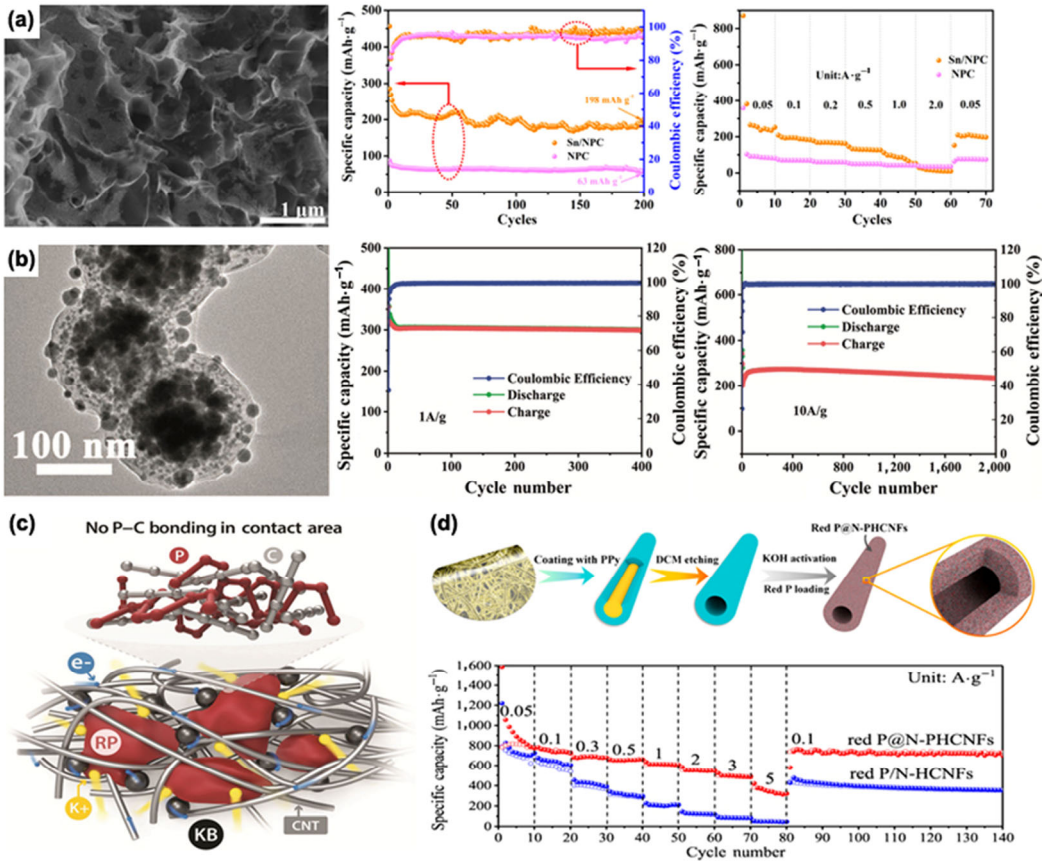

Figure 7 (a) SEM image of Sn/N-doped carbon and the K^+ storage performance. Reprinted with permission from Ref. [124], © Elsevier B.V. 2019. (b) TEM image of Bi@N-doped carbon and the electrochemical performance of PIBs. Reprinted with permission from Ref. [128], © WILEY-VCH Verlag GmbH & Co. KGaA, Weinheim 2019. (c) Schematic illustration of the structural configuration of activated Red P/C-based PIB electrode without the formation of P-C bonds. Reprinted with permission from Ref. [134], © WILEY-VCH Verlag GmbH & Co. KGaA, Weinheim 2019. (d) Red P in free-standing N-doped porous hollow carbon nanofibers and the K^+ storage performance. Reprinted with permission from Ref. [138], © American Chemical Society 2019.

abundant in the earth [132, 133]. In particular, due to the toxicity and chemical instability of white P, red P and black P are the primary species explored for PIBs. One efficient strategy to improve the K storage performance is to incorporate P species into substrates (e.g., carbonaceous materials, transition metal dichalcogenides (TMDs)) to form various intriguing architectures. As one of the most efficient and easily scaled-up production techniques, ball milling is used to prepare P-based composites, such as P/carbon composites [134–137]. For example, Tuan et al. have directly prepared the electrode slurry through ball milling the mixture composed of red P, multiwalled carbon nanotubes, Ketjen black, and sodium carboxymethyl cellulose (Fig. 7(c)) [134]. Red P particles were thoroughly encapsulated into the mixtures, and the presence of carbonaceous materials can enhance the electrical conductivity of electrodes. The as-prepared anodes exhibited a high reversible capacity reaching 750 $mAh·g^{-1}$ and high rate capability with the capacity of about 300 $mAh·g^{-1}$ at 1.0 $A·g^{-1}$. To further increase the loading of P in the electrodes and buffer the volume expansion during electrochemical redox reactions, the vaporization-condensation-conversion approach was developed [138–142]. This approach involves the selection/synthesis of carbonaceous materials with large voids and spaces, followed by the impregnation of P under heat treatment. Again, the encapsulation of red P into N-doped porous hollow carbon nanofibers matrix with ultrahigh pore volume and specific surface area was reported (Fig. 7(d)) [138]. In this work, the N-doped porous hollow carbon nanofibers were firstly prepared through the electrospinning method followed by using a self-scarified template method, red P was then introduced into the carbon matrix by the vaporization-condensation strategy. The anodes display great rate capability (342 $mAh·g^{-1}$ at 5.0 $A·g^{-1}$), and remarkable long cycle life with the reversible capacity as high as 465 $mAh·g^{-1}$ after 800 cycles at 2.0 $A·g^{-1}$. In addition, for the first time, Qu and co-workers designed and synthesized 1D carbon nanotube-backboned mesoporous carbon networks for confining P in PIBs [139]. The multiwalled carbon nanotubes were encapsulated into the foam like mesoporous carbon layers to form the special coaxial core–shell structures, and red P was embedded into the pores of the outer spaces of carbon shells. As a result, the final anodes exhibited a high reversible capacity (~ 1,000 $mAh·g^{-1}$ at 0.05 $A·g^{-1}$), superior rate performance with the capacity of ~ 430 $mAh·g^{-1}$ at 8.0 $A·g^{-1}$, and great cyclic stability over 800 cycles.

Other metals, like Ge [143], Pb [144, 145], and Zn [146], were also prepared to serve as the anode materials for PIBs. For instance, He et al. have prepared porous Ge anodes through a chemical-dealloying method [143]. By tailoring the nanoporous structures of Ge, the optimal electrochemical performances were obtained, including a stable capacity of about 120 $mAh·g^{-1}$ over 400 cycles. The formed intermediate K-Ge alloys can be detected upon discharging. Zhao et al. prepared the highly dispersed Zn nanoparticles confined into a nanoporous carbon network via annealing the Zn-containing MOFs under an inert atmosphere [146]. The as-prepared architecture possessed a porous structure and high surface area, which can boost the transport of electrons and ions as well as buffer the volume expansion during cycles.

5.5 Binary alloys

Metal alloys can also be utilized because of the high theoretical capacity value and accommodated volume changes [147, 148]. By optimizing the stoichiometry of different metallic elements, the electrochemical K^+ storage performance can be improved. Moreover, owing to the solid-state properties, the alloying processes can be limited to the local area and thus avoiding serious particle aggregations. As a representative work, Lu et al. prepared BiSb alloy through an *in situ* reduction method to serve as the anodes of PIBs [149]. Benefitting from the unique structures and special compositions, the as-obtained anodes displayed ultrahigh capacities reaching 611 and 300 mAh·g^{-1} at 100 and 1,000 mA·g^{-1}, respectively, as well as high cyclic stability of 353 mAh·g^{-1} after 1,000 cycles at 500 mA·g^{-1}. The above electrochemical performance comes from the series reactions between SbBi alloy and K^+ ions, which follows the conversion processes of SbBi to K(SbBi), then to K_3(SbBi) during discharge, and K_3(SbBi) to K(SbBi) and further to SbBi in the charge processes, as proved by the *in situ* characterizations. To further resolve the issues encountered by alloys and increase the electrochemical performance of PIBs, incorporating alloys into carbon matrices is the most promising strategy. For instance, Cabot and co-workers have confined the monodispersed CoSn and NiSn nanoparticles into a commercial carbon matrix for PIBs [150]. Owing to the nanosized particles and uniform distributions of alloys and the presence of carbon matrix, the as-achieved anodes showed excellent electrochemical performances with high discharge capacity values. Moreover, nanostructured Sb_xBi_{1-x} alloys anchored on 3D carbon frameworks were designed and fabricated via a modified sol–gel method [151]. When used as the anodes for PIBs, the optimal $Sb_{0.5}Bi_{0.5}$@carbon composite exhibited a high initial discharge capacity of 382 mAh·g^{-1} at 0.05 A·g^{-1} and long-term cyclic performance with the capacity retention as high as 83% after 400 cycles.

Although alloy-type anode materials suffered from poor cyclic stability and largely irreversible capacity loss, they are still regarded as promising candidates for practical applications after careful composition optimization and nanoscale structure engineering. P is the best choice as the anode materials of PIBs in this regard, owing to its high theoretical capacity and good cyclic stability derived from its intriguing intrinsic properties. Moreover, the most promising strategy to effectively accommodate the issues faced by alloy-type anode materials is to integrate with carbonaceous materials forming hybrid composites. Since some of the capacity contribution mechanisms of alloy-type materials are still vague, more efforts are still needed to focus on the in-depth working mechanisms during electrochemical reaction cycles. Regarding the large volume change of alloy-type anode materials, nanostructure engineering not only shortens ion diffusion pathways, but also alleviates the pulverization of active materials during electrochemical cycles. In addition, hybridizing nanostructured alloy-type materials with carbonaceous material can further improve the electrical conductivity and maximize the active material utilization, while suppressing the structural collapse. Up to now, different dimensional carbon materials have been integrated with alloy-based materials to achieve synergistic effects.

6 Transition metal compounds

6.1 Metal oxides

Metal oxides have been widely studied in LIBs and SIBs [152–154], however, their applications in PIBs are rarely reported. The reason can be attributed to the sluggish ion diffusion kinetics and poor structural stability [155, 156]. To resolve the above issues, 1D and 2D metal oxides with abundant active sites, large surface area, and short ion diffusion path have caught the attention of researchers. More importantly, 3D materials composed of 2D layered metal oxides possess the structural advantages of minimized volume expansion and self-aggregation, thus enabling high structural integrity. So far, well developed metal oxides with special structures that exhibit high K^+ storage performances in PIBs include Nb_2O_5 [157], TiP_2O_7 [158], TiO_x [159], VO_x [160, 161], SnO_x [162, 163], CuO [164], and so on. For instance, Nb_2O_5 with a layered structure, an open intrinsic framework, and good chemical stability was firstly reported in PIBs by Tang and co-workers [157]. As displayed in Fig. 8(a), the as-prepared Nb_2O_5 anodes delivered good rate capability (74 mAh·g^{-1} at 1.0 A·g^{-1}). Jiao et al. reported the synthesis of CuO and employed it as high-performance anode material (Fig. 8(b)) [164]. The CuO with nanoplate structure can ensure effective contact between the electrode and electrolyte and reduce the K^+ diffusion length. As a result, CuO anode displayed a high reversible capacity of 342.5 mAh·g^{-1} at 0.2 A·g^{-1} and good cyclic stability with the capacity of 206 mAh·g^{-1} after 100 cycles at 1.0 A·g^{-1}.

To further enhance the electrochemical performances of PIBs, metal oxides have been hybridized with carbonaceous materials. The introduction of carbonaceous materials can significantly enhance the electrical conductivity of anodes, which enables the fast transport of electrons and ions. Moreover, the as-formed large voids and spaces in the composites can well accommodate the volume expansion of active materials, as well as keep the structural integrity of total electrodes. As a typical work, Jiao et al. fabricated a flexible and self-standing electrode composed of V_2O_3 nanoparticles embedded into porous N-doped carbon nanofibers via electrospinning method followed by thermal treatment (Fig. 8(c)) [165]. *In situ* characterizations showed that the material interlayers and K^+ intercalation behavior are reversible, benefitting the structural integrity and electrochemical performance. Finally, a high reversible capacity of 240 mAh·g^{-1} at 50 mA·g^{-1}, great rate capability of 134 mAh·g^{-1} at 1,000 mA·g^{-1}, and long-term cycle stability reaching 500 cycles were obtained. In another work, Liu and co-workers have synthesized hollow MoO_2 wrapped by rGO sheets through a simple hydrothermal approach followed by thermal treatment [166]. The as-fabricated MoO_2/rGO composite anode could deliver a high K storage capacity of 367.2 mAh·g^{-1} at 50 mA·g^{-1}, and high capacity retention after 200 cycles. Other metal oxides, like $Na_2Ti_3O_7$ [167], TiO_x [168], Fe_3O_4 [169], SnO_2 [170, 171], MnO_2 [172], VO_x [173], etc., were also reported to hybrid with carbonaceous materials as new anodes for PIBs, and all these anodes showed improved electrochemical performance compared with the individual counterparts (Table 3).

6.2 Metal chalcogenides

6.2.1 *Metal sulfides*

Metal sulfides commonly have high electrical conductivity and large interlayer distances [174–177], and they can be directly used as the electrode materials of PIBs (Table 4). The most extensively investigated sulfide is molybdenum sulfides (MoS_2), a typical 2D TMD [178]. Theoretical simulations on MoS_2 have proven that the storage of K^+ derives from two steps: the intercalation of K^+ into the layered structure and the following conversion reaction [179]. The conversion reaction occurring at the low potential range would contribute to most of the K^+

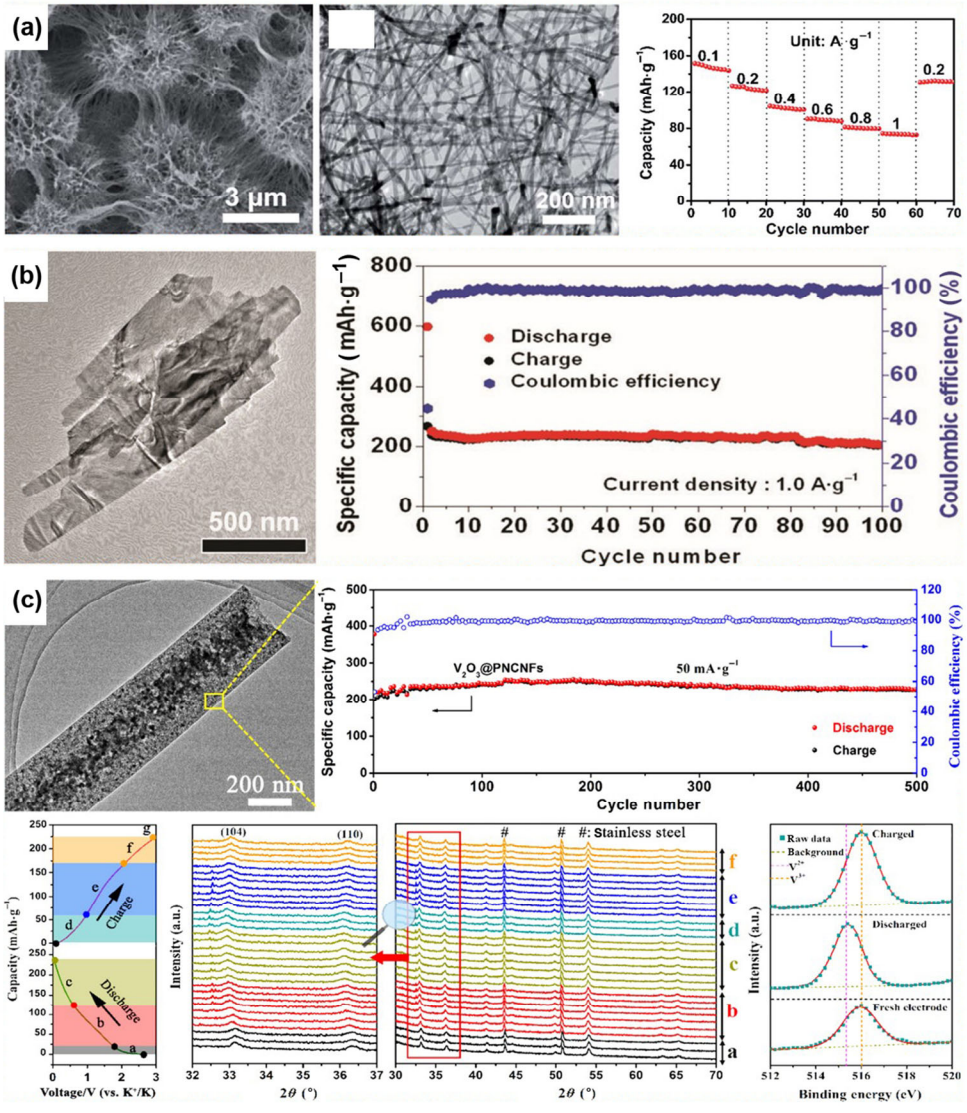

Figure 8 (a) Morphology and rate performance of T-Nb_2O_5 nanowires. Reprinted with permission from Ref. [157], © The Royal Society of Chemistry 2018. (b) TEM of CuO and the cycle stability at 1.0 A·g^{-1}. Reprinted with permission from Ref. [164], © WILEY-VCH Verlag GmbH & Co. KGaA, Weinheim 2019. (c) TEM image of V_2O_3 nanoparticles in a carbon nanofiber, cyclic performance at 50 mA·g^{-1}, and the *in situ* characterizations of anodes during charge/discharge processes. Reprinted with permission from Ref. [165], © Elsevier Ltd. 2018.

storage performance [180]. Even though MoS_2 can exhibit a high K^+ storage capacity, the layered structures of MoS_2 will tend to collapse upon deep discharge, thus restricting its applications. Similarly, carbonaceous materials are incorporated with MoS_2 through the construction of different architectures [181–188]. The carbonaceous materials can not only enhance the electrical conductivity of the composite but also serve as the substrates for MoS_2 layer decoration. The synergistic effects of the above two benefits can lead to significant improvement in K^+ storage capability. For instance, Qin et al. have reported bamboo-like MoS_2/N-doped carbon hollow tubes with an expanded interlayer distance of 10 Å [187]. The bamboo-like structure possessed the large spaces and voids to mitigate the strains in both directions and alleviate the volume expansion of K^+ intercalation (Fig. 9(a)), thereby efficiently hindering the continuous growth of SEI inside the particles. The bamboo-like structure can deliver a reversible capacity of 330 mAh·g^{-1} after 50 cycles at 50 mA·g^{-1}, 212 mAh·g^{-1} after 200 cycles at 100 mA·g^{-1}, and 151 mAh·g^{-1} after 1,000 cycles at 500 mA·g^{-1}. Moreover, to further promote the K^+ ion transportation in MoS_2/carbonaceous composites, Li and co-workers have fabricated a hierarchical interlayer-expanded MoS_2 assembled on carbon tubes through a straightforward solution method (Fig. 9(b)) [188]. The MoS_2 layers demonstrated increased interlayer spacing, which decreases the diffusion energy barrier and boosts the ion diffusion kinetics. As a result, the MoS_2 anode displayed a great rate capability with the capacity value of 247 mAh·g^{-1} at 1.0 A·g^{-1}, and 176 mAh·g^{-1} after 500 cycles at 1.0 A·g^{-1}

Other materials were also synthesized and used to incorporate the MoS_2 layers, such as metal oxides [189–191], and sulfides [192]. These composite materials exhibited impressive electrochemical performances when serving as the anodes for PIBs. Liu and co-workers have synthesized MoS_2-based heterostructured materials composed of a conductive Fe_9S_{10} core and carbon layers (Fig. 9(c)) [192]. The Fe_9S_{10} core here can improve the electrical conductivity, facilitate the densifying of MoS_2 particles, and form numerous heterogeneous interfaces. A high volumetric capacity of 408 mAh·cm^{-3}, and stable cyclic performance (50 cycles at 2.0 A·g^{-1}) were finally achieved.

Tin sulfides (SnS_2), another typical sulfide with a high theoretical capacity (733 mAh·g^{-1}) combining both the conversion and alloying mechanisms, have also been investigated [193]. Although theoretical calculations have confirmed that SnS_2 can display increased electrical conductivity when combined

Table 3 Comparisons of metal oxides as the anodes of PIBs

Anode	Morphology	Synthesis method	Specific capacity	Cyclic performance	Refs.
Nb_2O_5	Porous open structure	Hydrothermal method	104 mAh·g^{-1} at 400 mA·g^{-1}	0.068% per cycle decay for 400 cycles	[157]
TiP_2O_7	Spherical structure	Precursor-derived method	138.9 mAh·g^{-1} at 5,000 mA·g^{-1}	177.2 mAh·g^{-1} after 5,300 cycles at 1,000 mA·g^{-1}	[158]
Ti_6O_{11}	Particle structure	Reduction method	150 mAh·g^{-1} at 50 mA·g^{-1}	Stable for 500 cycles at 200 mA·g^{-1}	[159]
Sn-doped V_2O_5	Hierarchical tremella-like structure	Solvothermal method combined with partially replacing process	166 mAh·g^{-1} at 500 mA·g^{-1}	188 mAh·g^{-1} after 3,000 cycles at 500 mA·g^{-1}	[160]
Amorphous V_2O_5	Layered structure	Electrodeposited method	—	—	[161]
SnO	Hierarchical porous structure	Precipitation method	—	80% capacity retention after 30 cycles	[162]
SnO_2/Stainless steel mesh	Hierarchical porous structure	Hydrothermal method	125 mAh·g^{-1} at 1,000 mA·g^{-1}	128 mAh·g^{-1} after 200 cycles at 1,000 mA·g^{-1}	[163]
CuO	Nanoplate-like structure	Hydrothermal method	342.5 mAh·g^{-1} at 200 mA·g^{-1}	206 mAh·g^{-1} after 100 cycles at 1,000 mA·g^{-1}	[164]
V_2O_3 nanoparticles/N-doped carbon nanofibers	Self-standing porous structure	Electrospinning followed with thermal treatment	134 mAh·g^{-1} at 1,000 mA·g^{-1}	95.8% capacity retention after 500 cycles at 50 mA·g^{-1}	[165]
MoO_2/rGO	Porous hollow structure	Hydrothermal method followed by thermal treatment	367.2 mAh·g^{-1} at 50 mA·g^{-1}	104.2 mAh·g^{-1} after 500 cycles at 500 mA·g^{-1}	[166]
$Na_2Ti_3O_7$/N-doped carbon sponge	Porous wire structure	Hydrothermal method followed by thermal treatment	25 mAh·g^{-1} at 1,000 mA·g^{-1}	107.8 mAh·g^{-1} after 20 cycles at 100 mA·g^{-1}	[167]
TiO_2/carbon	Hierarchical tubular structure	Wet-chemical method	97.3 mAh·g^{-1} at 2,000 mA·g^{-1}	132.8 mAh·g^{-1} after 1,200 cycles at 500 mA·g^{-1}	[168]
Fe_3O_4/N-doped graphene	3D porous frameworks	Chemical blowing method	97.2 mAh·g^{-1} at 2,000 mA·g^{-1}	154.6 mAh·g^{-1} after 500 cycles at 1,000 mA·g^{-1}	[169]
SnO_2/carbon	3D porous structure	Freeze-drying followed by dealloying	144.6 mAh·g^{-1} at 2,000 mA·g^{-1}	270.3 mAh·g^{-1} after 200 cycles at 100 mA·g^{-1}	[170]
SnO_2/graphene-carbon	Homogeneous distributed in carbon nanofiber	Electrospinning method	114.8 mAh·g^{-1} at 1,000 mA·g^{-1}	202.1 mAh·g^{-1} after 100 cycles at 100 mA·g^{-1}	[171]
MnO_2/carbon nanotube	Nanowire arrays	Hydrothermal method	241 mAh·g^{-1} at 100 mA·g^{-1}	—	[172]
V_2O_3/graphene	Porous structure	Hydrothermal method	104 mAh·g^{-1} at 1,000 mA·g^{-1}	Stable for 2,000 cycles at 1,000 mA·g^{-1}	[173]

Table 4 Comparison of metal sulfides/selenides as the anodes of PIBs

Anode	Morphology	Synthesis method	Specific capacity	Cyclic performance	Refs.
Carbon-coated MoS_2/N-doped graphene	Layer stacked structure	Hydrothermal method	176.6 mAh·g^{-1} at 2,000 mA·g^{-1}	220.7 mAh·g^{-1} after 150 cycles at 1,000 mA·g^{-1}	[181]
MoS_2/carbon polyhedron	Porous structure	Precursor-derived method	291.9 mAh·g^{-1} at 5,000 mA·g^{-1}	350.4 mAh·g^{-1} after 500 cycles at 500 mA·g^{-1}	[182]
MoS_2 monolayer/carbon	Porous layered structure	Solvothermal method	323 mAh·g^{-1} at 100 mA·g^{-1}	180 mAh·g^{-1} after 240 cycles at 500 mA·g^{-1}	[183]
MoS_2/carbon nanotube	Porous layered structure	Solvothermal method followed by thermal annealing	310 mAh·g^{-1} at 1,000 mA·g^{-1}	510 mAh·g^{-1} after 100 cycles at 200 mA·g^{-1}	[184]
MoS_2/rGO	Porous rose-like structure	Hydrothermal method	438.5 mAh·g^{-1} at 100 mA·g^{-1}	98.5% capacity retention after 200 cycles at 100 mA·g^{-1}	[185]
MoS_2 rose/rGO	Porous rose-like structure	Solvothermal method	178 mAh·g^{-1} at 500 mA·g^{-1}	381 mAh·g^{-1} after 100 cycles at 100 mA·g^{-1}	[186]
MoS_2/N-doped carbon	Bamboo-like tubular structure	Solvothermal method followed by thermal annealing	131 mAh·g^{-1} at 2,000 mA·g^{-1}	151 mAh·g^{-1} after 1,000 cycles at 500 mA·g^{-1}	[187]
MoS_2/N, O-codoped carbon	Porous tubular structure	Solvothermal method followed by thermal annealing	247 mAh·g^{-1} at 1,000 mA·g^{-1}	220 mAh·g^{-1} after 300 cycles at 250 mA·g^{-1}	[188]
Carbon-coated MoS_2/$TiNb_2O_6$ spheres	Porous layered structure	Solvothermal method followed by thermal annealing	233 mAh·g^{-1} at 1,000 mA·g^{-1}	175 mAh·g^{-1} after 300 cycles at 1,000 mA·g^{-1}	[189]
MoS_2/MoO_2-carbon	Porous structure	Chemical vapor deposition combined with hydrothermal method	296 mAh·g^{-1} at 500 mA·g^{-1}	91% capacity retention after 500 cycles at 500 mA·g^{-1}	[190]
MoS_2@SnO_2@carbon	Hierarchical porous structure	Hydrothermal method	86 mAh·g^{-1} at 800 mA·g^{-1}	312 mAh·g^{-1} after 25 cycles at 50 mA·g^{-1}	[191]
MoS_2@Fe_9S_{10}@carbon	Hierarchical layered structure	Molten-salt method followed by chemical vapor deposition	127 mAh·g^{-1} at 5,000 mA·g^{-1}	95.4% capacity retention after 50 cycles at 2,000 mA·g^{-1}	[192]

(Continued)

Anode	Morphology	Synthesis method	Specific capacity	Cyclic performance	Refs.
SnS_2/rGO	Porous layered structure	H_2S reduction method	120 mAh·g^{-1} at 2,000 mA·g^{-1}	—	[193]
Few layer SnS_2/rGO	Porous layered structure	Solvothermal method	247 mAh·g^{-1} at 1,000 mA·g^{-1}	205 mAh·g^{-1} after 300 cycles at 1,000 mA·g^{-1}	[195]
SnS_2/carbon/rGO	Porous layered structure	Solution-based method	397.4 mAh·g^{-1} at 2,000 mA·g^{-1}	298.1 mAh·g^{-1} after 500 cycles at 500 mA·g^{-1}	[196]
CoS/carbon nanotube/carbon frameworks	Porous structure	Precursor-derived method	133.1 mAh·g^{-1} at 6,400 mA·g^{-1}	130 mAh·g^{-1} after 600 cycles at 3,200 mA·g^{-1}	[197]
CoS/graphene	Porous layered structure	Hydrothermal method	232.3 mAh·g^{-1} at 4 C	310.8 mAh·g^{-1} after 100 cycles at 500 mA·g^{-1}	[198]
CoS/N-doped carbon	Particle structure	Hydrothermal method	186 mAh·g^{-1} at 1,000 mA·g^{-1}	303 mAh·g^{-1} after 150 cycles at 200 mA·g^{-1}	[199]
FeS_2@carbon	Porous yolk-shell structure	Solution-based method	203 mAh·g^{-1} at 10,000 mA·g^{-1}	Stable for 1,500 cycle at 5,000 mA·g^{-1}	[200]
FeS_2 nanocage@rGO	Porous hollow structure	Precursor-derived method	151 mAh·g^{-1} at 500 mA·g^{-1}	123 mAh·g^{-1} after 420 cycles at 500 mA·g^{-1}	[201]
Graphene/FeS_2/carbon	Porous structure	Solution-based method combined with thermal annealing process	298 mAh·g^{-1} at 2,000 mA·g^{-1}	—	[202]
FeS_2@carbon nanoparticles	Porous hollow structure	Solution-based method combined with thermal annealing process	486 mAh·g^{-1} at 2,000 mA·g^{-1}	Stable for 100 cycles at 500 mA·g^{-1}	[203]
2H-WS_2	Layered structure	As received	40 mAh·g^{-1} at 200 mA·g^{-1}	—	[204]
WS_2 powder	Layered structure	As received	58 mAh·g^{-1} at 800 mA·g^{-1}	103 mAh·g^{-1} after 100 cycles at 100 mA·g^{-1}	[205]
Sb_2S_3/carbon sheet	Porous structure	High-shear exfoliation method	~ 180 mAh·g^{-1} at 2,000 mAh·g^{-1}	404 mAh·g^{-1} after 200 cycles at 50 mA·g^{-1}	[206]
Sb_2S_3/S, N-doped graphene	Porous structure	Hydrothermal method	—	Stable for 50 cycles	[207]
CuS nanosheet/GO	Porous structure	One-step method	410 mAh·g^{-1} at 1 00 mA·g^{-1}	290.5 mAh·g^{-1} after 100 cycles at 100 mA·g^{-1}	[208]
$NiCo_{2.5}S_4$/rGO	Porous layered structure	Solution-based method	402 mAh·g^{-1} at 2,000 mA·g^{-1}	495 mAh·g^{-1} after 1,900 cycles at 200 mA·g^{-1}	[209]
$MoSe_2$/carbon nanostructure	Pistachio-shuck-like structure	Thermal annealing	224 mAh·g^{-1} at 200 mA·g^{-1}	226 mAh·g^{-1} after 1000 cycles at 1,000 mA·g^{-1}	[210]
$FeMoSe_4$/N-doped carbon	Flower-like porous structure	Colloid method combined with thermal annealing	227 mAh·g^{-1} at 1,000 mA·g^{-1}	178 mAh·g^{-1} after 400 cycles at 1,000 mA·g^{-1}	[211]
$MoSe_2$/N, S-doped carbon	Porous layered structure	Solution-based method combined with thermal annealing	239 mAh·g^{-1} at 2,000 mA·g^{-1}	192 mAh·g^{-1} after 1,000 cycles at 5,000 mA·g^{-1}	[212]
$MoSe_2$/carbon fiber	Fiber structure	Electrospinning method	133 mAh·g^{-1} at 3,000 mA·g^{-1}	81 mAh·g^{-1} after 100 cycles at 100 mA·g^{-1}	[213]
Carbon-coated $MoSe_2$/MXene	Porous structure	Hydrothermal combined with thermal annealing	183 mAh·g^{-1} at 10,000 mA·g^{-1}	355 mAh·g^{-1} after 100 cycles at 200 mA·g^{-1}	[214]
Commercial $TiSe_2$	Powder structure	As received	38.3 mAh·g^{-1} at 16 C	52.2 mAh·g^{-1} after 300 cycles at 2 C	[218]
$ReSe_2$/rGO	Porous spherical structure	Hydrothermal combined with thermal annealing	203 mAh·g^{-1} at 10,000 mA·g^{-1}	150 mAh·g^{-1} after 500 cycles at 2,000 mA·g^{-1}	[219]
$CoSe_2$/N-doped carbon nanotube	Nanoparticles on tubular structure	Solvothermal method	196 mAh·g^{-1} at 2,000 mA·g^{-1}	173 mAh·g^{-1} after 600 cycles at 2,000 mA·g^{-1}	[220]
$Co_{0.85}Se$/carbon nanobox	Porous hollow structure	MOFs electrospinning method	166 mAh·g^{-1} at 5,000 mA·g^{-1}	299 mAh·g^{-1} after 400 cycles at 1,000 mA·g^{-1}	[221]
$Co_{0.85}Se$/carbon polyhedron	Porous hollow structure	Solution-based combined with thermal annealing	220 mAh·g^{-1} at 2,000 mA·g^{-1}	402 mAh·g^{-1} after 100 cycles at 50 mA·g^{-1}	[222]
ZnSe/carbon nanocage	Porous hollow spheres	Solution-based template method	318 mAh·g^{-1} at 50 mA·g^{-1}	189 mAh·g^{-1} after 1,000 cycles at 500 mA·g^{-1}	[223]
ZnSe/N-doped carbon	Porous polyhedron	Solution-based combined with thermal annealing	52.8 mAh·g^{-1} at 5,000 mA·g^{-1}	262.8 mAh·g^{-1} after 200 cycles at 100 mA·g^{-1}	[224]
VSe_2 nanosheets	Graphene-like structure	Solution-based method	169 mAh·g^{-1} at 2,000 mA·g^{-1}	0.025% decay per cycle for 500 cycles	[225]
Ta_4NiSe_5	Layered structure	Ion-intercalation and exfoliation method	121 mAh·g^{-1} at 1,000 mA·g^{-1}	81.4% capacity retention after 1,100 cycles at 500 mA·g^{-1}	[226]
$NbSe_2$ flakes	Layered structure	Physical exfoliation method	95 mAh·g^{-1} at 25 mA·g^{-1}	—	[227]

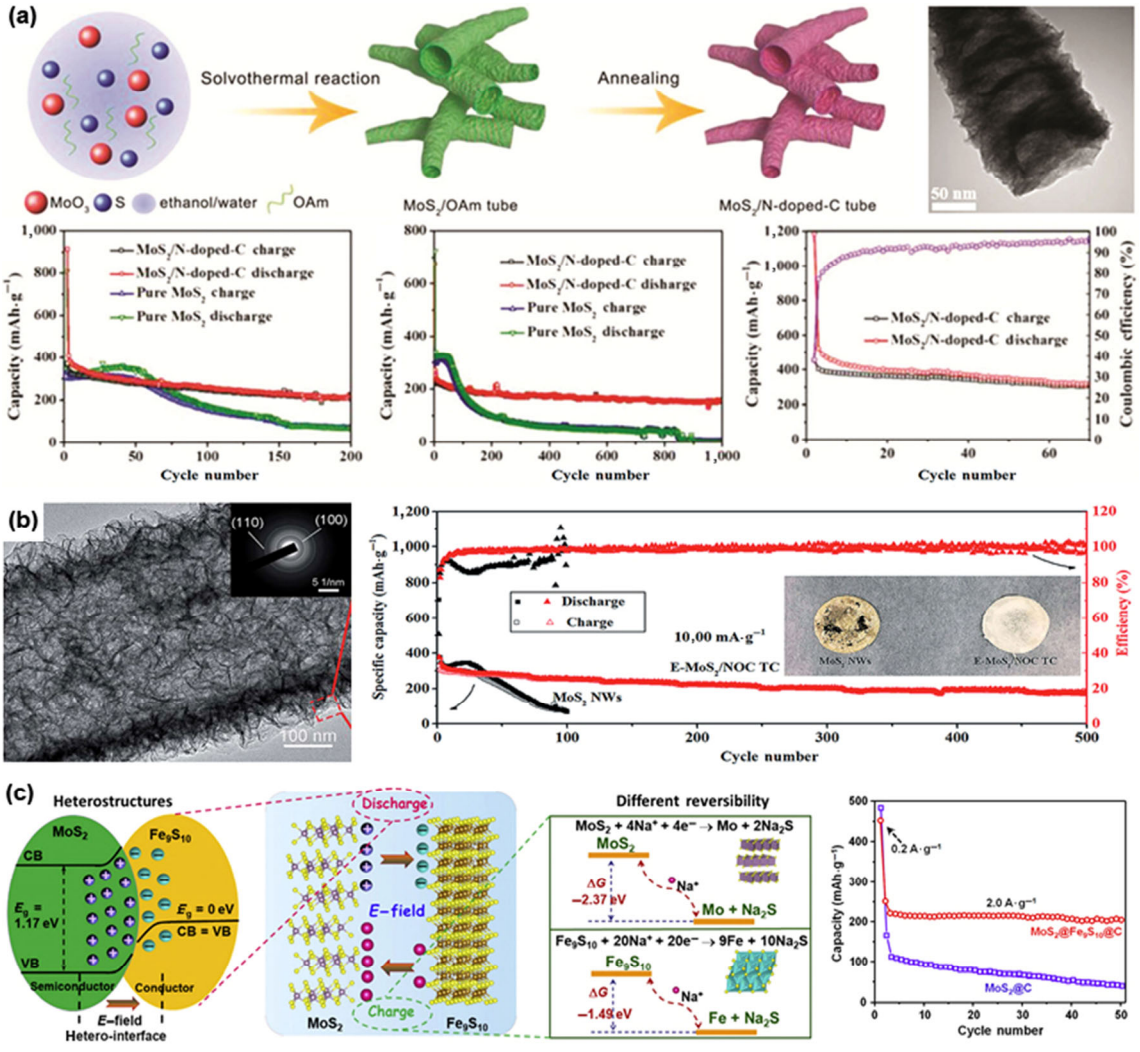

Figure 9 (a) Synthesis, morphology, and electrochemical performance of MoS_2/N-doped-carbon tube. Reprinted with permission from Ref. [187], © WILEY-VCH Verlag GmbH & Co. KGaA, Weinheim 2018. (b) TEM of tubular, interlayer expanded MoS_2-N/O-doped carbon and the cycle stability at 1.0 $A{\cdot}g^{-1}$. Reprinted with permission from Ref. [188], © The Royal Society of Chemistry 2019. (c) Schematic illustration of the formation mechanism and direction of internal E-field for Fe_9S_{10}@MoS_2@carbon during discharge and charge processes and the cycle performance at 2.0 $A{\cdot}g^{-1}$. Reprinted with permission from Ref. [192], © Elsevier B.V. 2019.

with K^+ ions during electrochemical reactions, the sluggish K^+ diffusion kinetic seriously restricts their practical applications [194]. To meet the challenge of severe volume expansion and low electrical conductivity, rational structure engineering and composite electrode design have been adopted. For instance, Xia and co-workers have incorporated SnS_2 nanosheets with rGO to form the composite electrodes of PIBs (Fig. 10(a)) [195]. Thanks to the ultrathin nanosheets and excellent structural integrity, the hybrid enabled fast K^+ storage kinetics and fast electron/ion transportation. As a result, the hybrid delivered high specific capacity reaching 448 $mAh{\cdot}g^{-1}$ at 0.05 $A{\cdot}g^{-1}$, great rate capability with the capacity of 247 $mAh{\cdot}g^{-1}$ at 1.0 $A{\cdot}g^{-1}$, and impressive cyclic stability with 87% capacity retention after 100 cycles. Moreover, Ci et al. have restrained SnS_2 into the porous carbon networks with rGO shells as the anodes for PIBs, via a pyrolysis and combination method (Fig. 10(b)) [196]. The rGO coating can efficiently restrict SnS_2 in porous carbon networks, and result in enhanced electrochemical performance.

Besides the abovementioned sulfides, other sulfides, like CoS [197–199], FeS_2 [200–203], WS_2 [204, 205], Sb_2S_3 [206, 207], CuS [208], and $NiCo_{2.5}S_4$ [209], were also prepared and utilized as the anodes. Guan et al. have reported the engineering of FeS_2@carbon structure on the graphene matrix through a solution-processed method (Fig. 10(c)) [202]. The channels and space between yolk and shell can alleviate the volume expansion and prevent the aggregation of FeS_2 species. The graphene matrix can enhance the charge transport within the composite. The hybrid displayed a high reversible capacity and great rate capability with the capacity reaching 298 $mAh{\cdot}g^{-1}$ at 2.0 $A{\cdot}g^{-1}$. Liu and co-workers have reported the fabrication of layered Sb_2S_3 via a solution-triggered one-step shear exfoliation method [206]. The as-prepared composite anodes can also show excellent electrochemical performance, which can be attributed to the structural advantages, including layered morphology which can minimize the volume expansion and shorten the ion transport distance during electrochemical processes, and the existence of carbon sheets to enhance the electrical conductivity and maintain the total structural integrity.

6.2.2 *Metal selenides*

Compared to metal sulfides, metal selenides have a higher electrical conductivity, which makes them promising for high-power electrode materials (Table 4) [210]. Meanwhile, metal selenides also suffer from severe volume expansion during

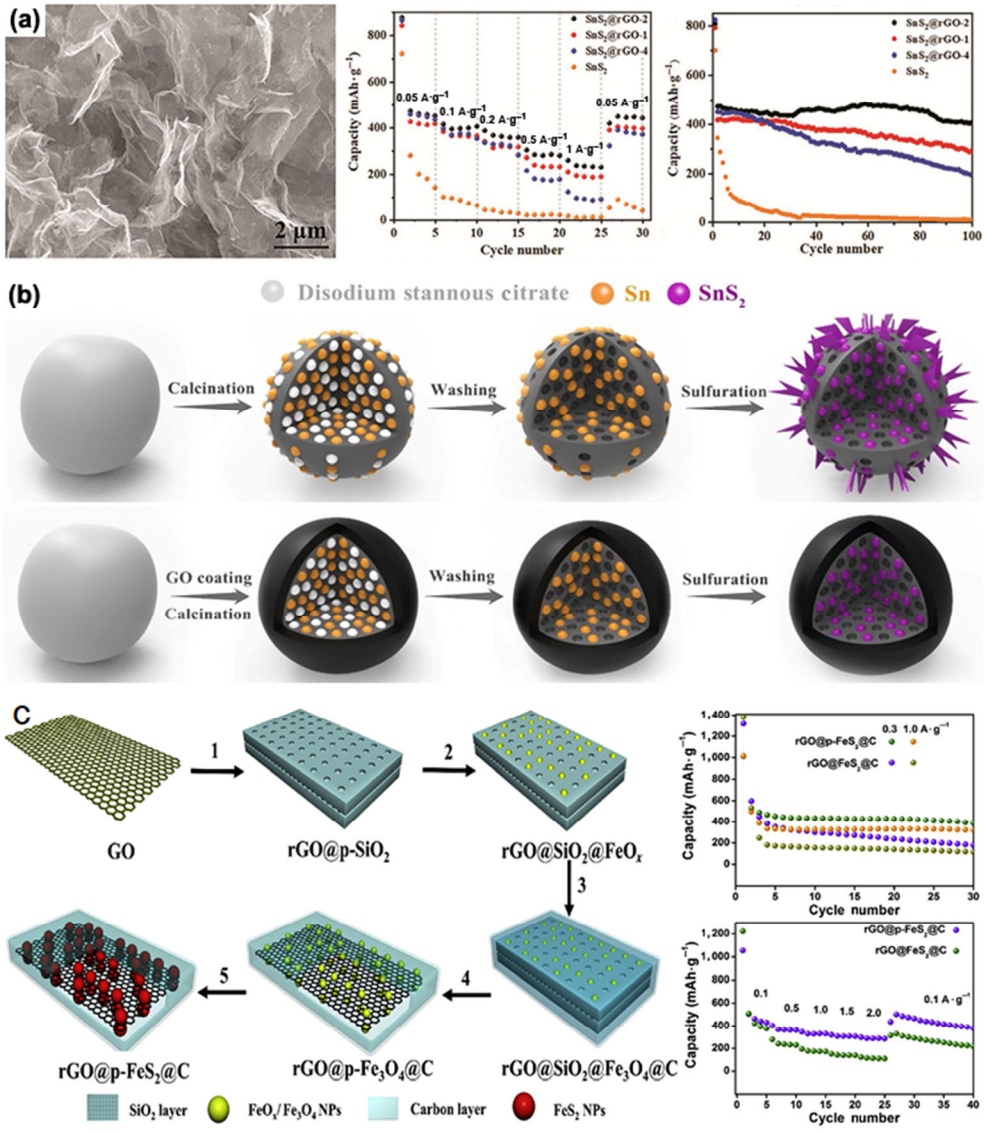

Figure 10 (a) SEM image of SnS_2@rGO-2 and electrochemical performance of PIBs. Reprinted with permission from Ref. [195], © WILEY-VCH Verlag GmbH & Co. KGaA, Weinheim 2019. (b) Synthesis process of SnS_2@C and SnS_2@C@rGO-*x*. Reprinted with permission from Ref. [196], © WILEY-VCH Verlag GmbH & Co. KGaA, Weinheim 2019. (c) Schematic illustration of rGO@p-FeS_2@C and the K^+ storage performance. Reprinted with permission from Ref. [202], © Elsevier Ltd. 2019.

charge/discharge processes. As a typical metal selenide, molybdenum selenides ($MoSe_2$) with versatile nanostructures were carefully designed and incorporated with carbon matrix to form composite anodes for PIBs [210–213]. Guo et al. constructed a pistachio-shuck-like $MoSe_2$/carbon nanostructure for boosting the performance of PIBs (Fig. 11(a)) [210]. The few-layer $MoSe_2$ with expanded interlayer distance enables fast intercalation/deintercalation of K^+ ions, while the carbon shell restrains the $MoSe_2$ and improves the structural integrity of the electrode during cycles. As a result, the as-prepared anodes showed a high capacity reaching 322 mAh·g^{-1} at 0.2 A·g^{-1} for 100 cycles, and maintained 226 mAh·g^{-1} at 1.0 A·g^{-1} even after 1,000 cycles. Coupling $MoSe_2$ with MXene can enhance the K^+ storage performance of $MoSe_2$. In this regard, Zhang and co-workers have fabricated hierarchical carbon-coated $MoSe_2$/MXene hybrid nanosheets via a hydrothermal method followed by thermal annealing processes (Fig. 11(b)) [214]. The $MoSe_2$/MXene anodes displayed excellent electrochemical performance with a high specific capacity of 207 mAh·g^{-1} at 5.0 A·g^{-1} after 300 cycles and an impressive rate capability of 183 mAh·g^{-1} at 10 A·g^{-1}.

Other selenides, like GeSe [215–217], $TiSe_2$ [218], $ReSe_2$ [219], $CoSe_x$ [220–222], ZnSe [223, 224], VSe_2 [225], Ta_4NiSe_5 [226], and $NbSe_2$ [227], were also prepared and employed as the anodes of PIBs, and all these PIBs show excellent electrochemical performance for K^+ storage. For instance, Ma et al. have reported the fabrication of $ReSe_2$ nanosheets anchored on rGO nanoflakes (Fig. 11(c)) [219]. The layered structure of $ReSe_2$ can facilitate the interaction of K^+ and shorten the ion diffusion path, while rGO sheets offer the conductive matrix to buffer the volume changes during cycles. In PIBs, a high specific capacity of over 250 mAh·g^{-1} was achieved after 200 cycles even at 500 mA·g^{-1}. When the current rate was increased to 10 A·g^{-1}, the capacity can retain at 203 mAh·g^{-1}. Moreover, Wang and co-workers have designed and fabricated the few-layered ternary selenides for PIBs [226], Ta_2NiSe_5, which has large interlayer spacing and abundant Se sites. Experiments and theoretical simulations confirmed that the intercalation of K^+ prefered to happen along the zigzag pathways in layered Ta_2NiSe_5. Finally, a high capacity of 315 mAh·g^{-1}, an impressive rate capability of 121 mAh·g^{-1} at 1.0 A·g^{-1}, and ultra-stable cyclic performance were obtained. These pioneering investigations demonstrated that the utilization of selenides may provide an opportunity for realizing the practical applications of PIBs.

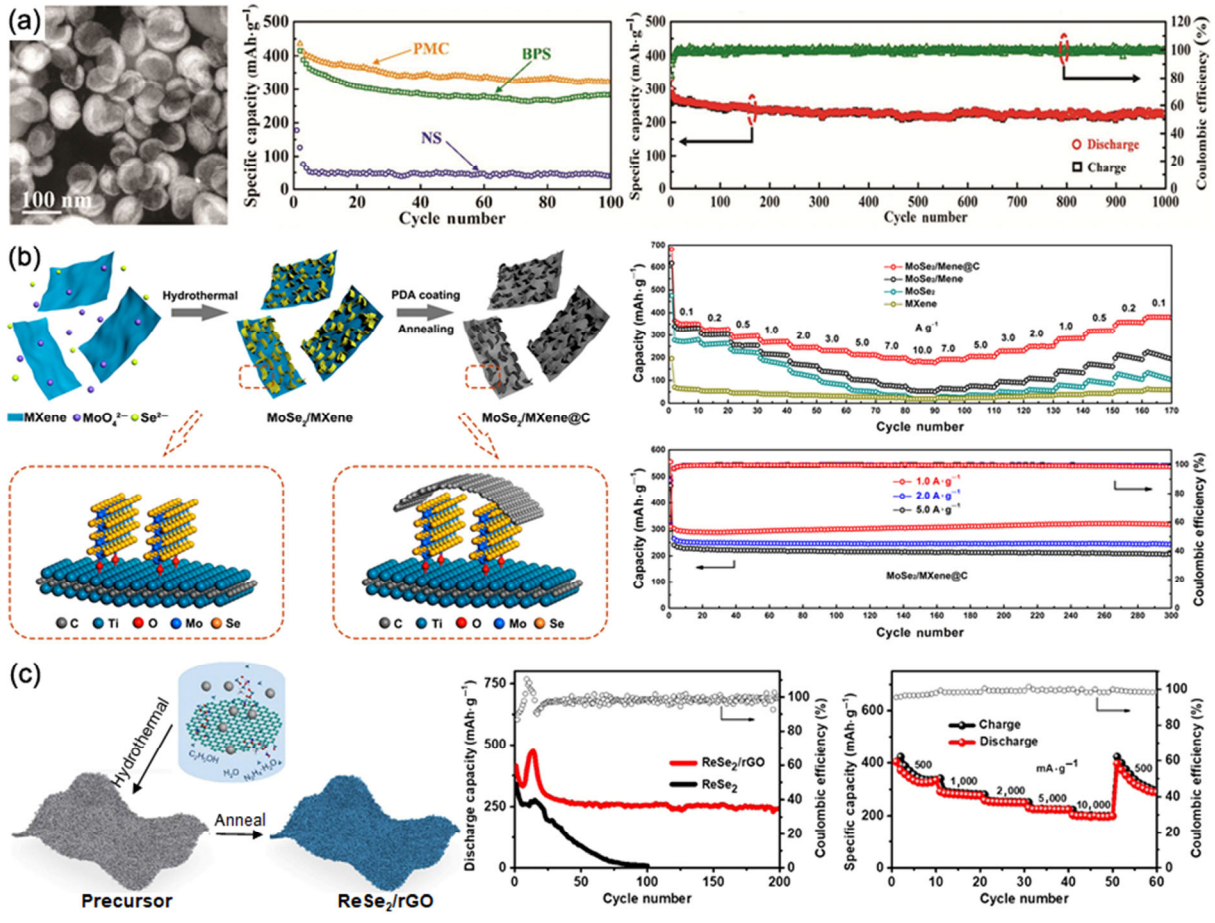

Figure 11 (a) SEM image of pistachio-shuck-like $MoSe_2$/carbon core/shell nanostructure and electrochemical performance of PIBs. Reprinted with permission from Ref. [210], © WILEY-VCH Verlag GmbH & Co. KGaA, Weinheim 2018. (b) Schematic of the preparation of $MoSe_2$/MXene@carbon, the rate, and long-term cycle stability. Reprinted with permission from Ref. [214], © American Chemical Society 2019. (c) Schematic illustration of $ReSe_2$@rGO composites and the K^+ storage performance. Reprinted with permission from Ref. [219], © WILEY-VCH Verlag GmbH & Co. KGaA, Weinheim 2019.

6.3 Metal phosphides

Phosphides are promising anode materials for PIBs, but the synthesis of phosphides usually involves complicated processes and harsh experimental conditions [228, 229]. The state-of-art metal phosphide electrodes for PIBs are summarized in Table 5. Tin phosphides are the most extensively investigated anode material for PIBs because both P and Sn species undergo alloying mechanism with the discharge products of K_3P and KSn [230–233], contributing to a high theoretical capacity. Typically, Sn_4P_3 confined into N-doped carbon fibers was synthesized through the electrospinning method, followed by thermal annealing processes (Fig. 12(a)) [230]. Sn_4P_3 particles were uniformly embedded in N-doped carbon fibers, and the carbon shells can stabilize the SEI layers during repeated charge/discharge processes. In operando synchrotron X-ray diffraction (XRD) characterization suggested that both Sn and P species participate in the electrochemical redox reactions, and electrochemical tests revealed the stable cyclic performance of the as-prepared anodes, with the capacity of 160.7 $mAh·g^{-1}$ after 1,000 cycles at 500 $mA·g^{-1}$.

Other phosphides, including FeP [234, 235], Co_2P [236], and NiFeP [237], were also tested as the anodes of PIBs. For instance, Guo et al. have reported the yolk-shell structured FeP@carbon nanoboxes [234]. As shown in Fig. 12(b), the existed voids and spaces as well as the conductive host can accommodate the volume expansion and improve the electron transfer during electrochemical reactions, thus leading to greatly enhanced electrochemical performance (negligible capacity loss after 300 cycles at 0.1 $A·g^{-1}$, and 37 $mAh·g^{-1}$ at 2.0 $A·g^{-1}$). Similarly, double-shelled NiFeP/N-doped carbon nanobox was prepared via the MOF-derived method [237]. The unique architectures, including large spaces and voids as well as the presence of carbon matrix, could alleviate the volume changes, restrict the particle aggregations during cycles, and ensure the efficient contact between active materials and electrolyte. As a result, the as-prepared NiFeP/N-doped carbon nanoboxes delivered improved long-term cyclic stability with the capacities reaching 172.9 $mAh·g^{-1}$ at 500 $mA·g^{-1}$ after 1,600 cycles and 115 $mAh·g^{-1}$ at 1,000 $mA·g^{-1}$ after 2,600 cycles.

6.4 MXene

MXenes, a family of 2D materials with merits of high electronic conductivity and flexible mechanical properties, have been used as PIB anodes [238–240], and their K^+ storage performances are summarized in Table 5. Typically, Tian et al. have designed a robust, flexible, and freestanding MXene@metal film through a general one-step electrodeposition method for serving as the anodes of PIBs [238]. It was revealed that the hierarchical feature can provide a short diffusion distance for K^+ and accommodate the volume changes during cycles, while the MXene film can act as the elastic electronic highway for electron transport. As a result, the MXene@metal anodes exhibited a high specific capacity reaching 516.8 $mAh·g^{-1}$, a remarkable rate capability of 270 $mAh·g^{-1}$ at 500 $mA·g^{-1}$, and a low capacity fading rate of 0.042% per cycle. Moreover, Wu and colleagues

Table 5 Comparison of phosphides and other materials as the anodes of PIBs

Anode	Morphology	Synthesis method	Specific capacity	Cyclic performance	Ref.
Sn_4P_3/N-doped carbon fibers	Wire structure	Electrospinning combined with thermal annealing	169.6 mAh·g^{-1} at 2,000 mA·g^{-1}	160.7 mAh·g^{-1} after 1,000 cycles at 500 mA·g^{-1}	[230]
Sn_4P_3/carbon composite	Hierarchical porous structure	Solvothermal method	183.6 mAh·g^{-1} at 2,000 mA·g^{-1}	181.5 mAh·g^{-1} after 800 cycles at 500 mA·g^{-1}	[231]
$SnP_{0.94}$/GO	Nanoplate structure	Solution-based method	57 mAh·g^{-1} at 1,000 mA·g^{-1}	106 mAh·g^{-1} after 100 cycles at 200 mA·g^{-1}	[232]
Sn_4P_3/rGO	Particle structure	Ball milling	116.4 mAh·g^{-1} at 800 mA·g^{-1}	157.3 mAh·g^{-1} after 60 cycles at 600 mA·g^{-1}	[233]
FeP@carbon nanobox	Porous yolk-shell structure	Solution-based method combined with chemical vapor deposition	37 mAh·g^{-1} at 2,000 mA·g^{-1}	205 mAh·g^{-1} after 300 cycles at 100 mA·g^{-1}	[234]
FeP/carbon	Particle structure	Ball milling	288.9 mAh·g^{-1} at 50 mA·g^{-1}	63.2% capacity retention after 50 cycles at 50 mA·g^{-1}	[235]
Co_2P/rGO	Nanorod on layered structure	Solution-based method	141 mAh·g^{-1} at 2,000 mA·g^{-1}	54% capacity retention after 5,000 cycles at 200 mA·g^{-1}	[236]
NiFeP/N-doped carbon nanobox	Porous hollow structure	Solution-based method combined with thermal annealing	51.2 mAh·g^{-1} at 2,000 mA·g^{-1}	115 mAh·g^{-1} after 2,600 cycles at 1,000 mA·g^{-1}	[237]
MXene/hard carbon	Porous structure	Solution and filtration method	102.2 mAh·g^{-1} at 500 mA·g^{-1}	210 mAh·g^{-1} after 100 cycles at 50 mA·g^{-1}	[238]
MXene/Sb	Particle-like structure	Electrodeposition method	270 mAh·g^{-1} at 500 mA·g^{-1}	0.042% capacity decay per cycle for 500 cycles at 500 mA·g^{-1}	[239]
MXene nanoribbons	Porous structure	Shaking treatment	78 mAh·g^{-1} at 200 mA·g^{-1}	42 mAh·g^{-1} after 500 cycles at 200 mA·g^{-1}	[240]
TiO_xN_y/carbon composite	Particle-like structure on layers	Thermal annealing	72 mAh·g^{-1} at 1, 600 mA·g^{-1}	150 mAh·g^{-1} after 1,250 cycles at 200 mA·g^{-1}	[241]
Cobalt (II) tetrephthalate-based layered MOF	Layered structure	Solvothermal method	131 mAh·g^{-1} at 1,000 mA·g^{-1}	188 mAh·g^{-1} after 600 cycles at 1,000 mA·g^{-1}	[242]
VN quantum dots/carbon	Porous structure	Solution combustion method combined with a reduction process	152 mAh·g^{-1} at 2,000 mA·g^{-1}	215 mAh·g^{-1} after 500 cycles at 500 mA·g^{-1}	[243]

have synthesized the alkalized Ti_3C_2 MXene nanoribbons with expanded interlayer distance through the continuous shaking treatment of pristine Ti_3C_2 MXene in an aqueous KOH solution (Fig. 12(c)) [240]. The 3D interconnected porous frameworks boost ion kinetics and improve structural integrity. A reversible capacity of 136 mAh·g^{-1} at 20 mA·g^{-1}, and outstanding long-term cyclic stability with the capacity of 42 mAh·g^{-1} after 500 cycles were obtained.

For transition metal compounds, nanoscale engineering strategies were also involved in the design and construction of anodes for PIBs. The engineering of various nanostructures, such as hollow, porous, and yolk-shell, contributes to larger accessible surface areas and shorter ion diffusion pathways, thus promoting the ion transport in transition metal compounds. Applying template and solution-based synthesis are the two mainly used approaches to obtain such unique micro nanostructures. Unfortunately, transition metal compounds also suffer from poor electrical conductivity, thus restricting the electron transfer and affecting the electrochemical performance. The most effective method is to hybridize the transition metal compounds with carbonaceous materials. As such, the incorporation of carbonaceous materials not only improves the electrical conductivity of transition metal compounds but also boosts their structural stability during the electrochemical process, thus enabling excellent cyclic stability and rate performance.

7 Other materials

TiO_xN_y [241], MOFs [242], and nitrides [243], were also reported as the PIB anodes, as shown in Table 5. For instance, cobalt (II) tetrephthalate-based layered MOF was designed and fabricated as PIB anodes [242]. It was found that both the Co centers and organic ligands could participate in the K^+ storage, and the coordination between oxygen ions and Co ensured the high reversibility of K^+ intercalation/deintercalation processes. Finally, the as-prepared anodes displayed a reversible capacity as high as 188 mAh·g^{-1} after 600 cycles at 1.0 A·g^{-1}, indicating that MOFs can be used as superior electrodes for K^+ storage.

8 Conclusions and future perspectives

In summary, PIBs have attracted tremendous interests because of the high energy density, wide potential window, and abundant K sources. The anode materials currently suffer from narrow interlayer spacing, low electrical conductivity, and serious volume expansion, all of which will undoubtedly restrict the commercial-scale applications of PIBs. To resolve these issues, different electrode design strategies were explored towards various types of anode materials, including carbonaceous materials, metals alloys, oxides, sulfides, selenides, and others, as a result, these anodes can deliver excellent electrochemical performances in terms of reversible capacity, rate capability, and long-life cyclic stability. In this review, recent developments in the rational design and engineering of anode materials (conductive materials, nanostructure engineering, etc.) are carefully reviewed and discussed. Notably, the current progress on the anode materials of PIBs is far from satisfactory, especially for practical applications. In addition, many scientific questions are yet to be answered and novel designs of advanced anode materials are still needed. Herein we list some important directions for future research and development:

(1) Increasing K^+ intercalation/deintercalation kinetics can indeed improve the electrochemical performances of PIBs. To this end, the main strategy lies in the design and engineering

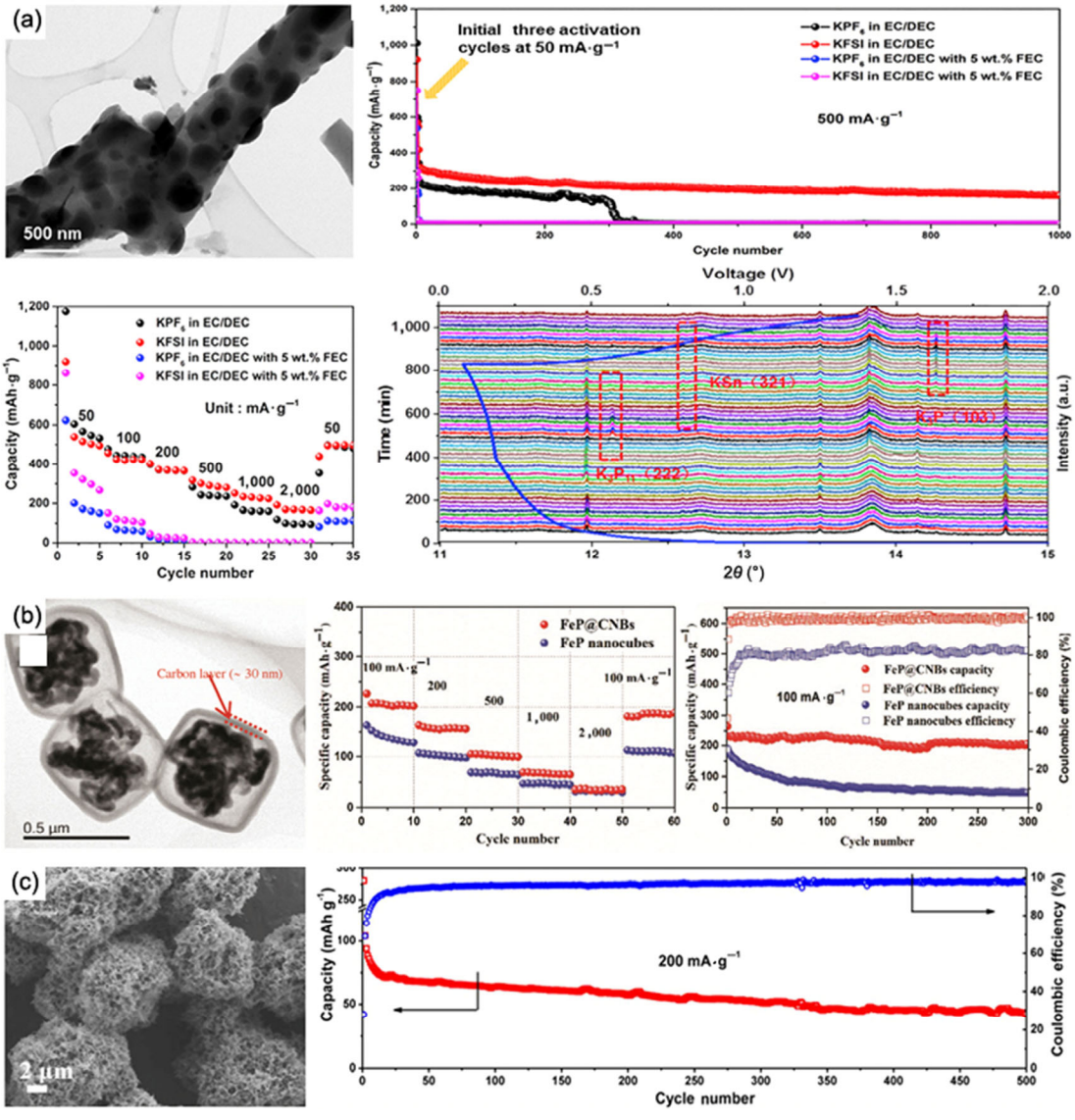

Figure 12 (a) TEM image of Sn_4P_3@carbon fiber, K^+ storage performance, and in operando synchrotron XRD characterizations of the anode during potassiation/depotassiation processes. Reprinted with permission from Ref. [230], © Elsevier Inc. 2018. (b) TEM image of FeP@carbon and the electrochemical performance of PIBs. Reprinted with permission from Ref. [234], © WILEY-VCH Verlag GmbH & Co. KGaA, Weinheim 2019. (c) SEM image of Ti_3C_2 MXene and the cycle stability under 200 mA·g^{-1}. Reprinted with permission from Ref. [240], © Elsevier Ltd. 2017.

of carbon matrix with enlarged interlayer distances to serve as the anode materials; however, this strategy has its intrinsic limits and the interlayer spacing can only be broadened to some extent. Therefore, novel strategies aimed at boosting the K^+ diffusion kinetics is extremely needed. For instance, heteroatom doping can not only enlarge the interlayer spacing but also modify the electronic structure of carbon materials. In this regard, precise control of heteroatom doping with a tunable amount needs to be achieved.

(2) The detailed working mechanisms of different types of anode materials should be figured out, in order to provide reliable guidance for future design and construction of novel anode materials. The reaction mechanisms of anode materials in PIBs are not the same as in LIBs and SIBs. Currently, the K^+ storage performance of the carbon matrix is mainly attributed to the intercalation/deintercalation behaviors of K^+ ions into the interlayers of carbonaceous materials, but for heteroatoms doped carbon matrix, the redox reactions can also be found and this would contribute to part of the K^+ storage capability. Moreover, for other materials, the electrochemical performances mainly originated from the redox reactions of inorganic materials with K^+ to form different intermediates and sequentially final products; however, the intercalation/deintercalation behavior should also be responsible for part of the electrochemical capacity. The accurate contributions of different working mechanisms need to be precisely determined, and the related influence factors needed to be examined, to facilitate the future practical applications.

(3) The interplay between anode materials and electrolytes should be well clarified, given that even the same material shows distinct cyclic stability in different electrolytes. For instance, it was revealed that increasing the salt concentration in the diglyme-based electrolyte could greatly enhance the cyclic stability of PIBs [244]. Therefore, developing a suitable electrolyte for a specific type of anode material is crucial for achieving better electrochemical performance. The underlined reduction mechanisms of electrolytes on different anode materials should be clarified. More importantly, the exploration and optimization of new electrolyte systems are crucial to improving electrochemical performance. The currently utilized electrolyte systems could lead to low initial Coulombic efficiencies, affecting the total electrochemical performance of anodes. Besides the adjustment of electrolyte additives and solvent, developing new electrolyte salts and all-solid-state

electrolytes will be another efficient strategy. This will largely overcome the destructive issues faced by PIBs. Finally, maybe K metals can be directly used as the anodes in practical applications, once resolving the safety problem of K metal when exposing to the air.

(4) Theoretical understanding of the anode materials of PIBs is still lacking. To better guide the design and construction of anodes, theoretical calculations are needed to investigate the intrinsic properties and evaluate the suitability of such materials to act as the anodes of PIBs. Moreover, the working mechanisms and theoretical capacities of different types of anode materials need to be examined in-depth. Experimental investigations need to progress accordingly to test the predictions given by theoretical simulations.

(5) Advanced techniques are in urgent need to characterize the composition and structure evolutions of anode materials during potassiation/depotassiation cycles. For instance, cryo-electron microscopy (cryo-EM) can be used to investigate the growth of SEI layers, and examine their working mechanisms in K^+ storage. Moreover, *in situ* and *ex situ* characterization tools, like *in/ex situ* Raman spectroscopy, *in/ex situ* Fourier transform infrared (FT-IR) spectroscopy, *in/ex situ* X-ray absorption fine structure (XAFS) spectroscopy, *in/ex situ* nuclear magnetic resonance (NMR) imaging, and aberration-corrected scanning transmission electron microscopy (STEM) can be conducted to help find the underlined working mechanisms based on electrochemical redox reactions. It should be noted that a single characterization tool is not enough o obtain sufficient useful information; thus multiple techniques should be carried out together in some cases. Also, the development of new and creative characterization systems is encouraged in probing in-depth mechanisms.

(6) The investigations on PIB full-cells need to be further conducted. So far, most of the achieved electrochemical performances were tested on half-cells. For PIB full-cells, the matching of cathodic and anodic materials, the amount ratio of electroactive materials, as well as the electrolyte, should be considered. Moreover, the durability tests of PIB full-cells under harsh environments, such as high/low working temperatures and high humidity atmosphere, need to be conducted in order to cater the practical applications.

(7) The synthesis procedures of anode materials normally involve the expensive facilities and complicated processes, which seriously restricted their commercial application. Moreover, the current achieved electrochemical performances of PIBs are still below the requirements for real applications, in terms of energy density, reversible capacity, rate capability, and long-term cyclic lifespan. More efforts should be devoted to constructing new anode materials using novel approaches.

(8) Last but not least, to promote the commercial application of anode materials for PIBs, the earth-abundant, non-toxic, and low-cost raw materials have to been used. Figure 13 shows the cost of different elements that have been used for the PIB anodes. In general, carbon-based materials have the lowest cost, however, the capacity is relatively low. Among different metal compounds, Fe, Mn, and Zn-based compounds are compounds favorable for low-cost PIB anodes thanks to the low cost of Fe, Mn, and Zn, while Sn- and Bi-based compounds typically have higher capacities due to the conversion and alloying reactions. It is worth noting that phosphorous not only has a low price but shows an intriguing capacity (843 $mAh \cdot g^{-1}$, for potassium phosphide (KP)), which is rather attractive in PIBs. For practical application, both the cost and performances of anode materials should be considered and well balanced under specific conditions.

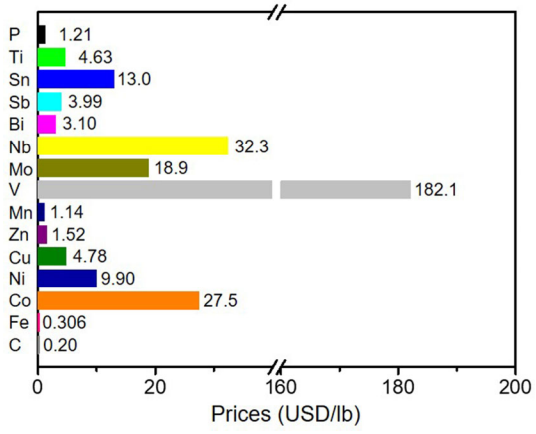

Figure 13 Price comparison of carbon, phosphorous, and various metals for potential applications in PIBs. (The data was collected on website from https://www.shmet.com)

In summary, PIBs have attracted numerous attentions as an alternative to traditional LIBs. Although great progress has already been achieved, the development of PIBs is still in its infancy. More experimental conductions and theoretical simulations on the anode materials of PIBs are required in the future. Given the rapid development of anode materials and in understanding of working mechanisms, the commercial applications of PIBs are expected to be realized in the near future.

Acknowledgements

This project was financially supported by the National Key Research and Development Program of China (No. 2017YFA0208200), the National Natural Science Foundation of China (Nos. 22005003, 22022505, and 21872069), the Fundamental Research Funds for the Central Universities (Nos. 0205-14380219 and 0205-14913212), the Scientific Research Foundation of Anhui University of Technology for Talent Introduction (No. DT19100069), the Yong Scientific Research Foundation of Anhui University of Technology (No. QZ202003), the Natural Science Foundation of Jiangsu Province (No. BK20180008), the Shenzhen Fundamental Research Program of Science, Technology, and Innovation Commission of Shenzhen Municipality (No. JCYJ20180307155007589).

References

[1] Tarascon, J. M.; Armand, M. Issues and challenges facing rechargeable lithium batteries. *Nature* **2001**, *414*, 359–367.

[2] Armand, M.; Tarascon, J. M. Building better batteries. *Nature* **2008**, *451*, 652–657.

[3] Zhuang, Z. C.; Kang, Q.; Wang, D. S.; Li, Y. D. Single-atom catalysis enables long-life, high-energy lithium-sulfur batteries. *Nano Res.* **2020**, *13*, 1856–1866.

[4] Scrosati, B.; Garche, J. Lithium batteries: Status, prospects and future. *J. Power Sources* **2010**, *195*, 2419–2430.

[5] Reddy, M. V.; Rao, G. V. S.; Chowdari, B. V. R. Metal oxides and oxysalts as anode materials for Li ion batteries. *Chem. Rev.* **2013**, *113*, 5364–5457.

[6] Bruce, P. G.; Scrosati, B.; Tarascon, J. M. Nanomaterials for rechargeable lithium batteries. *Angew. Chem., Int. Ed.* **2008**, *47*, 2930–2946.

[7] Etacheri, V.; Marom, R.; Elazari, R.; Salitra, G.; Aurbach, D. Challenges in the development of advanced Li-ion batteries: A review. *Energy Environ. Sci.* **2011**, *4*, 3243–3262.

[8] Li, X. R.; Yang, X. C.; Xue, H. G.; Pang, H.; Xu, Q. Metal-organic frameworks as a platform for clean energy applications. *EnergyChem* **2020**, *2*, 100027.

[9] Chen, Y.; Zhuo, S. M.; Li, Z. Y.; Wang, C. L. Redox polymers for rechargeable metal-ion batteries. *EnergyChem* **2020**, *2*, 100030.

[10] Cheng, Y.; Xiao, X.; Pan, K. M.; Pang, H. Development and application of self-healing materials in smart batteries and supercapacitors. *Chem. Eng. J.* **2020**, *380*, 122565.

[11] Yang, S. N.; Cheng, Y.; Xiao, X.; Pang, H. Development and application of carbon fiber in batteries. *Chem. Eng. J.* **2020**, *384*, 123294.

[12] Chen, M. Z.; Wang, E. H.; Liu, Q. N.; Guo, X. D.; Chen, W. H.; Chou, S. L.; Dou, S. X. Recent progress on iron- and manganese-based anodes for sodium-ion and potassium-ion batteries. *Energy Storage Mater.* **2019**, *19*, 163–178.

[13] Li, Y. M.; Lu, Y. X.; Zhao, C. L.; Hu, Y. S.; Titirici, M. M.; Li, H.; Huang, X. J.; Chen, L. Q. Recent advances of electrode materials for low-cost sodium-ion batteries towards practical application for grid energy storage. *Energy Storage Mater.* **2017**, *7*, 130–151.

[14] Chen, M. Z.; Cortie, D.; Hu, Z.; Jin, H. L.; Wang, S.; Gu, Q. F.; Hua, W. B.; Wang, E. H.; Lai, W. H.; Chen, L. N. et al. A novel graphene oxide wrapped $Na_2Fe_2(SO_4)_3$/C cathode composite for long life and high energy density sodium-ion batteries. *Adv. Energy Mater.* **2018**, *8*, 1800944.

[15] Xu, Y. S.; Duan, S. Y.; Sun, Y. G.; Bin, D. S.; Tao, X. S.; Zhang, D.; Liu, Y.; Cao, A. M.; Wan, L. J. Recent developments in electrode materials for potassium-ion batteries. *J. Mater. Chem. A* **2019**, *7*, 4334–4352.

[16] Luo, W.; Wan, J. Y.; Ozdemir, B.; Bao, W. Z.; Chen, Y. N.; Dai, J. Q.; Lin, H.; Xu, Y.; Gu, F.; Barone, V. et al. Potassium ion batteries with graphitic materials. *Nano Lett.* **2015**, *15*, 7671–7677.

[17] Wu, X.; Chen, Y. L.; Xing, Z.; Lam, C. W. K.; Pang, S. S.; Zhang, W.; Ju, Z. C. Advanced carbon-based anodes for potassium-ion batteries. *Adv. Energy Mater.* **2019**, *9*, 1900343.

[18] Ma, L. B.; Cui, J.; Yao, S. S.; Liu, X. M.; Luo, Y. S.; Shen, X. P.; Kim, J. K. Dendrite-free lithium metal and sodium metal batteries. *Energy Storage Mater.* **2020**, *27*, 522–554.

[19] Ma, L. B.; Zhu, G. Y.; Wang, D. D.; Chen, H. X.; Lv, Y. H.; Zhang, Y. Z.; He, X. J.; Pang, H. Emerging metal single atoms in electrocatalysts and batteries. *Adv. Funct. Mater.* **2020**, *30*, 2003870.

[20] Sultana, I.; Rahman, M. M.; Chen, Y.; Glushenkov, A. M. Potassium-ion battery anode materials operating through the alloying–dealloying reaction mechanism. *Adv. Funct. Mater.* **2018**, *28*, 1703857.

[21] Palomares, V.; Serras, P.; Villaluenga, I.; Hueso, K. B.; Carretero-González, J.; Rojo, T. Na-ion batteries, recent advances and present challenges to become low cost energy storage systems. *Energy Environ. Sci.* **2012**, *5*, 5884–5901.

[22] Su, D. W.; Wang, G. X. Single-crystalline bilayered V_2O_5 nanobelts for high-capacity sodium-ion batteries. *ACS Nano* **2013**, *7*, 11218–11226.

[23] An, Y. L.; Fei, H. F.; Zeng, G. F.; Ci, L. J.; Xi, B. J.; Xiong, S. L.; Feng, J. K. Commercial expanded graphite as a low-cost, long-cycling life anode for potassium-ion batteries with conventional carbonate electrolyte. *J. Power Sources* **2018**, *378*, 66–72.

[24] Jian, Z. L.; Luo, W.; Ji, X. L. Carbon electrodes for K-ion batteries. *J. Am. Chem. Soc.* **2015**, *137*, 11566–11569.

[25] Zhang, W. C.; Mao, J. F.; Li, S.; Chen, Z. X.; Guo, Z. P. Phosphorus-based alloy materials for advanced potassium-ion battery anode. *J. Am. Chem. Soc.* **2017**, *139*, 3316–3319.

[26] Zhu, B.; Wang, X. Y.; Yao, P. C.; Li, J. L.; Zhu, J. Towards high energy density lithium battery anodes: Silicon and lithium. *Chem. Sci.* **2019**, *10*, 7132–7148.

[27] Wu, J. X.; Qin, X. Y.; Zhang, H. R.; He, Y. B.; Li, B. H.; Ke, L.; Lv, W.; Du, H. D.; Yang, Q. H.; Kang, F. Y. Multilayered silicon embedded porous carbon/graphene hybrid film as a high performance anode. *Carbon* **2015**, *84*, 434–443.

[28] Wu, J. X.; Qin, X. Y.; Miao, C.; He, Y. B.; Liang, G. M.; Zhou, D.; Liu, M.; Han, C. P.; Li, B. H.; Kang, F. Y. A honeycomb-cobweb inspired hierarchical core–shell structure design for electrospun silicon/carbon fibers as lithium-ion battery anodes. *Carbon* **2016**, *98*, 582–591.

[29] Ren, X. D.; Wu, Y. Y. A low-overpotential potassium–oxygen battery based on potassium superoxide. *J. Am. Chem. Soc.* **2013**, *135*, 2923–2926.

[30] Komaba, S.; Hasegawa, T.; Dahbi, M.; Kubota, K. Potassium intercalation into graphite to realize high-voltage/high-power potassium-ion batteries and potassium-ion capacitors. *Electrochem. Commun.* **2015**, *60*, 172–175.

[31] Frackowiak, E.; Béguin, F. Carbon materials for the electrochemical storage of energy in capacitors. *Carbon* **2001**, *39*, 937–950.

[32] Pandolfo, A. G.; Hollenkamp, A. F. Carbon properties and their role in supercapacitors. *J. Power Sources* **2006**, *157*, 11–27.

[33] Zhu, Y. W.; Murali, S.; Stoller, M. D.; Ganesh, K. J.; Cai, W. W.; Ferreira, P. J.; Pirkle, A.; Wallace, R. M.; Cychosz, K. A.; Thommes, M. et al. Carbon-based supercapacitors produced by activation of graphene. *Science* **2011**, *332*, 1537–1541.

[34] Huang, X.; Zeng, Z. Y.; Fan, Z. X.; Liu, J. Q.; Zhang, H. Graphene-based electrodes. *Adv. Mater.* **2012**, *24*, 5979–6004.

[35] Deng, S. K.; Berry, V. Wrinkled, rippled and crumpled graphene: An overview of formation mechanism, electronic properties, and applications. *Mater. Today* **2016**, *19*, 197–212.

[36] Liu, L. Y.; Lin, Z. F.; Chane-Ching, J. Y.; Shao, H.; Taberna, P. L.; Simon, P. 3D rGO aerogel with superior electrochemical performance for K-ion battery. *Energy Storage Mater.* **2019**, *19*, 306–313.

[37] Chen, Y. C.; Qin, L.; Lei, Y.; Li, X. J.; Dong, J. H.; Zhai, D. Y.; Li, B. H.; Kang, F. Y. Correlation between microstructure and potassium storage behavior in reduced graphene oxide materials. *ACS Appl. Mater. Inter.* **2019**, *11*, 45578–45585.

[38] Wang, X. W.; Sun, G. Z.; Routh, P.; Kim, D. H.; Huang, W.; Chen, P. Heteroatom-doped graphene materials: Syntheses, properties and applications. *Chem. Soc. Rev.* **2014**, *43*, 7067–7098.

[39] Xue, Y. Z.; Wu, B.; Bao, Q. L.; Liu, Y. Q. Controllable synthesis of doped graphene and its applications. *Small* **2014**, *10*, 2975–2991.

[40] Wen, Y. Y.; Huang, C. C.; Wang, L. Z.; Hulicova-Jurcakova, D. Heteroatom-doped graphene for electrochemical energy storage. *Chin. Sci. Bull.* **2014**, *59*, 2102–2121.

[41] Ju, Z. C.; Li, P. Z.; Ma, G. Y.; Xing, Z.; Zhuang, Q. C.; Qian, Y. T. Few layer nitrogen-doped graphene with highly reversible potassium storage. *Energy Storage Mater.* **2018**, *11*, 38–46.

[42] Qiu, W. D.; Xiao, H. B.; Li, Y.; Lu, X. H.; Tong, Y. X. Nitrogen and phosphorus codoped vertical graphene/carbon cloth as a binder-free anode for flexible advanced potassium ion full batteries. *Small* **2019**, *15*, 1901285.

[43] Ju, Z. C.; Zhang, S.; Xing, Z.; Zhuang, Q. C.; Qiang, Y. H.; Qian, Y. T. Direct synthesis of few-layer F-doped graphene foam and its lithium/potassium storage properties. *ACS Appl. Mater. Inter.* **2016**, *8*, 20682–20690.

[44] Tang, Y. F.; Zhao, Y.; Burkert, S. C.; Ding, M. N.; Ellis, J. E.; Star, A. Efficient separation of nitrogen-doped carbon nanotube cups. *Carbon* **2014**, *80*, 583–590.

[45] Tang, Y. F.; Burkert, S. C.; Zhao, Y.; Saidi, W. A.; Star, A. The effect of metal catalyst on the electrocatalytic activity of nitrogen-doped carbon nanotubes. *J. Phys. Chem. C* **2013**, *117*, 25213–25221.

[46] Li, J. C.; Kaur, A. P.; Meier, M. S.; Cheng, Y. T. Stacked-cup-type MWCNTs as highly stable lithium-ion battery anodes. *J. Appl. Electrochem.* **2014**, *44*, 179–187.

[47] Wang, B.; Yuan, F.; Wang, W.; Zhang, D.; Sun, H. L.; Xi, K.; Wang, D. L.; Chu, J. H.; Wang, Q. J.; Li, W. A carbon microtube array with a multihole cross profile: Releasing the stress and boosting long-cycling and high-rate potassium ion storage. *J. Mater. Chem. A* **2019**, *7*, 25845–25852.

[48] Moussa, M.; Al-Bataineh, S. A.; Losic, D.; Dubal, D. P. Engineering of high-performance potassium-ion capacitors using polyaniline-derived N-doped carbon nanotubes anode and laser scribed graphene oxide cathode. *Appl. Mater. Today* **2019**, *16*, 425–434.

[49] Yu, Y.; Luo, Y. F.; Wu, H. C.; Jiang, K. L.; Li, Q. Q.; Fan, S. S.; Li, J.; Wang, J. P. Ultrastretchable carbon nanotube composite electrodes for flexible lithium-ion batteries. *Nanoscale* **2018**, *10*, 19972–19978.

[50] Chew, S. Y.; Ng, S. H.; Wang, J. Z.; Novák, P.; Krumeich, F.; Chou, S. L.; Chen, J.; Liu, H. K. Flexible free-standing carbon nanotube films for model lithium-ion batteries. *Carbon* **2009**, *47*, 2976–2983.

[51] Zhao, X. X.; Tang, Y. F.; Ni, C. L.; Wang, J. W.; Star, A.; Xu, Y. H. Free-standing nitrogen-doped cup-stacked carbon nanotube mats for potassium-ion battery anodes. *ACS Appl. Energy Mater.* **2018**, *1*, 1703–1707.

[52] Shen, C.; Yuan, K.; Tian, T.; Bai, M. H.; Wang, J. G.; Li, X. F.; Xie, K. Y.; Fu, Q. G.; Wei, B. Q. Flexible sub-micro carbon fiber@CNTs

as anodes for potassium-ion batteries. *ACS Appl. Mater. Inter.* **2019**, *11*, 5015–5021.

[53] Hu, Y. X.; Debnath, S.; Hu, H.; Luo, B.; Zhu, X. B.; Wang, S. C.; Hankel, M.; Searles, D. J.; Wang, L. Z. Unlocking the potential of commercial carbon nanofibers as free-standing positive electrodes for flexible aluminum ion batteries. *J. Mater. Chem. A* **2019**, *7*, 15123–15130.

[54] Wang, Y. W.; Xiao, N.; Wang, Z. Y.; Tang, Y. C.; Li, H. Q.; Yu, M. L.; Liu, C.; Zhou, Y.; Qiu, J. S. Ultrastable and high-capacity carbon nanofiber anodes derived from pitch/polyacrylonitrile for flexible sodium-ion batteries. *Carbon* **2018**, 135, 187–194.

[55] Li, W. H.; Li, M. S.; Adair, K. R.; Sun, X. L.; Yu, Y. Carbon nanofiber-based nanostructures for lithium-ion and sodium-ion batteries. *J. Mater. Chem. A* **2017**, *5*, 13882–13906.

[56] Xu, Y.; Zhang, C. L.; Zhou, M.; Fu, Q.; Zhao, C. X.; Wu, M. H.; Lei, Y. Highly nitrogen doped carbon nanofibers with superior rate capability and cyclability for potassium ion batteries. *Nat. Commun.* **2018**, *9*, 1720.

[57] Zhang, M.; Shoaib, M.; Fei, H. L.; Wang, T.; Zhong, J.; Fan, L.; Wang, L.; Luo, H. Y.; Tan, S.; Wang, Y. Y. et al. Hierarchically porous N-doped carbon fibers as a free-standing anode for high-capacity potassium-based dual-ion battery. *Adv. Energy Mater.* **2019**, *9*, 1901663.

[58] Xu, Y.; Yuan, T.; Zhao, Y. H.; Yao, H. F.; Yang, J. H.; Zheng, S. Y. Constructing multichannel carbon fibers as freestanding anodes for potassium-ion battery with high capacity and long cycle life. *Adv. Mater. Inter.* **2020**, *7*, 1901829.

[59] Xie, Y. H.; Chen, Y.; Liu, L.; Tao, P.; Fan, M. P.; Xu, N.; Shen, X. W.; Yan, C. L. Ultra-high pyridinic N-doped porous carbon monolith enabling high-capacity K-ion battery anodes for both half-cell and full-cell applications. *Adv. Mater.* **2017**, *29*, 1702268.

[60] Sun, X. Z.; Wang, C. L.; Gong, Y.; Gu, L.; Chen, Q. W.; Yu, Y. A flexible sulfur-enriched nitrogen doped multichannel hollow carbon nanofibers film for high performance sodium storage. *Small* **2018**, *14*, 1802218.

[61] Hao, R.; Lan, H.; Kuang, C. W.; Wang, H.; Guo, L. Superior potassium storage in chitin-derived natural nitrogen-doped carbon nanofibers. *Carbon* **2018**, *128*, 224–230.

[62] Zhai, Y. P.; Dou, Y. Q.; Zhao, D. Y.; Fulvio, P. F.; Mayes, R. T.; Dai, S. Carbon materials for chemical capacitive energy storage. *Adv. Mater.* **2011**, *23*, 4828–4850.

[63] Liang, C. D.; Li, Z. J.; Dai, S. Mesoporous carbon materials: Synthesis and modification. *Angew. Chem., Int. Ed.* **2008**, *47*, 3696–3717.

[64] Dutta, S.; Bhaumik, A.; Wu, K. C. W. Hierarchically porous carbon derived from polymers and biomass: Effect of interconnected pores on energy applications. *Energy Environ. Sci.* **2014**, *7*, 3574–3592.

[65] Zhou, X. F.; Chen, L. L.; Zhang, W. H.; Wang, J. W.; Liu, Z. J.; Zeng, S. F.; Xu, R.; Wu, Y.; Ye, S. F.; Feng, Y. Z. et al. Three-dimensional ordered macroporous metal−organic framework single crystal-derived nitrogen-doped hierarchical porous carbon for high-performance potassium-ion batteries. *Nano Lett.* **2019**, *19*, 4965–4973.

[66] Wang, G.; Xiong, X. H.; Xie, D.; Lin, Z. H.; Zheng, J.; Zheng, F. H.; Li, Y. P.; Liu, Y. Z.; Yang, C. H.; Liu, M. L. Chemically activated hollow carbon nanospheres as a high-performance anode material for potassium ion batteries. *J. Mater. Chem. A* **2018**, *6*, 24317–24323.

[67] Ruan, J. F.; Wu, X.; Wang, Y.; Zheng, S. Y.; Sun, D. L.; Song, Y.; Chen, M. Nitrogen-doped hollow carbon nanospheres towards the application of potassium ion storage. *J. Mater. Chem. A* **2019**, *7*, 19305–19315.

[68] Yang, W. X.; Zhou, J. H.; Wang, S.; Zhang, W. Y.; Wang, Z. C.; Lv, F.; Wang, K.; Sun, Q.; Guo, S. J. Freestanding film made by necklace-like N-doped hollow carbon with hierarchical pores for high-performance potassium-ion storage. *Energy Environ. Sci.* **2019**, *12*, 1605–1612.

[69] Zhang, Y.; Yang, L.; Tian, Y.; Li, L.; Li, J. Y.; Qiu, Y. Y.; Zou, G. Q.; Hou, H. S.; Ji, X. B. Honeycomb hard carbon derived from carbon quantum dots as anode material for K-ion batteries. *Mater. Chem. Phys.* **2019**, *229*, 303–309.

[70] Hong, W. W.; Zhang, Y.; Yang, L.; Tian, Y.; Ge, P.; Hu, J. G.; Wei, W. F.; Zou, G. Q.; Hou, H. S.; Ji, X. B. Carbon quantum dot micelles tailored hollow carbon anode for fast potassium and sodium storage. *Nano Energy* **2019**, *65*, 104038.

[71] Hu, X.; Liu, Y. J.; Chen, J. X.; Yi, L. C.; Zhan, H. B.; Wen, Z. H. Fast redox kinetics in Bi-heteroatom doped 3D porous carbon nanosheets for high-performance hybrid potassium-ion battery capacitors. *Adv. Energy Mater.* **2019**, *9*, 1901533.

[72] Qin, J.; Sari, H. M. K.; He, C. N.; Li, X. F. A hybrid energy storage mechanism of carbonous anodes harvesting superior rate capability and long cycle life for sodium/potassium storage. *J. Mater. Chem. A* **2019**, *7*, 3673–3681.

[73] Zhang, W. L.; Ming, J.; Zhao, W. L.; Dong, X. C.; Hedhili, M. N.; Costa, P. M. F. J.; Alshareef, H. N. Graphitic nanocarbon with engineered defects for high-performance potassium-ion battery anodes. *Adv. Funct. Mater.* **2019**, *29*, 1903641.

[74] Liu, S. T.; Yang, B. B.; Zhou, J. S.; Song, H. H. Nitrogen-rich carbon-onion-constructed nanosheets: An ultrafast and ultrastable dual anode material for sodium and potassium storage. *J. Mater. Chem. A* **2019**, *7*, 18499–18509.

[75] Cao, B.; Zhang, Q.; Liu, H.; Xu, B.; Zhang, S. L.; Zhou, T. F.; Mao, J. F.; Pang, W. K.; Guo, Z. P.; Li, A. et al. Graphitic carbon nanocage as a stable and high power anode for potassium-ion batteries. *Adv. Energy Mater.* **2018**, *8*, 1801149.

[76] Xiao, N.; Zhang, X. Y.; Liu, C.; Wang, Y. W.; Li, H. Q.; Qiu, J. S. Coal-based carbon anodes for high-performance potassium-ion batteries. *Carbon* **2019**, *147*, 574–581.

[77] Qian, Y.; Jiang, S.; Li, Y.; Yi, Z.; Zhou, J.; Li, T. Q.; Han, Y.; Wang, Y. S.; Tian, J.; Lin, N. et al. *In situ* revealing the electroactivity of P–O and P–C bonds in hard carbon for high-capacity and long-life Li/K-ion batteries. *Adv. Energy Mater.* **2019**, *9*, 1901676.

[78] Kamiyama, A.; Kubota, K.; Nakano, T.; Fujimura, S.; Shiraishi, S.; Tsukada, H.; Komaba, S. High-capacity hard carbon synthesized from macroporous phenolic resin for sodium-ion and potassium-ion battery. *ACS Appl. Energy Mater.* **2020**, *3*, 135–140.

[79] Qian, Y.; Jiang, S.; Li, Y.; Yi, Z.; Zhou, J.; Tian, J.; Lin, N.; Qian, Y. T. Water-induced growth of a highly oriented mesoporous graphitic carbon nanospring for fast potassium-ion adsorption/intercalation storage. *Angew. Chem., Int. Ed.* **2019**, *58*, 18108–18115.

[80] Mahmood, A.; Li, S.; Ali, Z.; Tabassum, H.; Zhu, B. J.; Liang, Z. B.; Meng, W.; Aftab, W.; Guo, W. H.; Zhang, H. et al. Ultrafast sodium/potassium-ion intercalation into hierarchically porous thin carbon shells. *Adv. Mater.* **2019**, *31*, 1805430.

[81] Li, Y. P.; Yang, C. H.; Zheng, F. H.; Ou, X.; Pan, Q. C.; Liu, Y. Z.; Wang, G. High pyridine N-doped porous carbon derived from metal–organic frameworks for boosting potassium-ion storage. *J. Mater. Chem. A* **2018**, *6*, 17959–17966.

[82] Jian, Z. L.; Hwang, S.; Li, Z. F.; Hernandez, A. S.; Wang, X. F.; Xing, Z. Y.; Su, D.; Ji, X. L. Hard–soft composite carbon as a long-cycling and high-rate anode for potassium-ion batteries. *Adv. Funct. Mater.* **2017**, *27*, 1700324.

[83] Zhang, W. L.; Cao, Z.; Wang, W. X.; Alhajji, E.; Emwas, A. H.; Costa, P. M. F. J.; Cavallo, L.; Alshareef, H. N. A site-selective doping strategy of carbon anodes with remarkable K-ion storage capacity. *Angew. Chem., Int. Ed.* **2020**, *59*, 4448–4455.

[84] Liu, Y.; Dai, H. D.; Wu, L.; Zhou, W. B.; He, L.; Wang, W. G.; Yan, W. Q.; Huang, Q. H.; Fu, L. J.; Wu, Y. P. A large scalable and low-cost sulfur/nitrogen dual-doped hard carbon as the negative electrode material for high-performance potassium-ion batteries. *Adv. Energy Mater.* **2019**, *9*, 1901379.

[85] Lin, X. Y.; Huang, J. Q.; Zhang, B. Correlation between the microstructure of carbon materials and their potassium ion storage performance. *Carbon* **2019**, *143*, 138–146.

[86] Wang, W.; Zhou, J. H.; Wang, Z. P.; Zhao, L. Y.; Li, P. H.; Yang, Y.; Yang, C.; Huang, H. X.; Guo, S. J. Short-range order in mesoporous carbon boosts potassium-ion battery performance. *Adv. Energy Mater.* **2018**, *8*, 1701648.

[87] Yamamoto, H.; Muratsubaki, S.; Kubota, K.; Fukunishi, M.; Watanabe, H.; Kim, J.; Komaba, S. Synthesizing higher-capacity hard-carbons from cellulose for Na- and K-ion batteries. *J. Mater. Chem. A* **2018**, *6*, 16844–16848.

[88] Zhang, Z. L.; Jia, B. R.; Liu, L.; Zhao, Y. Z.; Wu, H. Y.; Qin, M. L.; Han, K.; Wang, W. A.; Xi, K.; Zhang, L. et al. Hollow multihole carbon bowls: A stress–release structure design for high-stability and high-volumetric-capacity potassium-ion batteries. *ACS Nano* **2019**, *13*, 11363–11371.

[89] Gao, C. L.; Wang, Q.; Luo, S. H.; Wang, Z. Y.; Zhang, Y. H.; Liu, Y. G.; Hao, A. M.; Guo, R. High performance potassium-ion battery anode based on biomorphic N-doped carbon derived from walnut septum. *J. Power Sources* **2019**, *415*, 165–171.
[90] Arnaiz, M.; Bothe, A.; Dsoke, S.; Balducci, A.; Ajuria, J. Aprotic and protic ionic liquids combined with olive pits derived hard carbon for potassium-ion batteries. *J. Electrochem. Soc.* **2019**, *166*, A3504−A3510.
[91] Chen, C. J.; Wang, Z. G.; Zhang, B.; Miao, L.; Cai, J.; Peng, L. F.; Huang, Y. Y.; Jiang, J. J.; Huang, Y. H.; Zhang, L. N. et al. Nitrogen-rich hard carbon as a highly durable anode for high-power potassium-ion batteries. *Energy Storage Mater.* **2017**, *8*, 161–168.
[92] Li, H. Y.; Cheng, Z.; Zhang, Q.; Natan, A.; Yang, Y.; Cao, D. X.; Zhu, H. L. Bacterial-derived, compressible, and hierarchical porous carbon for high-performance potassium-ion batteries. *Nano Lett.* **2018**, *18*, 7407–7413.
[93] Chen, C.; Wu, M. Q.; Wang, Y. S.; Zaghib, K. Insights into pseudographite-structured hard carbon with stabilized performance for high energy K-ion storage. *J. Power Sources* **2019**, *444*, 227310.
[94] Qi, X. J.; Huang, K. S.; Xu, X.; Zhao, W.; Wang, H.; Zhuang, Q. C.; Ju, Z. C. Novel fabrication of N-doped hierarchically porous carbon with exceptional potassium storage properties. *Carbon* **2018**, *131*, 79–85.
[95] Ma, H. L.; Qi, X. J.; Peng, D. Q.; Chen, Y. X.; Wei, D. H.; Ju, Z. C.; Zhuang, Q. C. Novel fabrication of N/S Co-doped hierarchically porous carbon for potassium-ion batteries. *Chem. Select* **2019**, *4*, 11488–11495.
[96] Wu, X.; Lam, C. W. K.; Wu, N. Q.; Pang, S. S.; Xing, Z.; Zhang, W.; Ju, Z. C. Multiple templates fabrication of hierarchical porous carbon for enhanced rate capability in potassium-ion batteries. *Mater. Today Energy* **2019**, *11*, 182–191.
[97] Zhang, R.; Li, H. B.; Li, R.; Wei, D. H.; Kang, W. J.; Ju, Z. C.; Xiong, S. L. Boosting the potassium-ion storage performance of a carbon anode by chemically regulating oxygen-containing species. *Chem. Commun.* **2019**, *55*, 14147–14150.
[98] Sun, Q.; Li, D. P.; Cheng, J.; Dai, L. N.; Guo, J. G.; Liang, Z.; Ci, L. J. Nitrogen-doped carbon derived from pre-oxidized pitch for surface dominated potassium-ion storage. *Carbon* **2019**, *155*, 601–610.
[99] Li, Y. P.; Zhong, W. T.; Yang, C. H.; Zheng, F. H.; Pan, Q. C.; Liu, Y. Z.; Wang, G.; Xiong, X. H.; Liu, M. L. N/S codoped carbon microboxes with expanded interlayer distance toward excellent potassium storage. *Chem. Eng. J.* **2019**, *358*, 1147–1154.
[100] Lu, G. F.; Wang, H. L.; Zheng, Y. L.; Zhang, H.; Yang, Y. P.; Shi, J.; Huang, M. H.; Liu, W. Metal-organic framework derived N-doped CNT@porous carbon for high-performance sodium- and potassium-ion storage. *Electrochim. Acta* **2019**, *319*, 541–551.
[101] Li, D. J.; Cheng, X. L.; Xu, R.; Wu, Y.; Zhou, X. F.; Ma, C.; Yu, Y. Manipulation of 2D carbon nanoplates with a core–shell structure for high-performance potassium-ion batteries. *J. Mater. Chem. A* **2019**, *7*, 19929–19938.
[102] Gabaudan, V.; Berthelot, R.; Stievano, L.; Monconduit, L. Inside the alloy mechanism of Sb and Bi electrodes for K-ion batteries. *J. Phys. Chem. C* **2018**, *122*, 18266–18273.
[103] Liu, Q.; Fan, L.; Ma, R. F.; Chen, S. H.; Yu, X. Z.; Yang, H. G.; Xie, Y.; Han, X.; Lu, B. G. Super long-life potassium-ion batteries based on an antimony@carbon composite anode. *Chem. Commun.* **2018**, *54*, 11773–11776. [104] McCulloch, W. D.; Ren, X. D.; Yu, M. Z.; Huang, Z. J.; Wu, Y. Y. Potassium-ion oxygen battery based on a high capacity antimony anode. *ACS Appl. Mater. Inter.* **2015**, *7*, 26158–26166.
[105] Sultana, I.; Rahman, M. M.; Liu, J. N.; Sharma, N.; Ellis, A. V.; Chen, Y.; Glushenkov, A. M. Antimony-carbon nanocomposites for potassium-ion batteries: Insight into the failure mechanism in electrodes and possible avenues to improve cyclic stability. *J. Power Sources* **2019**, *413*, 476–484.
[106] Zhang, N.; Liu, Y. C.; Lu, Y. Y.; Han, X. P.; Cheng, F. Y.; Chen, J. Spherical nano-Sb@C composite as a high-rate and ultra-stable anode material for sodium-ion batteries. *Nano Res.* **2015**, *8*, 3384–3393.
[107] Gabaudan, V.; Touja, J.; Cot, D.; Flahaut, E.; Stievano, L.; Monconduit, L. Double-walled carbon nanotubes, a performing additive to enhance capacity retention of antimony anode in potassium-ion batteries. *Electrochem. Commun.* **2019**, *105*, 106493.
[108] Zhou, L.; Cao, Z.; Zhang, J.; Cheng, H.; Liu, G.; Park, G. T.; Cavallo, L.; Wang, L. M.; Alshareef, H. N.; Sun, Y. K. et al. Electrolyte-mediated stabilization of high-capacity micro-sized antimony anodes for potassium-ion batteries. *Adv. Mater.* **2021**, *33*, 2005993.
[109] Zhao, N.; Qin, J.; Chu, L. J.; Wang, L. Z.; Xu, D.; Wang, X. J.; Yang, H. J.; Zhang, J. J.; Li, X. F. Heterogeneous interface of Se@Sb@C boosting potassium storage. *Nano Energy* **2020**, *78*, 105345.
[110] Zhao, R. Z.; Di, H. X.; Wang, C. X.; Hui, X. B.; Zhao, D. Y.; Wang, R. T.; Zhang, L. Y.; Yin, L. W. Encapsulating ultrafine Sb nanoparticles in Na^+ pre-intercalated 3D porous $Ti_3C_2T_x$ MXene nanostructures for enhanced potassium storage performance. *ACS Nano* **2020**, *14*, 13938–13951.
[111] Cheng, N.; Zhao, J. G.; Fan, L.; Liu, Z. M.; Chen, S. H.; Ding, H. B.; Yu, X. Z.; Liu, Z. G.; Lu, B. G. Sb-MOFs derived Sb nanoparticles@porous carbon for high performance potassium-ion batteries anode. *Chem. Commun.* **2019**, *55*, 12511–12514.
[112] He, X. D.; Liu, Z. H.; Liao, J. Y.; Ding, X.; Hu, Q.; Xiao, L. N.; Wang, S.; Chen, C. H. A three-dimensional macroporous antimony@carbon composite as a high-performance anode material for potassium-ion batteries. *J. Mater. Chem. A* **2019**, *7*, 9629–9637.
[113] Zheng, J.; Yang, Y.; Fan, X. L.; Ji, G. B.; Ji, X.; Wang, H. Y.; Hou, S.; Zachariah, M. R.; Wang, C. S. Extremely stable antimony–carbon composite anodes for potassium-ion batteries. *Energy Environ. Sci.* **2019**, *12*, 615–623.
[114] Zhang, W. M.; Miao, W. F.; Liu, X. Y.; Li, L.; Yu, Z.; Zhang, Q. H. High-rate and ultralong-stable potassium-ion batteries based on antimony-nanoparticles encapsulated in nitrogen and phosphorus co-doped mesoporous carbon nanofibers as an anode material. *J. Alloys Compd.* **2018**, *769*, 141–148.
[115] Wang, H.; Wu, X.; Qi, X. J.; Zhao, W.; Ju, Z. C. Sb nanoparticles encapsulated in 3D porous carbon as anode material for lithium-ion and potassium-ion batteries. *Mater. Res. Bull.* **2018**, *103*, 32–37.
[116] Luo, W.; Li, F.; Zhang, W. R.; Han, K.; Gaumet, J. J.; Schaefer, H. E.; Mai, L. Q. Encapsulating segment-like antimony nanorod in hollow carbon tube as long-lifespan, high-rate anodes for rechargeable K-ion batteries. *Nano Res.* **2019**, *12*, 1025–1031.
[117] Yi, Z.; Lin, N.; Zhang, W. Q.; Wang, W. W.; Zhu, Y. C.; Qian, Y. T. Preparation of Sb nanoparticles in molten salt and their potassium storage performance and mechanism. *Nanoscale* **2018**, *10*, 13236–13241.
[118] An, Y. L.; Tian, Y.; Ci, L. J.; Xiong, S. L.; Feng, J. K.; Qian, Y. T. Micron-sized nanoporous antimony with tunable porosity for high-performance potassium-ion batteries. *ACS Nano* **2018**, *12*, 12932–12940.
[119] Obrovac, M. N.; Chevrier, V. L. Alloy negative electrodes for Li-ion batteries. *Chem. Rev.* **2014**, *114*, 11444–11502.
[120] Shan, Y. Y.; Li, Y.; Pang, H. Applications of tin sulfide-based materials in lithium-ion batteries and sodium-ion batteries. *Adv. Funct. Mater.* **2020**, *30*, 2001298.
[121] Li, Z.; Ding, J.; Mitlin, D. Tin and tin compounds for sodium ion battery anodes: Phase transformations and performance. *Acc. Chem. Res.* **2015**, *48*, 1657–1665.
[122] Wang, Q. N.; Zhao, X. X.; Ni, C. L.; Tian, H.; Li, J. X.; Zhang, Z.; Mao, S. X.; Wang, J. W.; Xu, Y. H. Reaction and capacity-fading mechanisms of tin nanoparticles in potassium-ion batteries. *J. Phys. Chem. C* **2017**, 121, 12652–12657.
[123] Lang, J. H.; Li, J. R.; Ou, X. W.; Zhang, F.; Shin, K.; Tang, Y. B. A flexible potassium-ion hybrid capacitor with superior rate performance and long cycling life. *ACS Appl. Mater. Inter.* **2020**, *12*, 2424–2431.
[124] Yang, Y. L.; Li, D.; Zhang, J. Q.; Suo, G. Q.; Yu, Q. Y.; Feng, L.; Hou, X. J.; Ye, X. H.; Zhang, L.; Wang, W. Sn nanoparticles anchored on N doped porous carbon as an anode for potassium ion batteries. *Mater. Lett.* **2019**, *256*, 126613.
[125] Sultana, I.; Ramireddy, T.; Rahman, M. M.; Chen, Y.; Glushenkov, A. M. Tin-based composite anodes for potassium-ion batteries. *Chem. Commun.* **2016**, *52*, 9279–9282.
[126] Wang, H.; Xing, Z.; Hu, Z. K.; Zhang, Y.; Hu, Y.; Sun, Y. W.; Ju, Z. C.; Zhuang, Q. C. Sn-based submicron-particles encapsulated in porous reduced graphene oxide network: Advanced anodes for high-rate and long life potassium-ion batteries. *Appl. Mater. Today* **2019**, *15*, 58–66.

[127] Yin, H.; Li, Q. W.; Cao, M. L.; Zhang, W.; Zhao, H.; Li, C.; Huo, K. F.; Zhu, M. Q. Nanosized-bismuth-embedded 1D carbon nanofibers as high-performance anodes for lithium-ion and sodium-ion batteries. *Nano Res*. **2017**, *10*, 2156–2167.
[128] Yang, H.; Xu, R.; Yao, Y.; Ye, S. F.; Zhou, X. F.; Yu, Y. Multicore–shell Bi@N-doped carbon nanospheres for high power density and long cycle life sodium-and potassium-ion anodes. *Adv. Funct. Mater*. **2019**, *29*, 1809195.
[129] Zhang, Q.; Mao, J. F.; Pang, W. K.; Zheng, T.; Sencadas, V.; Chen, Y. Z.; Liu, Y. J.; Guo, Z. P. Boosting the potassium storage performance of alloy-based anode materials via electrolyte salt chemistry. *Adv. Energy Mater*. **2018**, *8*, 1703288.
[130] Cheng, X. L.; Li, D. J.; Wu, Y.; Xu, R.; Yu, Y. Bismuth nanospheres embedded in three-dimensional (3D) porous graphene frameworks as high performance anodes for sodium- and potassium-ion batteries. *J. Mater. Chem. A* **2019**, *7*, 4913–4921.
[131] Lei, K. X.; Wang, C. C.; Liu, L. J.; Luo, Y. W.; Mu, C. N.; Li, F. J.; Chen, J. A porous network of bismuth used as the anode material for high-energy-density potassium-ion batteries. *Angew. Chem., Int. Ed*. **2018**, *57*, 4687–4691.
[132] Yang, W. W.; Lu, Y. X.; Zhao, C. X.; Liu, H. L. First-principles study of black phosphorus as anode material for rechargeable potassium-ion batteries. *Electron. Mater. Lett*. **2020**, *16*, 89–98.
[133] Qin, G. H.; Liu, Y. H.; Liu, F. S.; Sun, X.; Hou, L. R.; Liu, B. B.; Yuan, C. Z. Magnetic field assisted construction of hollow red P nanospheres confined in hierarchical N-doped carbon nanosheets/nanotubes 3D framework for efficient potassium storage. *Adv. Energy Mater*. **2021**, *11*, 2003429.
[134] Chang, W. C.; Wu, J. H.; Chen, K. T.; Tuan, H. Y. Red phosphorus potassium-ion battery anodes. *Adv. Sci*. **2019**, *6*, 1801354.
[135] Sultana, I.; Rahman, M. M.; Ramireddy, T.; Chen, Y.; Glushenkov, A. M. High capacity potassium-ion battery anodes based on black phosphorus. *J. Mater. Chem. A* **2017**, *5*, 23506–23512.
[136] Gao, Y. Q.; Ru, Q.; Liu, Y.; Cheng, S. K.; Wei, L.; Ling, F. C. C.; Chen, F. M.; Hou, X. H. Mosaic red phosphorus/MoS_2 hybrid as an anode to boost potassium-ion storage. *ChemElectroChem* **2019**, *6*, 4689–4695.
[137] Wu, X.; Zhao, W.; Wang, H.; Qi, X. J.; Xing, Z.; Zhuang, Q. C.; Ju, Z. C. Enhanced capacity of chemically bonded phosphorus/carbon composite as an anode material for potassium-ion batteries. *J. Power Sources* **2018**, *378*, 460–467.
[138] Wu, Y.; Hu, S. H.; Xu, R.; Wang, J. W.; Peng, Z. Q.; Zhang, Q. B.; Yu, Y. Boosting potassium-ion battery performance by encapsulating red phosphorus in free-standing nitrogen-doped porous hollow carbon nanofibers. *Nano Lett*. **2019**, *19*, 1351–1358.
[139] Liu, D.; Huang, X. K.; Qu, D. Y.; Zheng, D.; Wang, G. W.; Harris, J.; Si, J. Y.; Ding, T. Y.; Chen, J. H.; Qu, D. Y. Confined phosphorus in carbon nanotube-backboned mesoporous carbon as superior anode material for sodium/potassium-ion batteries. *Nano Energy* **2018**, *52*, 1–10.
[140] Xiong, P. X.; Bai, P. X.; Tu, S. B.; Cheng, M. R.; Zhang, J. F.; Sun, J.; Xu, Y. H. Red phosphorus nanoparticle@3D interconnected carbon nanosheet framework composite for potassium-ion battery anodes. *Small* **2018**, *14*, 1802140.
[141] Huang, X. K.; Liu, D.; Guo, X. R.; Sui, X. Y.; Qu, D. Y.; Chen, J. H. Phosphorus/carbon composite anode for potassium-ion batteries: Insights into high initial coulombic efficiency and superior cyclic performance. *ACS Sustain. Chem. Eng*. **2018**, *6*, 16308–16314.
[142] Wang, H.; Wang, L. F.; Wang, L. C.; Xing, Z.; Wu, X.; Zhao, W.; Qi, X. J.; Ju, Z. C.; Zhuang, Q. C. Phosphorus particles embedded in reduced graphene oxide matrix to enhance capacity and rate capability for capacitive potassium-ion storage. *Chem.–Eur. J*. **2018**, *24*, 13897–13902.
[143] Yang, Q.; Wang, Z. F.; Xi, W.; He, G. Tailoring nanoporous structures of Ge anodes for stable potassium-ion batteries. *Electrochem. Commun*. **2019**, *101*, 68–72.
[144] Tai, Z. X.; Liu, Y. J.; Zhang, Q.; Zhou, T. F.; Guo, Z. P.; Liu, H. K.; Dou, S. X. Ultra-light and flexible pencil-trace anode for high performance potassium-ion and lithium-ion batteries. *Green. Energy Environ*. **2017**, *2*, 278–284.
[145] Gabaudan, V.; Berthelot, R.; Stievano, L.; Monconduit, L. Electrochemical alloying of lead in potassium-ion batteries. *ACS Omega* **2018**, *3*, 12195–12200.
[146] Yan, C. L.; Gu, X.; Zhang, L.; Wang, Y.; Yan, L. T.; Liu, D. D.; Li, L. J.; Dai, P. C.; Zhao, X. B. Highly dispersed Zn nanoparticles confined in a nanoporous carbon network: Promising anode materials for sodium and potassium ion batteries. *J. Mater. Chem. A* **2018**, *6*, 17371–17377.
[147] Wang, Z. Y.; Dong, K. Z.; Wang, D.; Luo, S. H.; Liu, Y. G.; Wang, Q.; Zhang, Y. H.; Hao, A. M.; Shi, C. S.; Zhao, N. Q. A nanosized SnSb alloy confined in N-doped 3D porous carbon coupled with ether-based electrolytes toward high-performance potassium-ion batteries. *J. Mater. Chem. A* **2019**, *7*, 14309–14318.
[148] Zhang, Y. F.; Li, M.; Huang, F. B.; Li, Y. S.; Xu, Y. Q.; Wang, F.; Yao, Q. R.; Zhou, H. Y.; Deng, J. Q. 3D porous Sb-Co nanocomposites as advanced anodes for sodium-ion batteries and potassium-ion batteries. *Appl. Surf. Sci*. **2020**, *499*, 143907.
[149] Wang, J.; Fan, L.; Liu, Z. M.; Chen, S. H.; Zhang, Q. F.; Wang, L. L.; Yang, H. G.; Yu, X. Z.; Lu, B. G. *In situ* alloying strategy for exceptional potassium ion batteries. *ACS Nano* **2019**, *13*, 3703–3713.
[150] Li, J. S.; Xu, X. J.; Yu, X. T.; Han, X.; Zhang, T.; Zuo, Y.; Zhang, C. Q.; Yang, D. W.; Wang, X.; Luo, Z. S. et al. Monodisperse CoSn and NiSn nanoparticles supported on commercial carbon as anode for lithium- and potassium-ion batteries. *ACS Appl. Mater. Inter.* **2020**, *12*, 4414–4422.
[151] He, X. D.; Liao, J. Y.; Wang, S.; Wang, J. R.; Liu, Z. H.; Ding, X.; Hu, Q.; Wen, Z. Y.; Chen, C. H. From nanomelting to nanobeads: Nanostructured Sb_xBi_{1-x} alloys anchored in three-dimensional carbon frameworks as a high-performance anode for potassium-ion batteries. *J. Mater. Chem. A* **2019**, *7*, 27041–27047.
[152] Jiang, J.; Li, Y. Y.; Liu, J. P.; Huang, X. T.; Yuan, C. Z.; Lou, X. W. Recent advances in metal oxide-based electrode architecture design for electrochemical energy storage. *Adv. Mater*. **2012**, *24*, 5166–5180.
[153] Yuan, C. Z.; Wu, H. B.; Xie, Y.; Lou, X. W. Mixed transition-metal oxides: Design, synthesis, and energy-related applications. *Angew. Chem., Int. Ed*. **2014**, *53*, 1488–1504.
[154] Wu, Z. S.; Zhou, G. M.; Yin, L. C.; Ren, W. C.; Li, F.; Cheng, H. M. Graphene/metal oxide composite electrode materials for energy storage. *Nano Energy* **2012**, *1*, 107–131.
[155] Zhao, S. Q.; Dong, L. B.; Sun, B.; Yan, K.; Zhang, J. Q.; Wan, S. W.; He, F. R.; Munroe, P.; Notten, P. H. L.; Wang, G. X. $K_2Ti_2O_5$@C microspheres with enhanced K^+ intercalation pseudocapacitance ensuring fast potassium storage and long-term cycling stability. *Small* **2020**, *16*, 1906131.
[156] Niu, X. G.; Zhang, Y. C.; Tan, L. L.; Yang, Z.; Yang, J.; Liu, T.; Zeng, L.; Zhu, Y. J.; Guo, L. Amorphous $FeVO_4$ as a promising anode material for potassium-ion batteries. *Energy Storage Mater*. **2019**, *22*, 160–167.
[157] Li, N.; Zhang, F.; Tang, Y. B. Hierarchical T-Nb_2O_5 nanostructure with hybrid mechanisms of intercalation and pseudocapacitance for potassium storage and high-performance potassium dual-ion batteries. *J. Mater. Chem. A* **2018**, *6*, 17889–17895.
[158] Li, Z. T.; Dong, Y. F.; Feng, J. Z.; Xu, T.; Ren, H.; Gao, C.; Li, Y. R.; Cheng, M. J.; Wu, W. T.; Wu, M. B. Controllably enriched oxygen vacancies through polymer assistance in titanium pyrophosphate as a super anode for Na/K-ion batteries. *ACS Nano* **2019**, *13*, 9227–9236.
[159] Lee, G. W.; Park, B. H.; Nazarian-Samani, M.; Kim, Y. H.; Roh, K. C.; Kim, K. B. Magneli phase titanium oxide as a novel anode material for potassium-ion batteries. *ACS Omega* **2019**, *4*, 5304–5309.
[160] Xing, L. D.; Yu, Q. Y.; Bao, Y. P.; Chu, J. H.; Han, K.; Chong, S. K.; Lao, C. Y.; Lai, F. L.; Li, P.; Xi, K. et al. Strong (001) facet-induced growth of multi-hierarchical tremella-like Sn-doped V_2O_5 for high-performance potassium-ion batteries. *J. Mater. Chem. A* **2019**, *7*, 25993–26001.
[161] Li, Y. Q.; Shi, H.; Wang, S. B.; Zhou, Y. T.; Wen, Z.; Lang, X. Y.; Jiang, Q. Dual-phase nanostructuring of layered metal oxides for high-performance aqueous rechargeable potassium ion microbatteries. *Nat. Commun*. **2019**, *10*, 4292.
[162] Shimizu, M.; Yatsuzuka, R.; Koya, T.; Yamakami, T.; Arai, S. Tin oxides as a negative electrode material for potassium-ion batteries. *ACS Appl. Energy Mater*. **2018**, *1*, 6865–6870.

[163] Suo, G. Q.; Li, D.; Feng, L.; Hou, X. J.; Yang, Y. L.; Wang, W. SnO_2 nanosheets grown on stainless steel mesh as a binder free anode for potassium ion batteries. *J. Electroanal. Chem.* **2019**, *833*, 113–118.
[164] Cao, K. Z.; Liu, H. Q.; Li, W. Y.; Han, Q. Q.; Zhang, Z.; Huang, K. J.; Jing, Q. S.; Jiao, L. F. CuO nanoplates for high-performance potassium-ion batteries. *Small* **2019**, *15*, 1901775.
[165] Jin, T.; Li, H. X.; Li, Y.; Jiao, L. F.; Chen, J. Intercalation pseudocapacitance in flexible and self-standing V_2O_3 porous nanofibers for high-rate and ultra-stable K ion storage. *Nano Energy* **2018**, *50*, 462–467.
[166] Liu, C. L.; Luo, S. H.; Huang, H. B.; Zhai, Y. C.; Wang, Z. W. Direct growth of MoO_2/reduced graphene oxide hollow sphere composites as advanced anode materials for potassium-ion batteries. *ChemSusChem* **2019**, *12*, 873–880.
[167] Li, P. H.; Wang, W.; Gong, S.; Lv, F.; Huang, H. X.; Luo, M. C.; Yang, Y.; Yang, C.; Zhou, J. H.; Qian, C. et al. Hydrogenated $Na_2Ti_3O_7$ epitaxially grown on flexible N-doped carbon sponge for potassium-ion batteries. *ACS Appl. Mater. Inter.* **2018**, *10*, 37974–37980.
[168] Li, Y. P.; Yang, C. H.; Zheng, F. H.; Pan, Q. C.; Liu, Y. Z.; Wang, G.; Liu, T. Z.; Hu, J. H.; Liu, M. L. Design of TiO_2eC hierarchical tubular heterostructures for high performance potassium ion batteries. *Nano Energy* **2019**, *59*, 582–590.
[169] Liu, Y.; He, D. L.; Tan, Q. W.; Wan, Q.; Han, K.; Liu, Z. W.; Li, P.; An, F. Q.; Qu, X. H. A synergetic strategy for an advanced electrode with Fe_3O_4 embedded in a 3D N-doped porous graphene framework and a strong adhesive binder for lithium/potassium ion batteries with an ultralong cycle lifespan. *J. Mater. Chem. A* **2019**, *7*, 19430–19441.
[170] Wang, Z. Y.; Dong, K. Z.; Wang, D.; Luo, S. H.; Liu, Y. G.; Wang, Q.; Zhang, Y. H.; Hao, A. M.; Shi, C. S.; Zhao, N. Q. Ultrafine SnO_2 nanoparticles encapsulated in 3D porous carbon as a high-performance anode material for potassium-ion batteries. *J. Power Sources* **2019**, *441*, 227191.
[171] Huang, Z.; Chen, Z.; Ding, S. S.; Chen, C. M.; Zhang, M. Enhanced conductivity and properties of SnO_2-graphene-carbon nanofibers for potassium-ion batteries by graphene modification. *Mater. Lett.* **2018**, *219*, 19–22.
[172] Chong, S. K.; Wu, Y. F.; Liu, C. F.; Chen, Y. Z.; Guo, S. W.; Liu, Y. N.; Cao, G. Z. Cryptomelane-type MnO_2/carbon nanotube hybrids as bifunctional electrode material for high capacity potassium-ion full batteries. *Nano Energy* **2018**, 54, 106–115.
[173] Tong, Z. Q.; Yang, R.; Wu, S. L.; Shen, D.; Jiao, T. P.; Zhang, K. L.; Zhang, W. J.; Lee, C. S. Defect-engineered vanadium trioxide nanofiber bundle@graphene hybrids for high-performance all-vanadate Na-ion and K-ion full batteries. *J. Mater. Chem. A* **2019**, *7*, 19581–19588.
[174] Xiao, Y.; Lee, S. H.; Sun, Y. K. The application of metal sulfides in sodium ion batteries. *Adv. Energy Mater.* **2017**, *7*, 1601329.
[175] Liu, Y. Z.; Yang, C. H.; Zhang, Q. Y.; Liu, M. L. Recent progress in the design of metal sulfides as anode materials for sodium ion batteries. *Energy Storage Mater.* **2019**, *22*, 66–95.
[176] Li, W. D.; Wang, D. Z.; Gong, Z. J.; Yin, Z. M.; Guo, X. S.; Liu, J.; Mao, C. M.; Zhang, Z. H.; Li, G. C. A robust strategy for engineering Fe_7S_8/C hybrid nanocages reinforced by defect-rich MoS_2 nanosheets for superior potassium-ion storage. *ACS Nano* **2020**, *14*, 16046–16056.
[177] Li, D. P.; Dai, L. N.; Ren, X. H.; Ji, F. J.; Sun, Q.; Zhang, Y. M.; Ci, L. J. Foldable potassium-ion batteries enabled by free-standing and flexible SnS_2@C nanofibers. *Energy Environ. Sci.* **2021**, *14*, 424–436.
[178] Li, X.; Zhu, H. W. Two-dimensional MoS_2: Properties, preparation, and applications. *J. Materiom.* **2015**, *1*, 33–44.
[179] Dong, Y. L.; Xu, Y.; Li, W.; Fu, Q.; Wu, M. H.; Manske, E.; Kröger, J.; Lei, Y. Insights into the crystallinity of layer-structured transition metal dichalcogenides on potassium ion battery performance: A case study of molybdenum disulfide. *Small* **2019**, *15*, 1900497.
[180] He, H. N.; Huang, D.; Gan, Q. M.; Hao, J. N.; Liu, S. L.; Wu, Z. B.; Pang, W. K.; Johannessen, B.; Tang, Y. G.; Luo, J. L. et al. Anion vacancies regulating endows MoSSe with fast and stable potassium ion storage. *ACS Nano* **2019**, *13*, 11843–11852.
[181] Zhang, J. Y.; Cui, P. X.; Gu, Y.; Wu, D. J.; Tao, S.; Qian, B.; Chu, W. S.; Song, L. Encapsulating carbon-coated MoS_2 nanosheets within a nitrogen-doped graphene network for high-performance potassium-ion storage. *Adv. Mater. Interfaces* **2019**, *6*, 1901066.
[182] Rui, B. L.; Li, J. H.; Chang, L. M.; Wang, H. R.; Lin, L.; Guo, Y.; Nie, P. Engineering MoS_2 nanosheets anchored on metal organic frameworks derived carbon polyhedra for superior lithium and potassium storage. *Front. Energy Res.* **2019**, *7*, 142.
[183] Jia, B. R.; Zhao, Y. Z.; Qin, M. L.; Wang, W.; Liu, Z. W.; Lao, C. Y.; Yu, Q. Y.; Liu, Y.; Wu, H. W.; Zhang, Z. L. et al. Multirole organic-induced scalable synthesis of a mesoporous MoS_2-monolayer/carbon composite for high-performance lithium and potassium storage. *J. Mater. Chem. A* **2018**, *6*, 11147–11153.
[184] Di, S. J.; Ding, P.; Wang, Y. Y.; Wu, Y. L.; Deng, J.; Jia, L.; Li, Y. G. Interlayer-expanded MoS_2 assemblies for enhanced electrochemical storage of potassium ions. *Nano Res.* **2020**, *13*, 225–230.
[185] Chong, S. K.; Sun, L.; Shu, C. Y.; Guo, S. W.; Liu, Y. N.; Wang, W.; Liu, H. K. Chemical bonding boosts nano-rose-like MoS_2 anchored on reduced graphene oxide for superior potassium-ion storage. *Nano Energy* **2019**, *63*, 103868.
[186] Xie, K. Y.; Yuan, K.; Li, X.; Lu, W.; Shen, C.; Liang, C. L.; Vajtai, R.; Ajayan, P.; Wei, B. Q. Superior potassium ion storage via vertical MoS_2 "nano-rose" with expanded interlayers on graphene. *Small* **2017**, *13*, 1701471.
[187] Jia, B. R.; Yu, Q. Y.; Zhao, Y. Z.; Qin, M. L.; Wang, W.; Liu, Z. W.; Lao, C. Y.; Liu, Y.; Wu, H. W.; Zhang, Z. L. et al. Bamboo-like hollow tubes with MoS_2/N-doped-C interfaces boost potassium-ion storage. *Adv. Funct. Mater.* **2018**, *28*, 1803409.
[188] Zhang, N.; Jiang, G. Y.; Chen, X.; Mao, J. Y.; Zhou, Y. J.; Li, Y. S. Rational design of a tubular, interlayer expanded MoS_2–N/O doped carbon composite for excellent potassium-ion storage. *J. Mater. Chem. A* **2019**, *7*, 9305–9315.
[189] Xing, L. D.; Yu, Q. Y.; Jiang, B.; Chu, J. H.; Lao, C. Y.; Wang, M.; Han, K.; Liu, Z. W.; Bao, Y. P.; Wang, W. Carbon-encapsulated ultrathin MoS_2 nanosheets epitaxially grown on porous metallic $TiNb_2O_6$ microspheres with unsaturated oxygen atoms for superior potassium storage. *J. Mater. Chem. A* **2019**, *7*, 5760–5768.
[190] Liu, Y. T.; Xiao, Y. Y.; Liu, F. S.; Han, P. Y.; Qin, G. H. Controlled building of mesoporous MoS_2@MoO_2-doped magnetic carbon sheets for superior potassium ion storage. *J. Mater. Chem. A* **2019**, *7*, 26818–26828.
[191] Chen, Z.; Yin, D. G.; Zhang, M. Sandwich-like MoS_2@SnO_2@C with high capacity and stability for sodium/potassium ion batteries. *Small* **2018**, *14*, 1703818.
[192] Zhang, C. Z.; Han, F.; Wang, F.; Liu, Q. D.; Zhou, D. W.; Zhang, F. Q.; Xu, S. H.; Fan, C. L.; Li, X. K.; Liu, J. S. Improving compactness and reaction kinetics of MoS_2@C anodes by introducing Fe_9S_{10} core for superior volumetric sodium/potassium storage. *Energy Storage Mater.* **2020**, *24*, 208–219.
[193] Lakshmi, V.; Chen, Y.; Mikhaylov, A. A.; Medvedev, A. G.; Sultana, I.; Rahman, M. M.; Lev, O.; Prikhodchenko, P. V.; Glushenkov, A. M. Nanocrystalline SnS_2 coated onto reduced graphene oxide: Demonstrating the feasibility of a non-graphitic anode with sulfide chemistry for potassium-ion batteries. *Chem. Commun.* **2017**, *53*, 8272–8275.
[194] Rehman, J.; Fan, X. F.; Zheng, W. T. Computational insight of monolayer SnS_2 as anode material for potassium ion batteries. *Appl. Surf. Sci.* **2019**, *496*, 143625.
[195] Fan, L. Z.; Xu, J.; Sun, S.; Lin, B. W.; Guo, Q. B.; Luo, D.; Xia, H. Few-layered tin sulfide nanosheets supported on reduced graphene oxide as a high-performance anode for potassium-ion batteries. *Small* **2019**, *15*, 1804806.
[196] Li, D. P.; Sun, Q.; Zhang, Y. M.; Chen, L. N.; Wang, Z. P.; Liang, Z.; Si, P. C.; Ci, L. J. Surface-confined SnS_2@C@rGO as high-performance anode materials for sodium- and potassium-ion batteries. *ChemSusChem* **2019**, *12*, 2689–2700.
[197] Miao, W. F.; Zhang, Y.; Li, H. T.; Zhang, Z. H.; Li, L.; Yu, Z.; Zhang, W. M. ZIF-8/ZIF-67-derived 3D amorphous carbon-encapsulated CoS/NCNTs supported on CoS-coated carbon nanofibers as an advanced potassium-ion battery anode. *J. Mater. Chem. A* **2019**, *7*, 5504–5512.
[198] Gao, H.; Zhou, T. F.; Zheng, Y.; Zhang, Q.; Liu, Y. Q.; Chen, J.;

Liu, H. K.; Guo, Z. P. CoS Quantum dot nanoclusters for high-energy potassium-ion batteries. *Adv. Funct. Mater.* **2017**, *27*, 1702634.
[199] Yu, Q. Y.; He, J.; Qian, C.; Gao, Y. Z.; Wang, W.; Yin, G. P. CoS/N-doped carbon core/shell nanocrystals as an anode material for potassium-ion storage. *J. Solid State Electrochem.* **2019**, *23*, 27–32.
[200] Zhao, Y.; Zhu, J. J.; Ong, S. J. H.; Yao, Q. Q.; Shi, X. L.; Hou, K.; Xu, Z. J.; Guan, L. H. High-rate and ultralong cycle-life potassium ion batteries enabled by *in situ* engineering of yolk–shell FeS_2@C structure on graphene matrix. *Adv. Energy Mater.* **2018**, *8*, 1802565.
[201] Xie, J. P.; Zhu, Y. Q.; Zhuang, N.; Lei, H.; Zhu, W. L.; Fu, Y.; Javed, M. S.; Li, J. L.; Mai, W. J. Rational design of metal organic framework-derived FeS_2 hollow nanocages@reduced graphene oxide for K-ion storage. *Nanoscale* **2018**, *10*, 17092–17098.
[202] Yao, Q. Q.; Zhang, J. S.; Shi, X. L.; Deng, B. L.; Hou, K.; Zhao, Y.; Guan, L. H. Rational synthesis of two-dimensional G@porous FeS_2@C composite as high-rate anode materials for sodium/potassium ion batteries. *Electrochim. Acta* **2019**, *307*, 118–128.
[203] Luo, Y. S.; Tao, M. L.; Deng, J. H.; Zhan, R. M.; Guo, B. S.; Ma, Q. R.; Aslam, M. K.; Qi, Y. R.; Xu, M. W. Nanocubes composed of FeS_2@C nanoparticles as advanced anode materials for K-ion storage. *Inorg. Chem. Front.* **2020**, *7*, 394–401.
[204] Zhang, R. D.; Bao, J. Z.; Pan, Y. L.; Sun, C. F. Highly reversible potassium-ion intercalation in tungsten disulfide. *Chem. Sci.* **2019**, *10*, 2604–2612.
[205] Wu, Y. H.; Xu, Y.; Li, Y. L.; Lyu, P. B.; Wen, J.; Zhang, C. L.; Zhou, M.; Fang, Y. G.; Zhao, H. P.; Kaiser, U. et al. Unexpected intercalation-dominated potassium storage in WS_2 as a potassium-ion battery anode. *Nano Res.* **2019**, *12*, 2997–3002.
[206] Liu, Y. J.; Tai, Z. X.; Zhang, J.; Pang, W. K.; Zhang, Q.; Feng, H. F.; Konstantinov, K.; Guo, Z. P.; Liu, H. K. Boosting potassium-ion batteries by few-layered composite anodes prepared via solution-triggered one-step shear exfoliation. *Nat. Commun.* **2018**, *9*, 3645.
[207] Li, T.; Zhang, Q. Advanced metal sulfide anode for potassium ion batteries. *J. Energy Chem.* **2018**, *27*, 373–374.
[208] Jia, X. X.; Zhang, E. J.; Yu, X. Z.; Lu, B. G. Facile synthesis of copper sulfide nanosheet@graphene oxide for the anode of potassium-ion batteries. *Energy Technol.* **2020**, *8*, 1900987.
[209] Xie, J. P.; Li, X. D.; Lai, H. J.; Zhao, Z. J.; Li, J. L.; Zhang, W. G.; Xie, W. G.; Liu, Y. M.; Mai, W. J. A Robust solid electrolyte interphase layer augments the ion storage capacity of bimetallic-sulfide-containing potassium-ion batteries. *Angew. Chem., Int. Ed.* **2019**, *58*, 14740–14747.
[210] Wang, W.; Jiang, B.; Qian, C.; Lv, F.; Feng, J. R.; Zhou, J. H.; Wang, K.; Yang, C.; Yang, Y.; Guo, S. J. Pistachio-shuck-like $MoSe_2$/C core/shell nanostructures for high-performance potassium-ion storage. *Adv. Mater.* **2018**, *30*, 1801812.
[211] Chu, J. H.; Yu, Q. Y.; Yang, D. X.; Xing, L. D.; Lao, C. Y.; Wang, M.; Han, K.; Liu, Z. W.; Zhang, L.; Du, W. Y. et al. Thickness-control of ultrathin bimetallic Fe–Mo selenide@N-doped carbon core/shell "nano-crisps" for high-performance potassium-ion batteries. *Appl. Mater. Today* **2018**, *13*, 344–351.
[212] Zeng, L. X.; Kang, B. Y.; Luo, F. Q.; Fang, Y. X.; Zheng, C.; Liu, J. B.; Liu, R. P.; Li, X. Y.; Chen, Q. H.; Wei, M. D. et al. Facile synthesis of ultra-small few-layer nanostructured $MoSe_2$ embedded on N, P co-doped bio-carbon for high-performance half/full sodium-ion and potassium-ion batteries. *Chem.–Eur. J.* **2019**, *25*, 13411–13421.
[213] Shen, Q.; Jiang, P. J.; He, H. C.; Chen, C. M.; Liu, Y.; Zhang, M. Encapsulation of $MoSe_2$ in carbon fibers as anodes for potassium ion batteries and nonaqueous battery–supercapacitor hybrid devices. *Nanoscale* **2019**, *11*, 13511–13520.
[214] Huang, H. W.; Cui, J.; Liu, G. X.; Bi, R.; Zhang, L. Carbon-coated $MoSe_2$/MXene hybrid nanosheets for superior potassium storage. *ACS Nano* **2019**, *13*, 3448–3456.
[215] Sannyal, A.; Zhang, Z. Q.; Gao, X. F.; Jang, J. Two-dimensional sheet of germanium selenide as an anode material for sodium and potassium ion batteries: First-principles simulation study. *Comput. Mater. Sci.* **2018**, *154*, 204–211.
[216] He, C.; Zhang, J. H.; Zhang, W. X.; Li, T. T. GeSe/BP van der Waals heterostructures as promising anode materials for potassium-ion batteries. *J. Phys. Chem. C* **2019**, *123*, 5157–5163.
[217] Zhou, Y.; Zhao, M.; Chen, Z. W.; Shi, X. M.; Jiang, Q. Potential application of 2D monolayer β-GeSe as an anode material in Na/K ion batteries. *Phys. Chem. Chem. Phys.* **2018**, *20*, 30290–30296.
[218] Yu, H. X.; Cheng, X.; Xia, M. T.; Liu, T. T.; Ye, W. Q.; Zheng, R. T.; Long, N. B.; Shui, M.; Shu, J. Pretreated commercial $TiSe_2$ as an insertion-type potassium container for constructing "Rocking-Chair" type potassium ion batteries. *Energy Storage Mater.* **2019**, *22*, 154–159.
[219] Wu, M. G.; Yang, J. L.; Ng, D. H. L.; Ma, J. M. Rhenium diselenide anchored on reduced graphene oxide as anode with cyclic stability for potassium-ion battery. *Phys. Status Solidi Rapid Res. Lett.* **2019**, *13*, 1900329.
[220] Yu, Q. Y.; Jiang, B.; Hu, J.; Lao, C. Y.; Gao, Y. Z.; Li, P. H.; Liu, Z. W.; Suo, G. Q.; He, D. L.; Wang, W. et al. Metallic octahedral $CoSe_2$ threaded by N-doped carbon nanotubes: A flexible framework for high-performance potassium-ion batteries. *Adv. Sci.* **2018**, *5*, 1800782.
[221] Etogo, C. A.; Huang, H. W.; Hong, H.; Liu, G. X.; Zhang, L. Metal-organic-frameworks-engaged formation of $Co_{0.85}Se$@C nanoboxes embedded in carbon nanofibers film for enhanced potassium-ion storage. *Energy Storage Mater.* **2020**, *24*, 167–176.
[222] Liu, Z. W.; Han, K.; Li, P.; Wang, W.; He, D. L.; Tan, Q. W.; Wang, L. Y.; Li, Y.; Qin, M. L.; Qu, X. H. Tuning metallic $Co_{0.85}Se$ quantum dots/carbon hollow polyhedrons with tertiary hierarchical structure for high-performance potassium ion batteries. *Nano-Micro Lett.* **2019**, *11*, 96.
[223] Chu, J. H.; Wang, W.; Yu, Q. Y.; Lao, C. Y.; Zhang, L.; Xi, K.; Han, K.; Xing, L. D.; Song, L.; Wang, M. et al. Open ZnSe/C nanocages: Multi-hierarchy stress-buffer for boosting cycling stability in potassium-ion batteries. *J. Mater. Chem. A* **2020**, *8*, 779–788.
[224] Hu, Y.; Lu, T. T.; Zhang, Y.; Sun, Y. W.; Liu, J. L.; Wei, D. H.; Ju, Z. C.; Zhuang, Q. C. Highly dispersed ZnSe nanoparticles embedded in N-doped porous carbon matrix as an anode for potassium ion batteries. *Part. Part. Syst. Charact.* **2019**, *36*, 1900199.
[225] Yang, C.; Feng, J. R.; Lv, F.; Zhou, J. H.; Lin, C. F.; Wang, K.; Zhang, Y. L.; Yang, Y.; Wang, W.; Li, J. B. et al. Metallic graphene-like VSe_2 ultrathin nanosheets: Superior potassium-ion storage and their working mechanism. *Adv. Mater.* **2018**, *30*, 1800036.
[226] Tian, H. J.; Yu, X. C.; Shao, H. Z.; Dong, L. B.; Chen, Y.; Fang, X. Q.; Wang, C. Y.; Han, W. Q.; Wang, G. X. Unlocking few-layered ternary chalcogenides for high-performance potassium-ion storage. *Adv. Energy Mater.* **2019**, *9*, 1901560.
[227] Luo, Y. S.; Han, J.; Ma, Q. R.; Zhan, R. M.; Zhang, Y. Q.; Xu, Q. J.; Xu, M. W. Exploration of $NbSe_2$ flakes as reversible host materials for sodium-ion and potassium-ion batteries. *Chem. Select* **2018**, *3*, 9807–9811.
[228] Verma, R.; Didwal, P. N.; Ki, H. S.; Cao, G. Z.; Park, C. J. SnP_3/carbon nanocomposite as an anode material for potassium-ion batteries. *ACS Appl. Mater. Inter.* **2019**, *11*, 26976–26984.
[229] Yang, F. H.; Hao, J. N.; Long, J.; Liu, S. L.; Zheng, T.; Lie, W.; Chen, J.; Guo, Z. P. Achieving high-performance metal phosphide anode for potassium ion batteries via concentrated electrolyte chemistry. *Adv. Energy Mater.* **2021**, *11*, 2003346.
[230] Zhang, W. C.; Pang, W. K.; Sencadas, V.; Guo, Z. P. Understanding high-energy-density Sn_4P_3 anodes for potassium-ion batteries. *Joule* **2018**, *2*, 1534–1547.
[231] Li, D. P.; Zhang, Y. M.; Sun, Q.; Zhang, S. N.; Wang, Z. P.; Liang, Z.; Si, P. C.; Ci, L. J. Hierarchically porous carbon supported Sn_4P_3 as a superior anode material for potassium-ion batteries. *Energy Storage Mater.* **2019**, *23*, 367–374.
[232] Zhao, X. X.; Wang, W. H.; Hou, Z.; Wei, G. J.; Yu, Y. K.; Zhang, J.; Quan, Z. W. $SnP_{0.94}$ nanoplates/graphene oxide composite for novel potassium-ion battery anode. *Chem. Eng. J.* **2019**, *370*, 677–683.
[233] Yang, W. W.; Zhang, J. Y.; Huo, D.; Sun, S.; Tao, S.; Wang, Z. C.; Wang, J.; Wu, D. J.; Qian, B. Facile synthesis of tin phosphide/reduced graphene oxide composites as anode material for potassium-ion batteries. *Ionics* **2019**, *25*, 4795–4803.
[234] Yang, F. H.; Gao, H.; Hao, J. N.; Zhang, S. L.; Li, P.; Liu, Y. Q.; Chen, J.; Guo, Z. P. Yolk–shell structured FeP@C nanoboxes as advanced anode materials for rechargeable lithium-/potassium-ion batteries. *Adv. Funct. Mater.* **2019**, *29*, 1808291.
[235] Li, W. T.; Yan, B. J.; Fan, H. W.; Zhang, C.; Xu, H. Y.; Cheng, X. L.; Li, Z. L.; Jia, G. X.; An, S. L.; Qiu, X. P. FeP/C composites as

an anode material for K-ion batteries. *ACS Appl. Mater. Inter.* **2019**, *11*, 22364–22370.

[236] Wang, Y. X.; Zhang, Z. Y.; Wang, G. X.; Yang, X. Y.; Sui, Y. M.; Du, F.; Zou, B. Ultrafine Co_2P nanorods wrapped by graphene enable a long cycle life performance for a hybrid potassium-ion capacitor. *Nanoscale Horiz.* **2019**, *4*, 1394–1401.

[237] Chen, X. X.; Zeng, S. Y.; Muheiyati, H.; Zhai, Y. J.; Li, C. C.; Ding, X. Y.; Wang, L.; Wang, D. B.; Xu, L. Q.; He, Y. Y. et al. Double-shelled Ni–Fe–P/N-doped carbon nanobox derived from a prussian blue analogue as an electrode material for K-ion batteries and Li–S batteries. *ACS Energy Lett.* **2019**, *4*, 1496–1504.

[238] Sun, N.; Zhu, Q. Z.; Anasori, B.; Zhang, P.; Liu, H.; Gogotsi, Y.; Xu, B. MXene-bonded flexible hard carbon film as anode for stable Na/K-ion storage. *Adv. Funct. Mater.* **2019**, *29*, 1906282.

[239] Tian, Y.; An, Y. L.; Xiong, S. L.; Feng, J. K.; Qian, Y. T. A general method for constructing robust, flexible and freestanding MXene@metal anodes for high-performance potassium-ion batteries. *J. Mater. Chem. A* **2019**, *7*, 9716–9725.

[240] Lian, P. C.; Dong, Y. F.; Wu, Z. S.; Zheng, S. H.; Wang, X. H.; Wang, S.; Sun, C. L.; Qin, J. Q.; Shi, X. Y.; Bao, X. H. Alkalized Ti_3C_2 MXene nanoribbons with expanded interlayer spacing for high-capacity sodium and potassium ion batteries. *Nano Energy* **2017**, *40*, 1–8.

[241] Tao, M. L.; Du, G. Y.; Zhang, Y. Q.; Gao, Q.; Liu, D. Y.; Luo, Y. S.; Jiang, J.; Bao, S. J.; Xu, M. W. TiO_xN_y nanoparticles/C composites derived from MXene as anode material for potassium-ion batteries. *Chem. Eng. J.* **2019**, *369*, 828–833.

[242] Li, C.; Hu, X. S.; Hu, B. W. Cobalt(II) dicarboxylate-based metal-organic framework for long-cycling and high-rate potassium-ion battery anode. *Electrochim. Acta* **2017**, *253*, 439–444.

[243] Wu, H. Y.; Yu, Q. Y.; Lao, C. Y.; Qin, M. L.; Wang, W.; Liu, Z. W.; Man, C.; Wang, L. Y.; Jia, B. R.; Qu, X. H. Scalable synthesis of VN quantum dots encapsulated in ultralarge pillared N-doped mesoporous carbon microsheets for superior potassium storage. *Energy Storage Mater.* **2019**, *18*, 43–50.

[244] Katorova, N. S.; Fedotov, S. S.; Rupasov, D. P.; Luchinin, N. D.; Delattre, B.; Chiang, Y. M.; Abakumov, A. M.; Stevenson, K. J. Effect of concentrated diglyme-based electrolytes on the electrochemical performance of potassium-ion batteries. *ACS Appl. Energy Mater.* **2019**, *2*, 6051–6059.